Università degli Studi di Palermo

AREA QUALITÀ, PROGRAMMAZIONE E SUPPORTO STRATEGICO
SETTORE STRATEGIA PER LA RICERCA
U. O. DOTTORATI

Dottorato in Energia e Tecnologie dell'Informazione
Dipartimento di Ingegneria (DI)
Settore Scientifico Disciplinare ING-IND/31 – Elettrotecnica

# PULSED ELECTRO-ACOUSTIC SPACE CHARGE APPARATUS – QUALIFYING, TESTING AND MONITORING OF INSULATION FOR HVDC CABLES AND ACCESSORIES

IL DOTTORE
**Giuseppe Rizzo**

IL COORDINATORE
**Prof. Maurizio Cellura**

IL TUTOR
**Prof. Guido Ala**

CO TUTOR
**Prof. Pietro Romano**

CICLO XXXIV
ANNO CONSEGUIMENTO TITOLO 2022

# Preface

This document refers to the activities carried out in the framework of the PhD with industrial characterization funded from the Italian Ministry of University and Research (MIUR) with scholarship code DOT1320917, CUP B77I18065610001. The activities were aimed to develop a research project called "Pulsed Electro-Acoustic Space Charge Apparatus". This project was focused on the study of the role of space charge accumulation on the reliability and aging of the insulation of HVDC (High Voltage Direct Current) cables and accessories. With this aim, the phenomenon of space charge accumulation was investigated through bibliographic research and through the implementation of models to simulate such phenomena in HVDC cables and accessories in different scenarios. These simulations essentially concerned the study of the effect of axial heat transmission on the achievement of local electric field peaks in HVDC cables and joints as well as the time trend of the electric field during transients such as Polarity Reversal or Transient Over-Voltages.

In addition to this, the state-of-the-art of the Pulsed Electro-Acoustic (PEA) method was studied. This technique is considered one of the most reliable for measuring the distribution of space charge. In addition to the bibliographic research on the PEA method, space charge measurements were carried out on both flat and cable samples using commercial equipments at the LEPRE high voltage laboratory of the University of Palermo.

Following this study, as part of the collaboration with Prysmian Electronics, the industrial partner of this PhD, an innovative PEA apparatus was designed for measuring the distribution of space charge in flat specimens up to 5 mm thick under temperature gradient. In addition to the design of the PEA cell, a pulse generator suitable for the range of specimens to test as well as the heating and cooling systems of the two surfaces of the sample were designed.

In order to evaluate the interaction between space charge and partial discharge phenomena, studies were carried out both by means of models and experimental campaigns. Part of these studies were conducted in cooperation with Chalmers University of Technology using the experience of its staff in the measurement and analysis of partial discharges. The comparison between these experimental and computational results led to optimizing the conductivity models used and improving the predictability of the phenomenon of partial discharges under DC voltage.

# Table of contents

# List of publications

## *International Conference Papers with peer review:*

1. G. Ala, A. G. Giglia, A. Imburgia, R. Miceli, G. Rizzo, P. Romano, F. Viola; S. Quondam Antonio, H. P. Rimal, "Design of Soft Ferrite filters for EMI reduction in Power Conversion Systems," 2019 IEEE 5th International forum on Research and Technology for Society and Industry (RTSI), 2019, pp. 394-399.
2. G. Giglia, G. Ala, V. Castiglia, A. Imburgia, R. Miceli, G. Rizzo, P. Romano, G. Schettino, F. Viola, "Electromagnetic Full-Wave Simulation of Partial Discharge Detection in High Voltage AC Cables," 2019 IEEE 5th International forum on Research and Technology for Society and Industry (RTSI), 2019, pp. 166-171.
3. G. Rizzo, P. Romano, G. Ala and T. J. Å. Hammarström, "Deformation of bubbles in silicon gel insulation under an alternating electric field," 2019 IEEE Conference on Electrical Insulation and Dielectric Phenomena (CEIDP), 2019, pp. 536-539.
4. G. Rizzo, P. Romano, G. Ala, E. R. Sanseverino, R. Candela and V. Li Vigni, "A new approach to calibrate the thermal conditions in space charge measurements on HVDC mini-cables," 2019 IEEE Conference on Electrical Insulation and Dielectric Phenomena (CEIDP), 2019, pp. 438-441.
5. A. Imburgia, P. Romano, G. Ala, G. Rizzo, G. Giglia and F. Viola, "Acoustic Wave Behavior in a Specimen Containing an Air Void Defect," 2019 IEEE Conference on Electrical Insulation and Dielectric Phenomena (CEIDP), 2019, pp. 470-473.
6. A. Imburgia, P. Romano, G. Ala, M. Albertini,L. De Rai, S. Franchi Bononi, E. Riva Sanseverino, G. Rizzo, S. Siripurapu, "Different Measurement Setup Configurations for Space Charge test in Mini Cable Specimens with the PEA Method," 2019 IEEE Conference on Electrical Insulation and Dielectric Phenomena (CEIDP), 2019, pp. 478-481.
7. P. Romano, G. Rizzo, C. Consolazione, R. Candela and G. Ala, "The Partial Discharge Behavior of Different Materials Under DC Periodic Stress," 2019 IEEE Conference on Electrical Insulation and Dielectric Phenomena (CEIDP), 2019, pp. 661-665.

8. P. Romano, A. Imburgia, Y. Serdyuk, G. Ala, J. Blennow, M. Bongiorno, C. Grasso; T. Hammarström, G. Rizzo, "The Effect of the Harmonic Content Generated by AC/DC Modular Multilevel Converters on HVDC Cable Systems," 2019 IEEE Conference on Electrical Insulation and Dielectric Phenomena (CEIDP), 2019, pp. 666-669.
9. G. Rizzo, P. Romano, A. Imburgia, F. Viola, G. Schettino, G. Giglia, G. Ala, "Space charge accumulation in undersea HVDC cables as function of heat exchange conditions at the boundaries – water-air interface," 2020 IEEE 20th Mediterranean Electrotechnical Conference ( MELECON), 2020, pp. 447-452.
10. A. Imburgia, P. Romano, G. Ala, M. Albertini, L. de Rai, S. Franchi Bononi, E. Riva Sanseverino, G. Rizzo, S. Siripurapu, F. Viola, "Effect of Polarity Reversal on the Partial Discharge Phenomena," 2020 IEEE Conference on Electrical Insulation and Dielectric Phenomena (CEIDP), 2020, pp. 378-381.
11. P. Romano, G. Rizzo, A. Imburgia, F. Viola, G. Ala, Roberto Candela, V. Li Vigni, S. Franchi Bononi, M. Albertini, "Investigation on partial discharges in HVDC cables after polarity reversal events," 2020 IEEE Conference on Electrical Insulation and Dielectric Phenomena (CEIDP), 2020, pp. 292-295.
12. G. Rizzo, P. Romano, A. Imburgia, F. Viola, G. Ala, Roberto Candela, V. Li Vigni, S. Franchi Bononi, M. Albertini, "Polarity reversal in HVDC joints - the effect of the axial thermal conduction," *2020 IEEE Conference on Electrical Insulation and Dielectric Phenomena (CEIDP)*, 2020, pp. 115-118.
13. G. Rizzo, P. Romano, A. Imburgia, M. Albertini, S. Franchi Bononi, S. Siripurapu, G. Ala, "The effect of Transient Over Voltages on the Partial Discharges activity in HVDC joints," 2021 AEIT HVDC International Conference (AEIT HVDC), 2021, pp. 1-6.

## *Journal publications:*

1. G. Rizzo, P. Romano, A. Imburgia, and G. Ala, “Review of the PEA Method for Space Charge Measurements on HVDC Cables and Mini-Cables,” Energies, vol. 12, no. 18, p. 3512, Sep. 2019.

2. A. Imburgia, P. Romano, G. Chen, G. Rizzo, E. Riva Sanseverino, F. Viola, and G. Ala, “The Industrial Applicability of PEA Space Charge Measurements, for Performance Optimization of HVDC Power Cables,” Energies, vol. 12, no. 21, p. 4186, Nov. 2019.
3. G. Rizzo, P. Romano, A. Imburgia, F. Viola, and G. Ala, “The Effect of the Axial Heat Transfer on Space Charge Accumulation Phenomena in HVDC Cables,” Energies, vol. 13, no. 18, p. 4827, Sep. 2020.
4. A. Imburgia, P. Romano, G. Rizzo, F. Viola, G. Ala, and G. Chen, “Reliability of PEA Measurement in Presence of an Air Void Defect,” Energies, vol. 13, no. 21, p. 5652, Oct. 2020.
5. P. Romano, A. Imburgia, G. Rizzo, G. Ala and R. Candela, "A New Approach to Partial Discharge Detection Under DC Voltage: Application to Different Materials," in IEEE Electrical Insulation Magazine, vol. 37, no. 2, pp. 18-32, March-April 2021.
6. G. Rizzo, F. Viola, G. Ala, P. Romano, G. Schettino, A. Imburgia, G. Giglia, "Effect of Heat Exchange Transient Conditions With Moving Water-Air Interface on Space Charge Accumulation in Undersea HVdc Cables," in IEEE Transactions on Industry Applications, vol. 57, no. 5, pp. 4528-4536, Sept.-Oct. 2021.
7. G. Rizzo, P. Romano, A. Imburgia, G. Ala, “Partial discharges in HVDC cables – the effect of the temperature gradient during load transients,” in IEEE Transactions on Dielectrics and Electrical Insulation, October 2021.

# Introduction

Nowadays, the interest on DC transmissions is constantly growing in most part of the world [1]. This can essentially be attributed to the need to increase the transnational exchange of electricity or, in any case, to enhance long-distance connections. From a purely economic point of view, for the same power to be transported, an HVDC transmission line has advantages and disadvantages compared to an HVAC line [2].

The main advantages from an economic point of view are the lower use of copper with the same losses due to the Joule effect in the conductor and the absence of phenomena such as eddy currents and the skin effect that cause power losses in HVDC cables. Therefore, the cost per unit of length and with the same losses of an HVDC line section is certainly lower than that of an HVAC. On the other hand, the cost of the conversion stations, necessary for HVDC transmissions, significantly affects the total cost of the link. For this reason, for a given project, it is possible to define a minimum connection length above which an HVDC cable line is cheaper than an HVAC. In addition to this factor, it is useful to consider that HVDC technology is the only one that allows the construction of subsea cable lines even over medium distances.

The first commercial installation of an HVDC cable line dates back to 1954, when the project called “Gotland 1” was realized. For many years, the prevailing technologies for making HVDC cables were mass-impregnated (MI) and oil-filled (OF) [3]. The main limitation of MI cables is the low maximum temperature to which the cable can be subjected and the low mechanical resistance. On the other hand, OF cables have limits on the maximum length that can be reached [2].

Because the widespread use of Cross-linked Polyethylene (XLPE) in High Voltage Alternating Current (HVAC) systems, thanks to the advantages of insulating material (e.g. high dielectric strength, electrical resistivity and good mechanical and thermal properties), the cable industry has begun to use XLPE also for HVDC cables. In this way, the problems related to the use of MI and OF cables were overcome. However, the use of extruded cables for HVDC transmission has shown the onset of premature aging due to space charge accumulation phenomena in the bulk of the dielectric and near the electrodes [4]. Therefore, new insights were necessary to evaluate the reliability of the insulation and to better understand the strategies to be used to produce and manage extruded HVDC cables in the best possible way.

Research on these topics is also needed to address future challenges that see the increasing use of Extra High Voltage Direct Current (EHVDC) and Ultra High Voltage Direct Current (UHVDC) cables [5].

The research work described in this thesis is divided into three main branches:

a) Development and use of coupled thermal and electric macroscopic models in order to study the effect of space charge accumulation on the electric field distribution within the insulation of HVDC cables and accessories in different scenarios.
b) Use of space charge measurement methods with particular reference to the method called Pulsed Electro Acoustic (PEA) and design of an innovative measurement system.
c) Analysis of conduction phenomena in dielectrics through the measurement of Partial Discharges (PD) in cavities within dielectric materials subjected to HVDC stress.

Unlike in conductive materials, in dielectrics, the electrical conductivity increases with temperature. Combined with the current continuity law, this characteristic of dielectrics results in the accumulation of space charge in the insulation layer of a loaded HVDC cable. In particular, as demonstrated by several researchers, this phenomenon would tend to accumulate space charge near the conductor leading to the deformation of the radial distribution of the electric field with respect to the profile that would be obtained with the dielectric at a homogeneous temperature. In addition to this aspect, other phenomena contribute to the introduction, accumulation and displacement of charges within the dielectric layer. The insulation of a cable or an HVDC accessory is typically located between the conductor and the shield and is separated from these by a layer of semiconductive material. Even if the semiconductive compound is made starting from the same mixture of the dielectric used, the variation of the material at the interfaces leads to electron and ion injection due to the Schottky effect [6]. The weight of this phenomenon in the overall balance of the charges present in the dielectric depends on the type of facing materials, the electric field, the temperature and the quality of the surfaces. Furthermore, depending on the purity of the crystalline lattice of the dielectric material and its aging state, electron traps may be present in the bulk of the insulating layer [7,8]. Also this phenomenon can play an important role in determining the electric field profile in the insulation of a cable in operation. This phenomena depend on time, therefore, the

distribution of the electric field in an HVDC cable depends significantly on dynamic phenomena such as the variation of load current or applied voltage. Particular importance is given to the study of the evolution of the electric field during Reversal Polarity (PR) and Transient Over-Voltage (TOV) events.

In Chapter 1, a coupled thermal and electrical model is described useful for the analysis of space charge and electric field distribution in HVDC cables and accessories under dynamic conditions. The thermal model is based on the Fourier equation for conduction in solids and considers conductive heat exchange between the outer surface of the modelled component and the outside. The electric model is based on the continuity equation of the current in solid dielectrics, on the Gauss equation for the electric field, on Ohm's law and on the Schottky injection of charges at the interfaces. This model is less detailed than the microscopic models based on bipolar charge transport. However, thanks to its greater simplicity, it can be useful to study the evolution of space charge and electric field distribution in complex geometries and over relatively long transient. As explained in detail in the first chapter, this type of model also can be used to study phenomena requiring a three-dimensional modeling such as the time trend of the electric field distribution in the joints or the effect of thermal conduction along the cable axis. A limited number of parameters is needed to study the behavior of a dielectric using a conductivity model. Thanks to this aspect, a method is approachable in which the parameters of the model can be calibrated by comparing the results of experiments and simulations for certain case studies. This approach aims to determine parameters for the conductivity model of the dielectric capable of predicting macroscopic phenomena such as the triggering of partial discharges.

In any case, it is almost impossible with a model to take into consideration the particular behaviour, from the point of view of the accumulation of space charge, of a dielectric subjected to aging. For this reason, the improvement of space charge measurement techniques both on flat specimens and on model and full size cables plays an important role in this research. The methods considered most reliable for the measurement of space charge both by most of the researchers working in this field and by the recommendations of organizations such as the Cigrè and the IEEE are the following:

- Thermal Step Method (TSM);
- Pulsed Electro-Acoustic (PEA) method.

This research project focuses on the use and development of the PEA method. In chapter 2, the operating principle and the particularities regarding the use of the PEA method for flat samples and cables are described in detail. This chapter contains both a review on the PEA method and the results of measurements carried out using a commercial device at the LEPRE laboratory (Laboratorio di Elettrotecnica e di Prove Elettriche) at the DI (Dipartimento di Ingegneria) of the University of Palermo.

From bibliographic research and the experiments carried out at the LEPRE laboratory, it can be concluded that, to date, the commercial PEA cells are suitable for thin specimens or for cables. As mentioned above, temperature and its spatial gradient play an important role in the accumulation of space charge. PEA systems for thin flat specimens are not suitable for the application of temperature gradients due to the low thermal resistance of the sample. In the case of PEA systems for cables, it is possible to heat up the conductor and therefore apply a temperature drop over the insulation thickness. However, as demonstrated by the experience, these measurements have a low level of replicability and reliability. For these reasons, it has been considered appropriate to attempt to design a PEA system for thick flat specimens with the possibility of applying temperature drops between the flat surfaces. The design of a novel PEA system with these peculiarities has been described in Chapter 3.

In presence of an air cavity inside a dielectric material subjected to HVDC stress, PD may occur under certain conditions. Unlike what happens under AC stress, the inception conditions for PD under DC voltage depends on the conductivity phenomena and therefore on the space charge and electric field distributions. For this reason, the last part of this research project has been focused on PD measurements on flat and cable samples with the aim of using the their inception and the repetition rate as an indirect measurement of electric field. The specifications and the results of these experimental campaigns are detailed in Chapter 4. As explained in this chapter, within a certain range, the occurrence of PD within defects in the bulk of dielectric materials seems to be predictable using conductivity models.

This PhD thesis ends with conclusions containing a synthesis of the results achieved and a description of possible future developments of the research conducted.

# Main goals

As anticipated in the introduction, this thesis work is focused on the study of the phenomenon of space charge accumulation, considered one of the main factors that cause the aging of the insulation of HVDC cables. For this reason, research was conducted during the PhD course with the following main objectives:

- Based on literature research and computational analysis, assess the impact of space charge accumulation phenomena on the electrical stress to which the insulation of cables and HVDC accessories are subjected.
- Study state-of-the-art methods for measuring space charge, highlighting the performance and limitations of the devices currently available on the market. Among the various methods, deepen the knowledge on the Pulsed Electro-Acoustic (PEA) method also through its practical use in the laboratory.
- Develop an innovative PEA apparatus useful to carry out space charge measurements in configurations as close as possible to those in which the dielectric of HVDC cables and accessories is found in operation.
- Study the interaction between different phenomena in dielectrics such as the accumulation of space charge and the onset of partial discharges.

# Chapter 1
# Space charge accumulation in HVDC cables and accessories

This chapter describes a coupled thermal and electric model for the evaluation of space charge and electric field distributions in dielectrics under HVDC voltage stress. The content of this chapter is based on the works of the author et al. entitled "*The Effect of the Axial Heat Transfer on Space Charge Accumulation Phenomena in HVDC Cables*" [9], "*Space charge accumulation in undersea HVDC cables as function of heat exchange conditions at the boundaries–water-air interface*" [10], "*Investigation on partial discharges in HVDC cables after polarity reversal events*" [11], "*Polarity reversal in HVDC joints-the effect of the axial thermal conduction*" [12], "*The effect of Transient Over Voltages on the Partial Discharges activity in HVDC joints*" [13] and "*Effect of Heat Exchange Transient Conditions With Moving Water-Air Interface on Space Charge Accumulation in Undersea HVdc Cables*" [14].

Space charge accumulation within the dielectric layer is one of the most important causes of fault in HVDC transmission line [15]. This phenomenon is essentially due to the following reasons:

- The thermal gradient establishing on a loaded HVDC cable determines a conductivity and permittivity gradient leading to the accumulation of space charge in the bulk of the dielectric [2];
- Under high electric field gradient, injection of charges from electrodes occurs, this phenomenon depends on the type of interfacing materials and on the roughness of the facing surfaces [16];
- The charge carriers injected at the electrodes can remain in proximity of these, migrate leading to a heterocharge accumulation in proximity of the opposite electrode or remain in the bulk of the insulation in traps due to inhomogeneities or impurities within the crystalline lattice of the material [17].

In Figure 1.1, the typical stratigraphy of a full size HVDC cable for land application is shown. Since the permittivity of dielectric materials does not vary significantly with temperature and applied voltage, the radial electric field distribution in the insulation of a HVAC cable only depends on the position following an hyperbolic law as shown below [2]:

$$E_{AC}(r) = \frac{U_0}{r ln\left(\frac{r_0}{r_i}\right)} \tag{1.1}$$

Where $E_{AC}$(r) is the radial component of the electric field at radius $r$, $U_0$ is the design voltage of the cable across the dielectric, $r_i$ is the cable insulation inner radius, $r_0$ is the cable insulation outer radius. The radial electric field distribution in the insulating layer of an HVDC cable can be similar to that found in an HVAC cable only in the absence of a temperature gradient. However, also in this case, the dependence of the electric conductivity on the electric field as well as the injection and trapping phenomena mentioned above would lead to an accumulation of space charge and therefore to a deformation of the electric field profile with respect to that which occurs in the case of HVAC cables.

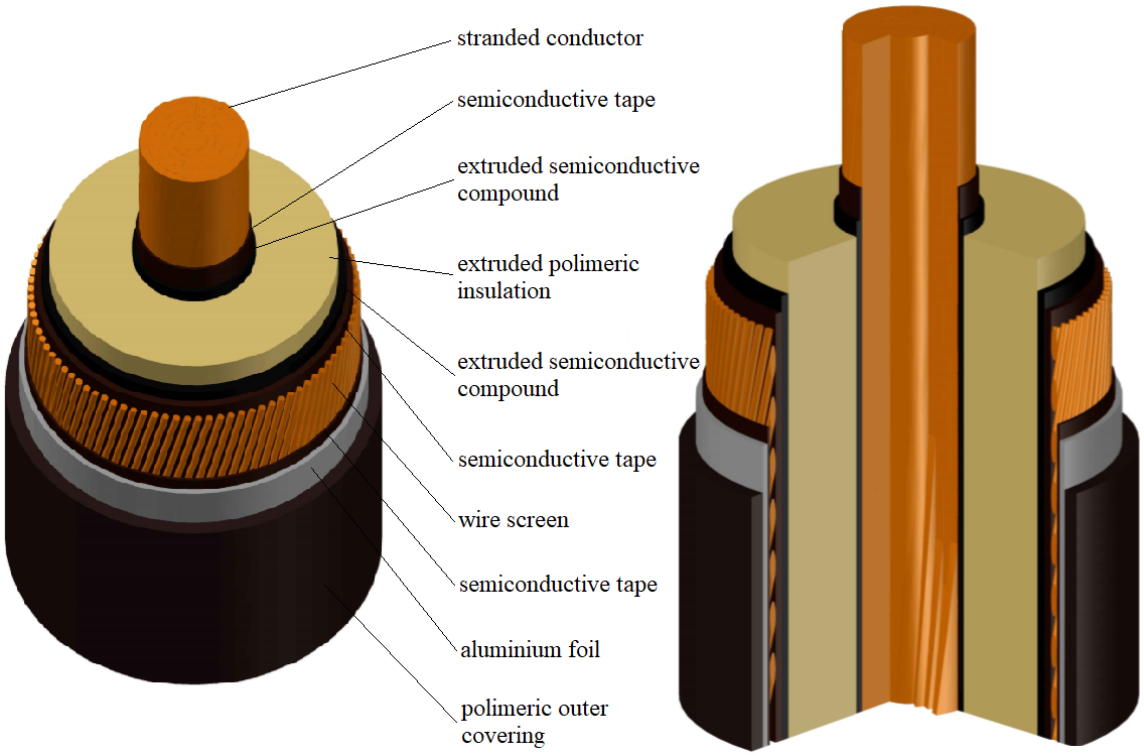


***Figure 1.1.*** *Typical stratigraphy of a full size HVDC cable*

The electrical conductivities of the commercially used dielectric materials are dependent on the temperature and electric field with an exponential law. In particular, the electrical conductivity grows in the range of the operating temperatures up to two orders of magnitude. The following equation is one of the most used to characterize the electrical conductivity of a dielectric as a function of temperature and electric field [2]:

$$\sigma(T, E) = \sigma_0 \exp\left[a(T - T_0) + b(E - E_0)\right] \tag{1.2}$$

where $\sigma(T,E)$ is the electrical conductivity of the dielectric at the temperature $T$ and under the electrical field $E$, $\sigma_0$ is the electrical conductivity at the temperature $T_0$ equal to 20°C and under the electrical field $E_0$ equal to 0 V/m. The coefficients $a$ and $b$ are respectively the thermal and electrical dependence coefficients for the conductivity. As reported in literature, the value of $b$ depends on the temperature. For many commercial dielectric materials, the values of $b$ can be expressed by means of the following equation [10]:

$$b = c(T - T_0)^2 + d(T - T_0) + e \tag{1.3}$$

where c, d and e are constants depending on the material.

Another equation widely used for calculating the electrical conductivity of dielectric materials is the following [18]:

$$\sigma(T, E) = A \cdot exp\left(\frac{-\varphi q}{k_b T}\right) \cdot \frac{sinh\,(B|E|)}{|E|} \tag{1.4}$$

where $A$, $\varphi$ and $B$ are respectively a material depending parameter, the thermal activation energy and the field constant, $q$ is the elementary charge, $k_b$ is the Boltzmann's constant and $E$ is the magnitude of the electric field.

The electric field distribution within a dielectric material depends on the applied voltage and on space charge distribution as shown from the definition of voltage and the Gauss law for electric field below reported:

$$E = -\nabla \mathrm{V} \tag{1.5}$$

$$\nabla \cdot (\varepsilon_0 \varepsilon_r E) = \rho \tag{1.6}$$

where $V$ is the voltage over the insulation layer, $\varepsilon_0$ is the vacuum permittivity, $\varepsilon_r$ is the relative permittivity.

Then the current density $J$ can be calculated from the Ohm's law for the current density:

$$J = \sigma(T, E) \cdot E \tag{1.7}$$

where $\sigma(T,E)$ is calculated from the equation (1.2) or (1.4) considering the local temperature at the current time. From the expression (1.7), it is understood that, in the case of a loaded cable, where a temperature gradient is established, the spatial distribution of $J$ cannot have the same shape as the distribution of $E$.

Moreover, the space charge density and the current density are related by the current continuity law as follows:

$$\nabla \cdot J = -\frac{\partial \rho}{\partial t} \tag{1.8}$$

By solving iteratively the set of equations ranging from (1.5) and (1.6) to (1.8), it is shown that, if a spatial variation of electrical conductivity is established, a transient is incepted which leads, through the accumulation of space charge, to the achievement of an equilibrium electric field distribution.

Combining Ohm's law for current density, Gauss's law for spatial charge and the law of continuity of the current, it is shown that, once reached steady state condition, if there is a permittivity and conductivity gradient, there is a space charge density in accordance with the following equation:

$$\sigma E \, \nabla \left( \frac{\varepsilon_0 \varepsilon_r}{\sigma} \right) = \rho \tag{1.9}$$

Considering stable thermal and electrical boundary conditions, the time required to reach an equilibrium electric field distribution depends on the time constant $\varepsilon_0 \varepsilon_r / \sigma$ of the material, which in turn, in a loaded cable, depends on the position. This also implies that the higher the average temperature in the insulation of an HVDC cable, the faster the electric field will tend to reach an equilibrium distribution.

A semi empirical expression for the radial component of the electric field $E_r(r)$ across the dielectric of a HVDC cable under thermal and electric stress is the following [2]:

$$E_r(r) = \frac{\delta U_0 (r/r_0)^{\delta - 1}}{r_0 [1 - (r_i/r_0)^{\delta}]} \tag{1.10}$$

where:

$$\delta = \frac{\frac{a \Delta T}{ln(r_0/r_i)} + \frac{b U_0}{(r_0 - r_i)}}{1 + \frac{b U_0}{(r_0 - r_i)}} \tag{1.11}$$

and $\Delta T$ is the temperature difference between the inner and the outer radius of the dielectric. In Figure 1.2, the typical the electric field distributions over the radius of an HVDC cable with and without load is shown. As it can be seen, the slope of the radial electric field profile can reach the inversion under certain load conditions. Under these conditions, the maximum electric field value is reached near the interface between the

dielectric and the external semiconductive layer, as opposed to what happens in an HVAC cable.

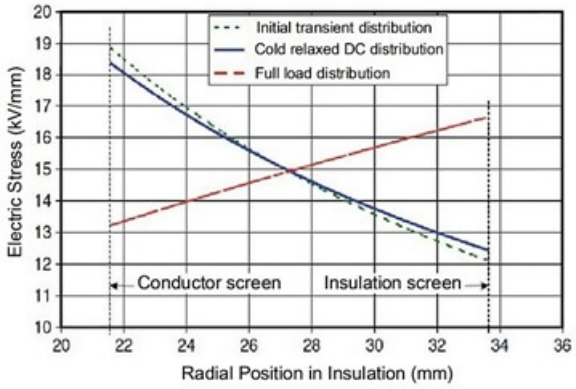


***Figure 1.2.*** *Example of no-load and full load electric field distribution in a HVDC cable – the figure is reproduced from [19]*

The expression (1.10) can be used to evaluate the radial electric field distribution in a DC cable under thermal and electrical stress without considering other phenomena involving the injection or the accumulation of space charge strictly related to the interfaces quality or the materials properties.

In real applications, other phenomena concur to the establishment of space charge in the dielectric such as the injection of charge carriers by the electrodes, the separation of charges by means of thermal ionization effects the trapping and de-trapping inside the bulk.

The injection of charges at interfaces depends on the number of electrons with a sufficient thermal energy to overcome the coulombic potential barrier. The extent of this phenomenon, known as Schottky injection, depends on the electron affinity of the interface materials, the effect of the coulombic image force and the potential energy due to the applied electric field. In presence of a high electric field, the height and the thickness of the potential barrier decrease, therefore the probability of electron injection through the interface increases. In presence of high electrical field, electrons could pass the potential barrier by the means of tunnel effect [20].

The charge injection from the electrodes leads increase or decrease of the electric field close the interfaces depending on the mobility of the charge carriers. A growth of the electric field near the electrodes typically occurs at low temperatures. Under these conditions, the transport effects are less relevant and homocharges are accumulated at

interfaces. The estimation of the mobility of charge carriers can be carried out from a depolarization curve obtained by means of space charge measurements.

The thermal ionization of impurities and the spatially inhomogeneous electric polarization can also contribute to the forming of space charge.

The above summarized phenomena taking place in HVDC cables lead to the forming of free space charge that can be trapped in potential gap due to the presence of physical or chemical defects. The typical crosslinking by-products of XLPE insulated cables are one of the main types of defects that enhance the accumulation of space charge. The degassing of the insulation material is a good solution to reduce the presence of crosslinking by-products. Trap depths can be estimated applying the Pulsed Electro Acoustic (PEA) method for space charge measurements in different scenarios: equilibrium, charging and discharging [21].

The set of the above mentioned phenomena leads to a not negligible modification of the radial electric field distribution inside the insulation of a HVDC cable. These phenomena play an important role during some transient scenarios occurring during the lifetime of a HVDC cable, such as polarity inversion and overvoltage transients [22].

At the start of a transient occurring after a relatively lasting steady state, the shape of the electrical field along the cable's radius is a combination of the pattern due to the thermal gradient and of the effect of local space charge accumulation phenomena. Most of the transient phenomena that could occur in a HVDC cable are characterized by a duration of several orders of magnitude lower than the system response time. In the light of the above, the local electric field during a transient could be significantly higher than the rated value due to the combined effect of the space charges accumulated and of the transient voltage behavior. For example, one of the most stressful scenarios for a HVDC line is the voltage Polarity Reversal (PR) that could occur due to a power flow inversion carried out by the means of Current Source Converters (CSC) [2]. The use of a Voltage Source Converter (VSC) enables the possibility to invert the power flow in a DC cable without voltage polarity inversion; therefore, this technology has played a decisive role in the growing demand of extruded HVDC cables. Nevertheless, the polarity reversal is still one of the most frequent causes of fault in HVDC connections. The first reason is the occurrence, even if VSC technology is used, of pole-to-ground fault on the DC link or faults inside the neighboring AC grid. The second one is related with the maintenance of existing HVDC

lines with the replacement of mass impregnated cables with extruded cables keeping the CSC technology for the AC/DC conversion. At the beginning of a PR scenario, the inverted electric field shape due to the thermal gradient and to the other above-mentioned phenomena, is added to the new conditions related to the polarity inversion. Under certain conditions depending on thermal gradient, age level and characteristics of the cable, the maximum local electric stress could significantly exceed the rated value leading to the ageing of the cable. Space charges could be accumulated near defects, such as crosslinking by-products, leading to Partial Discharge (PD) phenomena and accelerating the deterioration of the cable insulation until it causes its breakdown [23]. Since the phenomena described above may represent one of the main causes of failure in HVDC cables, it is advantageous that the space charge measurement be considered an integral part of the qualification procedures of the aforementioned cables. As it will be specified below, an international standard has been published in 2017 in order to propose an accredited protocol for space charge measurements during the cable testing [24]. In order to study the evolution of space charge and electric field distributions in different configurations and scenarios, investigations were carried out starting from models developed by means of commercial fem software. The following sections describe the boundary conditions, the peculiarities of the model used and the results of the main scenarios studied.

## 1.1 Calculation of the time trend of the electric field distribution in an HVDC cable considering the axial heat transfer

As mentioned above, a radial temperature gradient in the insulating layer of an HVDC cable leads to the accumulation of space charge in the bulk of the insulation and therefore to a deformed profile of the electric field compared to the hyperbolic one that would occur with constant temperature. Hitherto, many researchers have focused their attention to the effect of the thermal gradient on the distribution of the electric field. Most part of these studies are based on a unidimensional characterization of the temperature distribution over the insulation layer obtained in accordance with the indication of the standards IEC 60287 [25]. The approach proposed by these standards is based on the calculation of thermal resistances per unit length and it is therefore applicable to a lying section of one or more cables. However, it should be noted that the current rating of HVDC cables at voltages higher than 5 kV is not covered by a dedicated IEC standard. The Cigrè brochure 640 pays attention to this lack and to the need to consider the effect of the thermal drop over the

insulation layer in the current rating of HVDC cables. The same brochure emphasizes that the longitudinal heat flow through the cables can play an important role in the rating where axial discontinuity elements bring to a variation of the outgoing radial heat flux. In order to take into account the axial heat transfer in joint bays, some researchers have proposed a 3D F.E.M. model. It has been shown that the weight of the space charge contribution in the insulation of HVDC cables due to the thermal gradient compared to that due to other factors such as the injection of charge from the electrodes increases with the cable diameter. On the other hand, the thicker the insulation layer, the less effective the above-mentioned space charge measurement method is. For this reason, at the state of the art, the assessment of these phenomena in large size HVDC cables by means of simulations can offer information that can be added to those obtainable from measurements on sample or less thick cables.

In this section, attention is focused on the conditions that can lead to local and/or temporary peaks of thermal gradient in the dielectric layer of HVDC cables and the possibility to reach high levels of electric field near its external surface is verified. A discontinuity along the cable axis of the external heat exchange parameters can lead to the achievement of a local peak of temperature drop. In certain conditions, the axial thermal conduction can prevail on the radial one due to the high thermal conductivity of metals in comparison to that of polymeric materials. The area near a joint, the crossing by the cable of an interface between two different means or local external heat or cold sources are potentially cases in which axial heat transfer can play an important role in defining the highest electric field within the insulation of a cable. In Figure 1.3, the effect on the temperature drop of a hot spot is shown. Within this thesis, a case study has been described considering a full size cable partly immersed in water and partly in air.

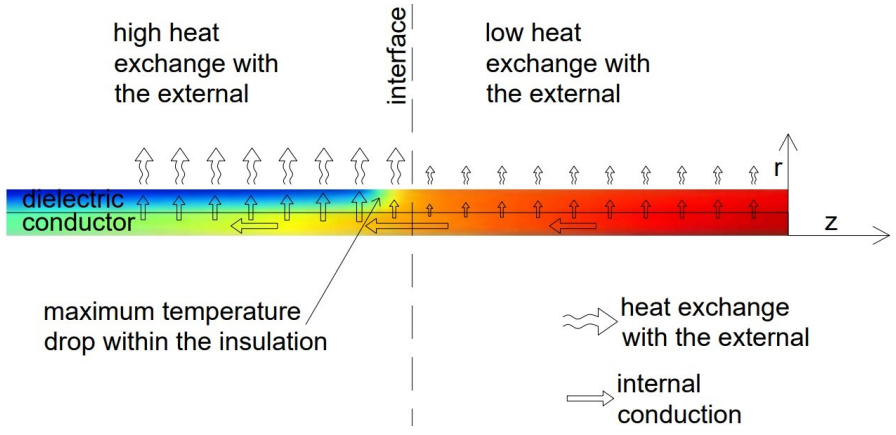


***Figure 1.3.*** *Schematic of prevalent axial conduction close an interface between two external means - the figure is reproduced from [9]*

In order to study the above-described phenomenon considering the axial heat transfer and its effects on the space charge and electric field distributions, a 2-D axial symmetric thermal model has been coupled with multiple 1-D electrical model and implemented in Matlab®. The portion of cable under investigation is divided into a discrete number of cross sections. The model is based on the hypothesis that heat can be transmitted radially or axially while the current in the dielectric circulates only radially. This hypothesis can be considered acceptable as axial external temperature gradients may occur while the voltage at the conductor and at the screen does not vary significantly along the axis.

The temperature distribution vs. time is calculated by means of the thermal conduction law in an axial-symmetric cylindrical coordinate system:

$$\frac{1}{r}\frac{\partial}{\partial r}k(r)r\frac{\partial T(r,t)}{\partial r}+\frac{\partial^2 k(r)T(r,t)}{\partial z^2}+q'''(r,t)=rho(r)C(r)\frac{\partial T(r,t)}{\partial t} \quad (1.12)$$

where *r*, *z*, and *t* are respectively the radial, the axial, and the time coordinates, *k(r)* is the thermal conductivity, *q‴(r,z,t)* is the thermal power density, *rho(r)* is the mass density, and *C(r)* is the specific heat. Equation (1.12) has been discretized in a linear system of equations through the finite differences method and iteratively solved for each time step.

Whilst the thermal model is applied to the entire cable segment, the domain of the electric model includes only the layers between the inner and the outer semiconductive layers and assumes that voltage is applied between these two layers.

The radial component of the electric field is calculated through the definition of voltage and the Gauss's law expressed in cylindrical coordinates and assuming axial symmetry and neglecting the axial derivatives:

$$\int_{rin}^{rout} E_r(r,z,t)\,dr = U(t) \quad (1.13)$$

$$\frac{1}{r}\frac{\partial}{\partial r}[r\varepsilon_r(r)E_r(r,z,t)] = \frac{\rho(r,z,t)}{\varepsilon_0} \quad (1.14)$$

where $\varepsilon_r(r)$ is the radius dependent relative permittivity of the material, and *ρ(r,z,t)* is the radius and axial dependent space charge density, *rin* and *rout* are the inner and the outer radius of the dielectric layer respectively as well as *U(t)* is the applied voltage. Equations (1.13) and (1.14) are discretized using a subset of the mesh used for (1.12) in order to have a temperature and electric field value for each node belonging to the domain of the electric model. The set of discretized equations for each node of the electrical model domain constitute a single system of linear equations that is solved for each time step.

As an initial condition, the space charge is considered equal to zero in the whole the domain. Consequently, the first radial distribution of the electrical field follows a hyperbolic law.

Once known, the temperature and the electric field in each node, the conductivity distribution can be calculated from equations (1.2) and (1.3) or (1.4) in order to obtain the following:

$$\sigma(r,z,t) = \sigma(T,E) \tag{1.15}$$

The radial component of the current density through the dielectric, $J_r$, can be therefore calculated from the Ohm's law that can be simply applied to each node:

$$J_r(r,z,t) = \sigma(r,z,t) * E_r(r,z,t) \tag{1.16}$$

As it can be noted from (1.16), the current field depends on the electrical conductivity distribution and therefore on the thermal and electrical field. For most commercially used dielectric materials, the electrical conductivity is more dependent on the temperature than on the electric field.

By considering the assumption above, the approximation of the current continuity equation expressed in cylindrical coordinates can be written as follows:

$$\frac{1}{r} \cdot \frac{\partial}{\partial r} r J_r(r,z,t) = -\frac{\partial \rho(r,z,t)}{\partial t} \tag{1.17}$$

As it can be noted from the (1.17), two values of $J_r$ are needed for each discretized equation in $\rho$, therefore, this equation is discretized with the finite difference method and is centred on the midpoint between two consecutive radial nodes among those defined for the equations for calculating the temperature and the electric field. The obtained linear system of equations provides the distribution of the space charge inside the dielectric that can be introduced in the system obtained from the (1.13) and (1.14) at the subsequent time step. the method just described is implemented in Matlab® and is validated by comparison with the results obtained by commercial fem software on identical case studies. The development of a model made starting from the differential equation describing the physics of the phenomenon involves several advantages such as the possibility of automating the execution of a large number of case studies. Another important advantage is that of having a lighter calculation system suitable to study relatively durable transients in cases characterized by simple geometry such as that of a cable.

In Table 1.1, the main thermal properties of the materials composing the cable considered in the case study are reported whilst, in Table 1.2, the main electrical properties are reported for the layers included in the domain of the electrical model.

***TABLE 1.1.*** *Geometrical and physical properties of the cable taken as the case study.*

| Layer | Description | External radius [mm] | Mass density [kg/m$^3$] | Specific heat [J/(kgK)] | Thermal conductivity [W/(mK)] |
|---|---|---|---|---|---|
| **1** | copper conductor | 20 | 8960 | 385 | 390 |
| **2** | inner semicon | 21 | 1180 | 1900 | 0.6 |
| **3** | thermoplastic dielectric | 51 | 1400 | 1714 | 0.2857 |
| **4** | outer semicon | 52 | 1180 | 1900 | 0.6 |
| **5** | swelling tape | 53 | 930 | 1900 | 0.6 |
| **6** | copper metallic screen | 55 | 8960 | 385 | 390 |
| **7** | swelling tape | 56 | 930 | 1900 | 0.6 |
| **8** | aluminum laminate | 58 | 2700 | 896 | 290 |
| **9** | PVC outer covering | 62 | 1400 | 1214 | 0.167 |

***TABLE 1.2.*** *Electrical properties of the cable taken as the case study.*

| Layer | Description | Permittivity | Reference Resistivity (@20 °C) [Ohm*m] |
|---|---|---|---|
| **2** | inner semicon | 5000 | 2.18 |
| **3** | dielectric | 2.5 | 1.4 × 1014 |
| **4** | outer semicon | 5000 | 2.18 |
| **5** | swelling tape | 5000 | 2.18 |

For the analysis of this case study, the equation (1.2) has been chosen to obtain the electrical conductivity. The values of $b$ have been calculated in accordance with equation (1.3) and adopting the following coefficients: $c = -4.13 \times 10{-}11$ m/(V*K$^2$), $d = 2.83 \times 10{-}9$ m/(V*K), $e = 1.25 \times 10{-}8$ m/V. These parameters are compatible with those of a thermoplastic dielectric material [2].

In order to describe the most significant cases in which axial heat conduction can play an important role in achieving local electric field peaks, several scenarios have been studied. Of these scenarios, the two most significant are described below. For both scenarios below, the boundary conditions represented in Table 1.3 were used.

The effect of axially variable thermal boundary conditions has been investigated by considering a portion of HVDC cable with a length of 10 m. At the cable's outer surface, a convective heat exchange has been considered, whilst, at the axial boundaries, an adiabatic condition has been applied. A sensibility analysis has demonstrated that the increase of the domain's axial length does not modify the results. Therefore, in order to optimize the calculation effort, the length of the modeled cable' segment has been limited to 10 m whilst the axial discretization has been optimized. A moving cable-water-air boundary is considered. In particular, the water and the air outside the cable, change over time with a sinusoidal law around the middle of the segment, with a period equal to 20 s and a peak-to-peak value equal to 0.6 m. This is accomplished by using the appropriate convective heat exchange condition on the external boundary of the cable. The duration of the transient is set equal to 48 h. Typical values of convection coefficients for calm air and water are considered. The section immersed in water, which from now on called as "cold segment", is cooled by water at a temperature of 15 °C with a convective exchange coefficient of 100 W/($m^2$*K). The remaining cable portion, which from now on referred as "hot segment", is cooled by air with a temperature of 25 °C and the convective exchange coefficient is set to 8 W/($m^2$*K). As shown in reference [26], a difference up to 10 K between the monthly averaged values of temperatures of sea surface and free air is consistent with conditions where the upwelling of cool water from the bottom into the sea surface occurs.

***TABLE 1.3.*** *Boundary conditions valid for both scenarios investigated*

| **Condition** | **Value** |
|---|---|
| **Duration of the transient [h]** | 48 |
| **Cable length [m]** | 10 |
| **Section immersed in air [m]** | From 5 ± 0.3 to 10 |
| **Section immersed in water [m]** | From 0 to 5 ± 0.3 |
| **Wave period of the moving interface [s]** | 20 |
| **Water temperature [°C]** | 15 |
| **Water convective heat exchange coefficient [W/($m^2$*K)]** | 100 |
| **Air temperature [°C]** | 25 |
| **Air convective heat exchange coefficient [W/($m^2$*K)]** | 8 |
| **Voltage [kV]** | 510 |

The two scenarios analyzed consist in the application of different boundary conditions that vary over time in terms of current and voltage.

### 1.1.1 Scenario 1 – Sudden load variation

In the first scenario, after applying the rated voltage of 510 kV with a step function, a current of 1200 A flowing through the conductor is set. After 24 h from the beginning of the transient, the current is increased up to 1920 A (+ 60%) with a 10 s ramp. The current of 1920 amperes corresponds to the ampacity calculated for the cable used as an example for this case study.

The purpose of this study is to assess the time trend of the electric field and of the space charge in the dielectric layer following a sudden load increase. In particular, attention is focused on local phenomena conditioned both by the temporal variation of the current and by the variation along the axis of the heat exchange conditions between the surface of the cable and the outside. In Figure 1.4, the temperature drop over the insulation thickness at the end of the transient is shown, as a function of the axial coordinate. As it can be observed, the maximum temperature drop is reached in the cold segment just below the average level of the interface. The presence of the interface seems to influence a section of the cable with a length of approximately 6 m. In this case study, the entity of the radial thermal gradient reaches about a +14% with respect to the value in deep waters and +2.3% with respect to the value immersed in air. As can also be observed from the Fig. 1.4, due to the increase in the conductor electrical resistivity at high temperature, a higher thermal power generation in the cable core in the hot region leads the radial temperature drop to greater values in the hot region. From the simulations, it has been demonstrated that the effect of axial heat transmission is more significant with lower load values. This is due to the fact that, with higher currents, the increase in conductor resistivity, especially in the hot region, counterbalances the effect of axial heat transmission.

As shown in Fig. 1.5, during the load transient, the temperature drop over the radius never exceeds the maximum value achieved in steady state at rated conditions. On the other hand, as illustrated in the Fig. 1.6, the temperature drop is concentrated near the conductor during the first hours after the load increase. This phenomenon is related to the greater thermal diffusivity of the copper conductor compared to the polymeric material insulation and it is less evident in the case of an aluminum conductor.

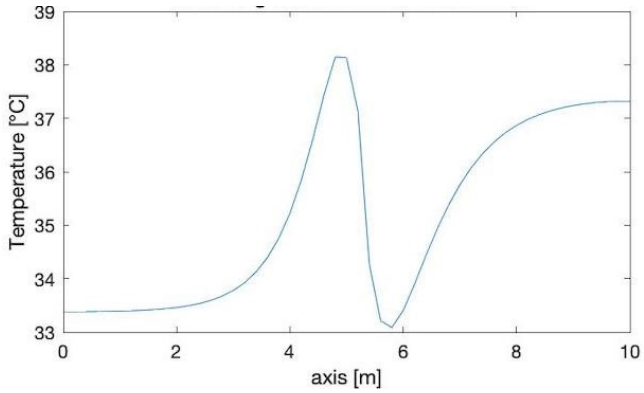


***Figure 1.4.*** *Scenario 1 - Temperature drop vs axial coordinate at the end of the transient t = 48 h, I = 1920 A - the figure is reproduced from [14]*

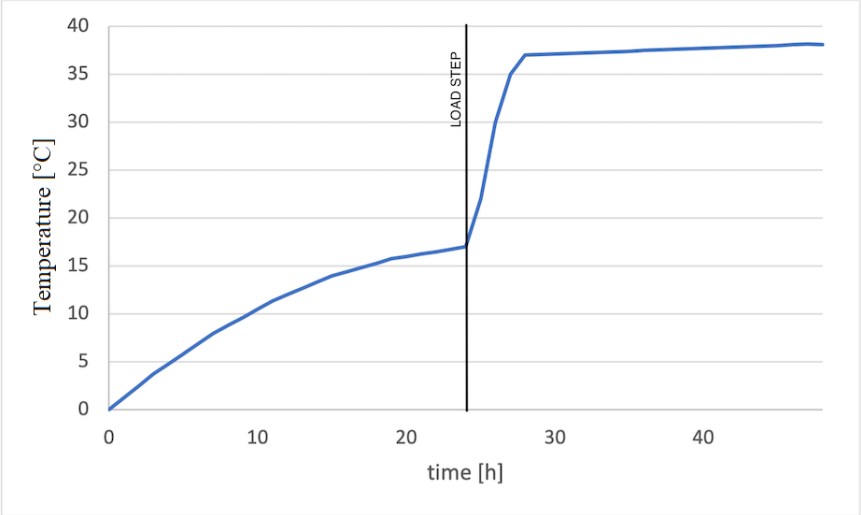


***Figure 1.5.*** *Scenario 1 - Time trend of the temperature drop over the insulation at the water-air interface - the figure is reproduced from [14]*

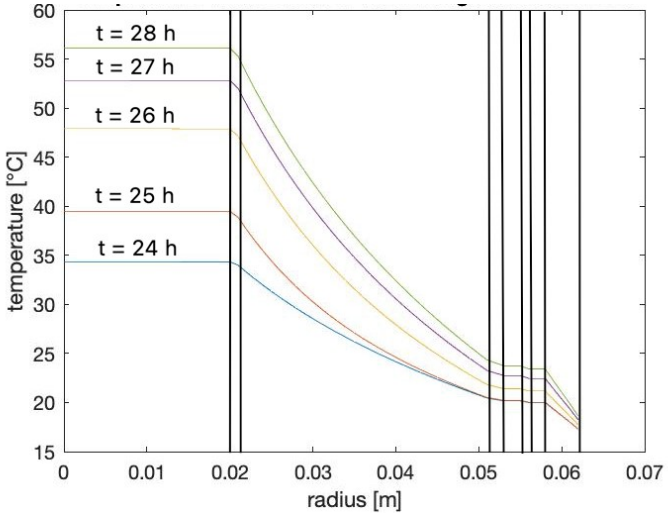


***Figure 1.6.*** *Scenario 1 - Radial temperature distribution at the average interface level after the load increase from t = 24 h*

As shown in the Fig. 1.7, the local and temporary increase in thermal gradient near the interface between the inner semiconductor and the dielectric leads the space charge density in this area to reach a peak during the first hours after the load abrupt increase. In this figure, the space charge distribution at the average interface level over time is shown. The results show that the highest concentrations of space charge lay in proximity of the interfaces between the dielectric and the semiconductive layers. This is because the abrupt variation in permittivity. To emphasize the role of the space charge accumulation within the bulk of the dielectric, the peaks at the boundaries of the dielectric layer have been removed from the illustration. The space charge found is positive across the insulation thickness, therefore, the effect of the temperature dependency of the electric conductivity in dielectrics under HVDC voltage and load enhance the accumulation homocharges near the inner electrode and heterocharges in proximity of the outer one.

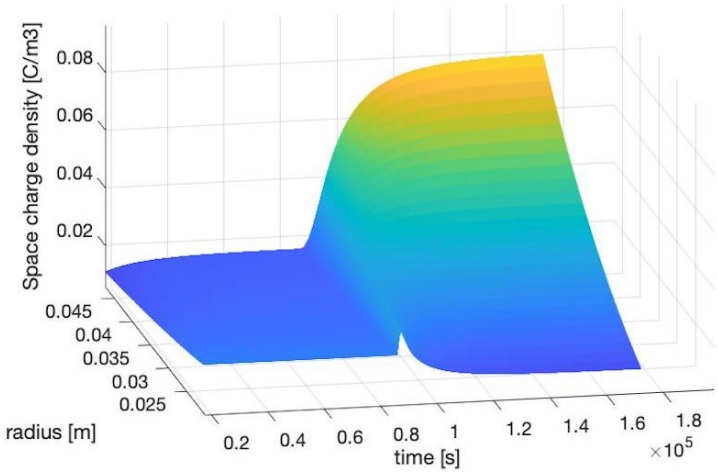


***Figure 1.7.*** *Scenario 1 - Radial space charge distribution at the average interface level vs time - the figure is reproduced from [14]*

As it can be seen in Figure 1.8, the aforementioned local and transient peak in space charge density close to the inner semiconductive layer does not cause an analogous behavior of the electric field distribution.

At the beginning of the transient, the electric field vs radius profile assumes a hyperbolic-like pattern with maximum value in proximity of the inner surface. After approximately 4 h, this pattern has been definitively modified from the accumulation of space charge inside the dielectric and an equilibrium is reached with the maximum value reached near the outer surface. Immediately after the abrupt increase in load, the amount of space charge grows further leading the maximum electric field at the outer surface to overcome the initial maximum value reached at the inner boundary.

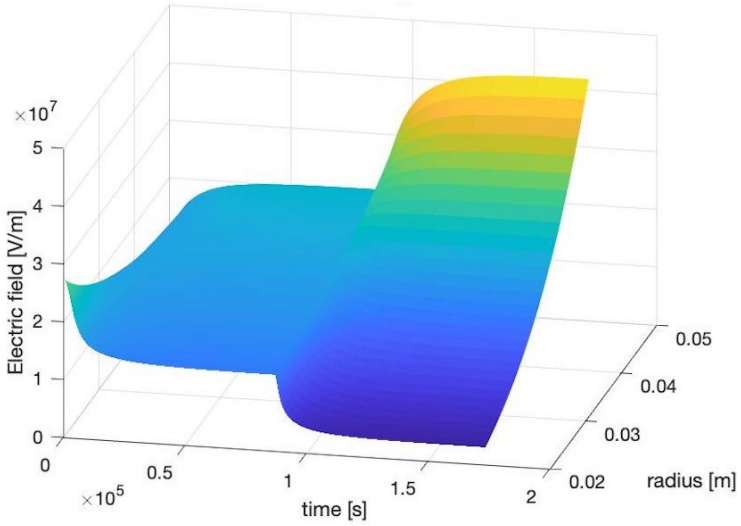


***Figure 1.8.*** *Scenario 1 - Radial electric field distribution at the average interface level vs time - the figure is reproduced from [14]*

In Figures 1.9-1.11, the radial electric field distributions at different time steps and in different axial positions are shown. At the end of the simulated transient, the maximum electric field is reached on the outer surface of the dielectric layer for all the cross sections. As it can be observed from the figures, the maximum electric field value is reached just below the air-water average interface level.

For the simulated case study, this value is equal to 42.3 kV/mm and exceeds of 3 % the maximum electric field in the sections immersed in air, where the peak is equal to 41.1 kV/m. In the part of the cable immersed in water, at 5 m from the average interface level, the maximum electric field value is equal to 37.7 kV/mm.

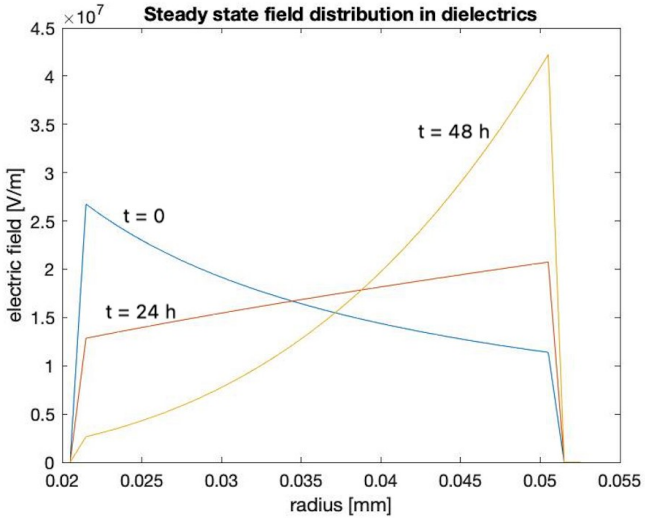


***Figure 1.9.*** *Scenario 1 - Inversion of the slope of the electric field profile – just below the interface - the figure is reproduced from [14]*

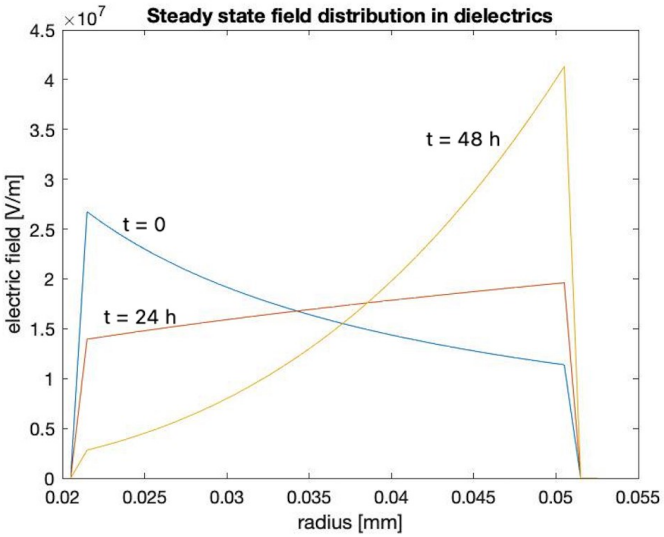


***Figure 1.10.*** *Scenario 1 - Inversion of the electric field profile – section immersed in air - the figure is reproduced from [14]*

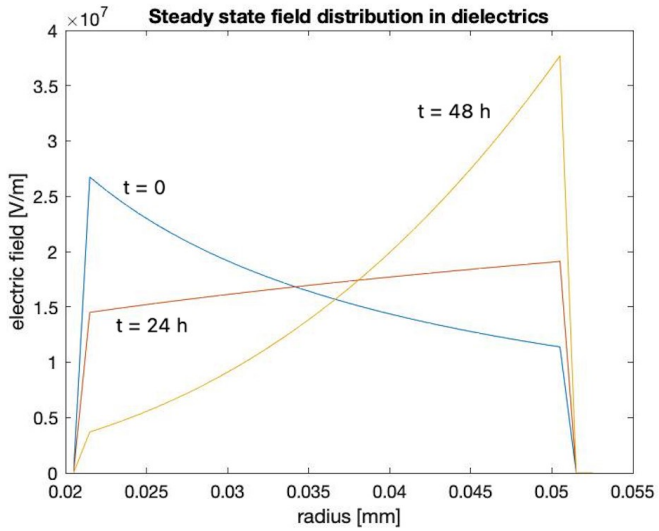


***Figure 1.11.*** *Scenario 1 - Inversion of the electric field profile – section immersed in water - the figure is reproduced from [14]*

In Figures 1.12 and 1.13, the two profiles show the space charge spatial distribution in the middle and at the end of the transient, respectively. As mentioned above, at low loads, the space charge accumulation is dominated by the temperature drop. As it can be seen from the Figures 1.12 and 1.13, the effect of the axial thermal conduction is more evident at the end of the transient than after the first 24 hours. Once reached the first steady state after 24 h from the beginning, the peak in space charge density is reached just below the average interface level and exceed its maximum value in the air-immersed region by 2.3 %. This percentage reaches the value of 5.6 % at the end of the transient.

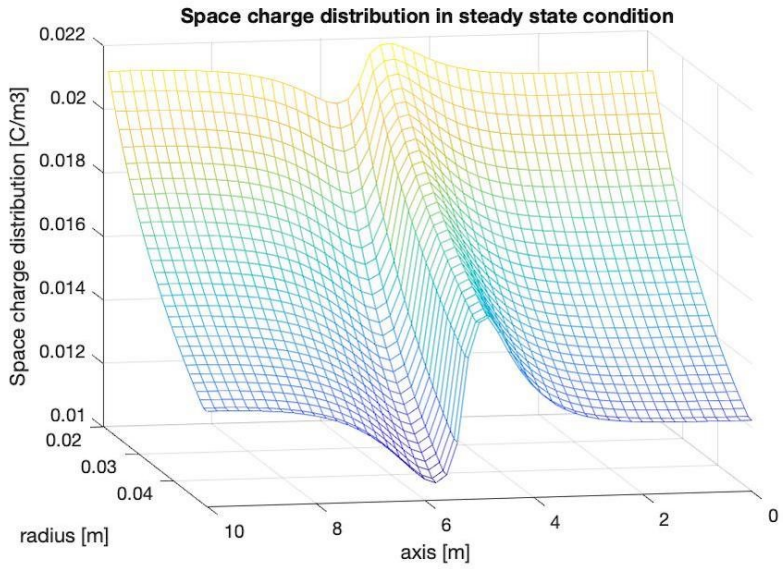


***Figure 1.12.*** *Scenario 1 - Space charge spatial distribution - t = 24 h - the figure is reproduced from [14]*

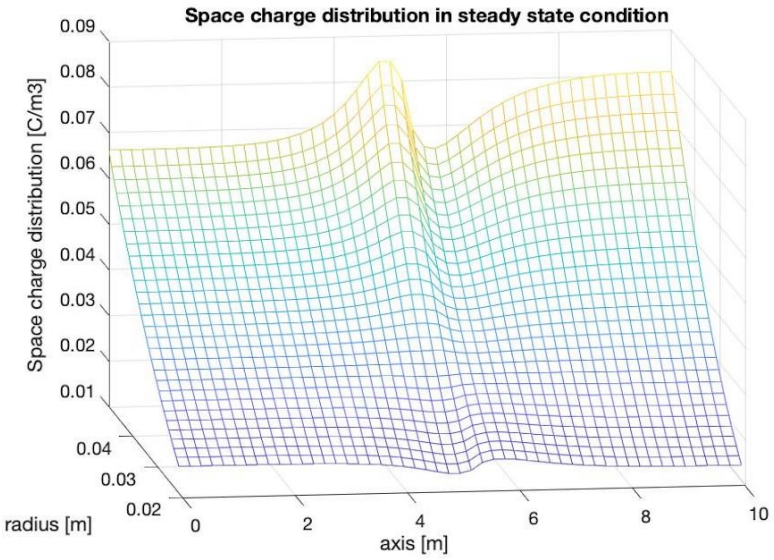


***Figure 1.13.*** *Scenario 1 - Space charge spatial distribution - t = 48 h - the figure is reproduced from [14]*

In Figures 1.14 and 1.15, the two profiles illustrate the electric field distribution over the radial and axial coordinates of the cable. The electric field depends on the applied voltage and it is influenced by the space charge accumulation. As it can be observed in the figures, as well as the space charge density, the maximum values of the electric field are reached just below the average interface level.

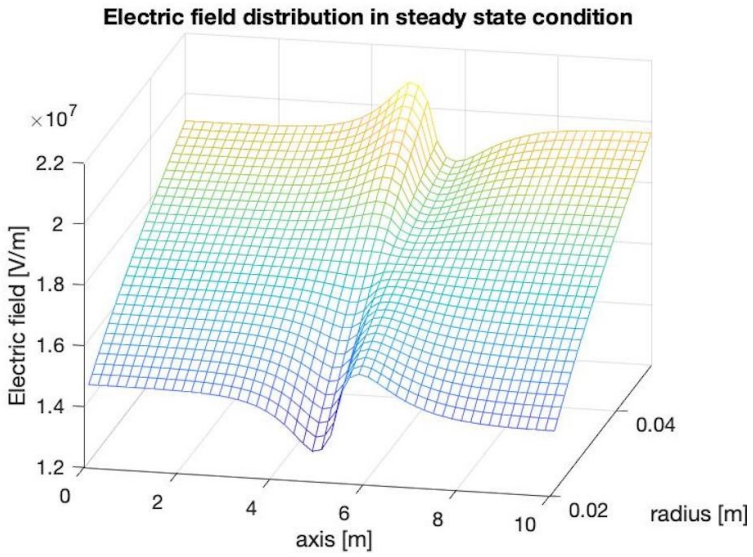


***Figure 1.14.*** *Scenario 1 - Electric field spatial distribution - t = 24 h - the figure is reproduced from [14]*

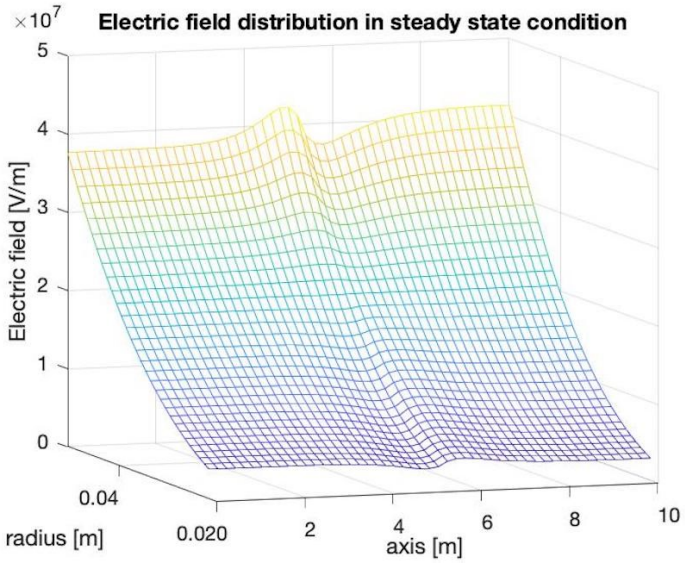


***Figure 1.15.*** *Scenario 1 - Electric field spatial distribution - t = 48 h - the figure is reproduced from [14]*

### 1.1.2 Scenario 2 – Polarity Reversal event

In the second scenario described in this thesis, after applying the rated voltage with a step function, a current of 1152 A flowing through the conductor is set. This current is equal to 60% of the rated ampacity. After 24 h from the beginning of the transient, a Polarity Reversal event begins. This consists of grounding the cable, then a period of 180 s with the voltage maintained equal to 0 and then applying the negative voltage to the conductor.

The purpose of this study is to evaluate the peak of electric field expected in proximity of the conductor after a programmed PR event starting from normal load conditions. In particular, attention is focused on the evaluation of the contribution in this phenomenon of the variation along the axis of the heat exchange conditions between the surface of the cable and the outside. In Figure 1.16, the temperature drop over the insulation thickness just before the PR event is shown, as a function of the axial coordinate. As it can be observed, as found for the Scenario 1, the maximum temperature drop is reached in the cold segment just below the average level of the interface. In this scenario, the entity of the radial thermal gradient reaches about a +16.8% with respect to the value in deep waters and +9.5% with respect to the value immersed in air. In Figure 1.17, the temperature distribution over the axis and radial coordinates, just before the PR event, is shown.

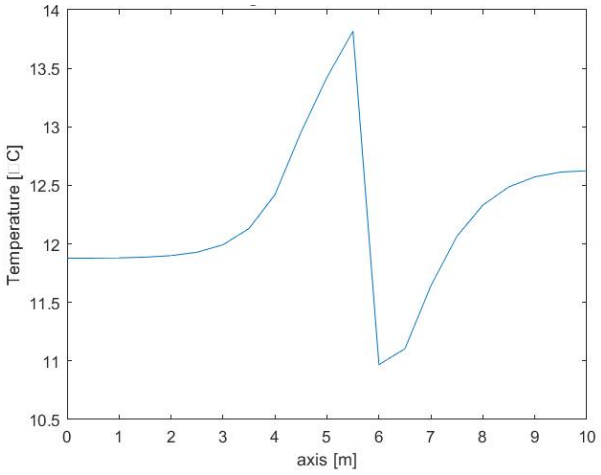


***Figure 1.16.*** *Scenario 2 - Temperature drop vs axial coordinate at the end of the first half of the transient t = 24 h, I = 1152 A*

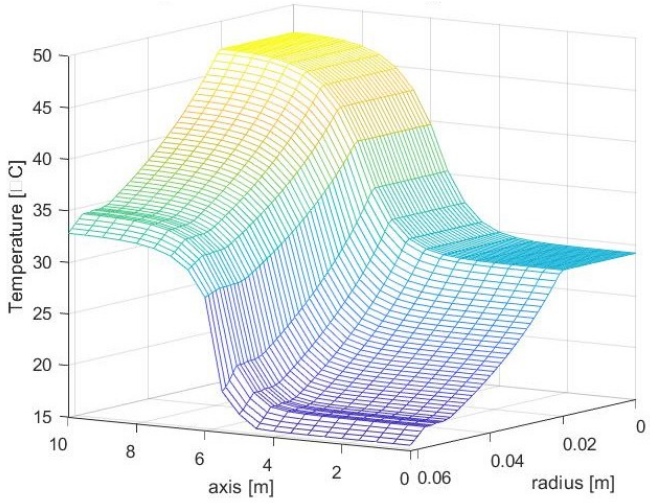


***Figure 1.17.*** *Scenario 2 - Temperature spatial distribution at the end of the first half of the transient t = 24 h, I = 1152 A*

As it can be observed from the figure 1.18, a thermal equilibrium can be considered as achieved after the first half of the transient. The decision to start the PR after 24 h from the start of the simulated transient is due to this circumstance.

Figure 1.19 shows the time course of the radial distribution of space charge immediately below the interface between the two external media. After reaching an equilibrium distribution after about 12 h, the space charge takes about 4 h, starting from the PR event, to reach a new equilibrium distribution identical but with opposite sign to the previous one. As can be seen from the Figure 1.19, immediately after the polarity inversion, the space charge density near the conductor reaches a negative peak. Subsequently, the charge accumulated near the conductor migrates outwards and a new equilibrium distribution is reached. The duration of this phenomenon is greater at lower temperatures due to the lesser mobility, under these conditions, of the charge carriers.

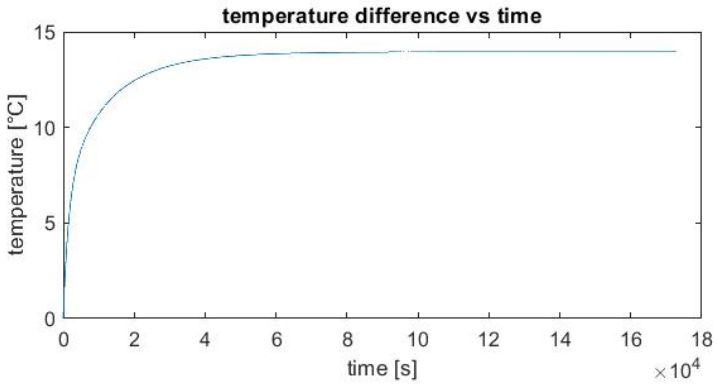


***Figure 1.18.*** *Scenario 2 – Time trend of the temperature drop over the insulation thickness, I = 1152 A*

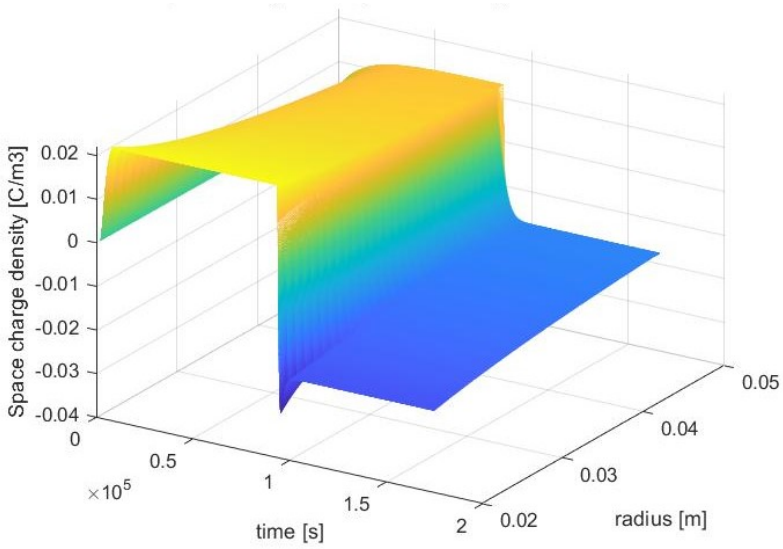


***Figure 1.19.*** *Scenario 2 - Radial space charge distribution at the average interface level vs time*

In Figure 1.20, the time trend of the electric field radial distribution, referred to the section just below the water-air interface is shown. As it is possible to observe, the times in which the electric field varies can be traced back to the time constants of variation of the space charge. As found for the space charge, the electric field also reaches a local peak near the interface between the internal semiconductor and the dielectric immediately after the voltage polarity reversal. Figure 1.21 shows the time trend of the maximum value of the electric field module in the section just below the average interface level between the external means. The electric field peak reached, due to polarity inversion, is 85% higher than the maximum reached in stationary conditions. In this portion of the cable, immediately after the PR event, the electric field modulus reaches the peak value of 38.2 kV/mm. In order to evaluate the role of axial thermal conduction in this phenomenon, Figure 1.22 shows the radial electric field distributions before the PR and at the end of the PR ramp in a section in the "hot region" 5 m away from the interface between the two external media. As can be seen, the peak value of the electric field modulus achieved in this region is equal to 32.1 kV/mm. Therefore, it can be concluded that the peak of electric field at the interface results 19 % higher than that found far from it. As can be seen, the increase due to the axial transmission of heat in terms of electric field (+ 19%) is more than double compared to the increase in temperature difference (+ 9.5%). This is explained by the fact that not only is the temperature difference at the interface greater than that in the hot region, but at the same time, the average temperature in the interface area is lower. This implies a longer time constant for the resetting of the charges because $\varepsilon_0\varepsilon_r/\sigma$ is lower as the temperature decreases.

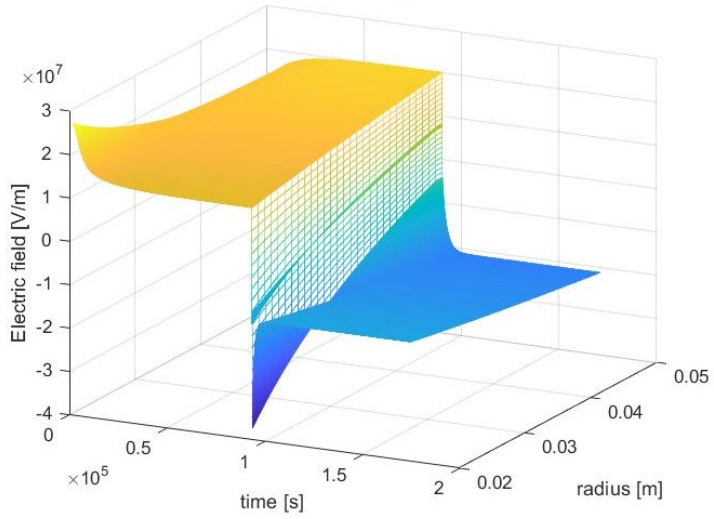


***Figure 1.20.*** *Scenario 2 - Radial electric field distribution at the average interface level vs time*

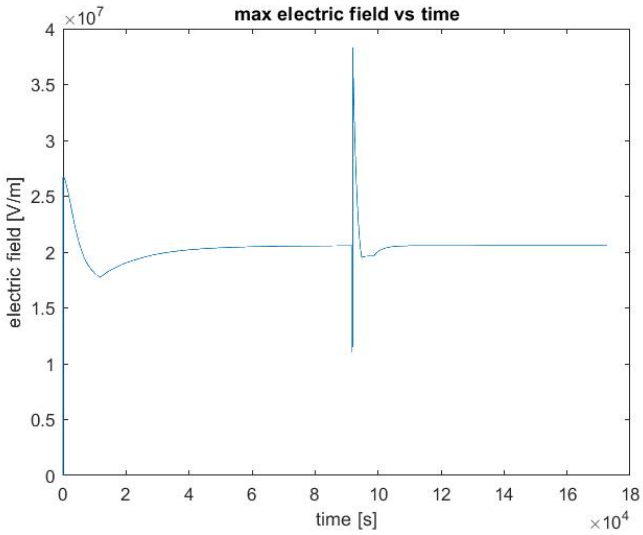


***Figure 1.21.*** *Scenario 2 – Time trend of the maximum electric field magnitude at the average interface level vs time*

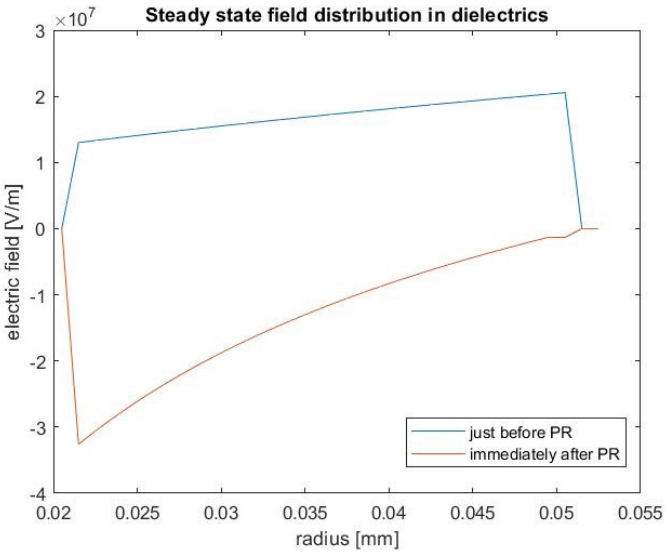


***Figure 1.22.*** *Scenario 2 – Radial electric field distributions before the PR and at the end of the PR ramp (section in the "hot region", at a distance of 5 m from the interface)*

Finally, it should be considered that the achievement of electric field values close to the breakdown for aged dielectrics makes the consideration of the axial heat transmission a factor not to be neglected.

### 1.1.3 Discussion

As mentioned above, this study is focused on the evaluation of the electric field peak reachable near the interface between two mediums in which an HVDC cable could be immersed. As described above, this value depends on the geometry of the cable, the

properties of the materials of which it is composed and the external mediums' properties. In order to describe this phenomenon from a more general point of view, for a certain cable, the ratio between the axial and the radial thermal resistances can be considered. The thermal conductivities of copper and aluminum used for the core are typically three orders of magnitude higher than those of the insulating material. In the case of a cable having a copper core and XLPE insulation, the thermal conductivities are 390 W/(m*K) and 0.287 W/(m*K) respectively. Therefore, the axial thermal resistance can be approximated as which of the conductor $R_A$ that can be calculated as follows [14]:

$$R_A = \frac{4l}{k_{cond} d_{cond}^2 \pi f} \tag{1.18}$$

Where $l$ is the length of the cable section, $k_{cond}$ is the thermal conductivity of the conductor material, $d_{cond}$ is the diameter of the conductor and $f$ is its filling factor.

The radial thermal resistance $R_R$ of the dielectric can be estimated as follows [14]:

$$R_R = \frac{\ln\left(\frac{d_{ext}}{d_{cond}}\right)}{2\pi l k_{diel}} \tag{1.19}$$

Where $d_{ext}$ is the outer diameter of the dielectric and $k_{diel}$ is its thermal conductivity. By setting ($R_A = R_R$), it is possible to find a value of $l$ such that the axial thermal resistance is equal to the radial one [14]:

$$l_{eq} = \sqrt{\frac{m}{8} \frac{k_{cond}}{k_{diel}}} \tag{1.20}$$

Where:

$$m = \ln(y) d_{cond}^2 f \tag{1.21}$$

Where:

$$y = \frac{d_{ext}}{d_{cond}} \tag{1.22}$$

Where $l_{eq}$ is the length of a cable' segment where the axial and the radial thermal resistances are equals. The values of m and $l_{eq}$ grow up with the diameter of the conductor and with the ratio y as shown in Figures 1.23 and 1.24. The aptitude of a cable to be subjected to local electric field peaks related to axial thermal conduction could be defined by the above parameter $l_{eq}$ that only depends on the characteristics of the cable. In other words, the higher is the value of $l_{eq}$, the higher is the ratio between axial and radial thermal

resistances. Therefore, in the case of abrupt variations in the heat exchange conditions with the axial coordinate, as $l_{eq}$ grows, the peak in the temperature drop over the insulation thickness increases.

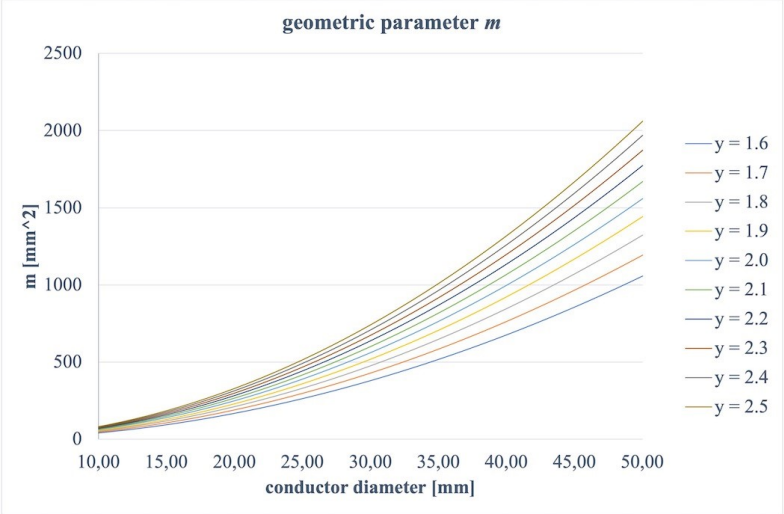


***Figure 1.23.*** *Geometric factor m vs conductor diam. at different values of ratio y and f = 0.9 - the figure is reproduced from [14]*

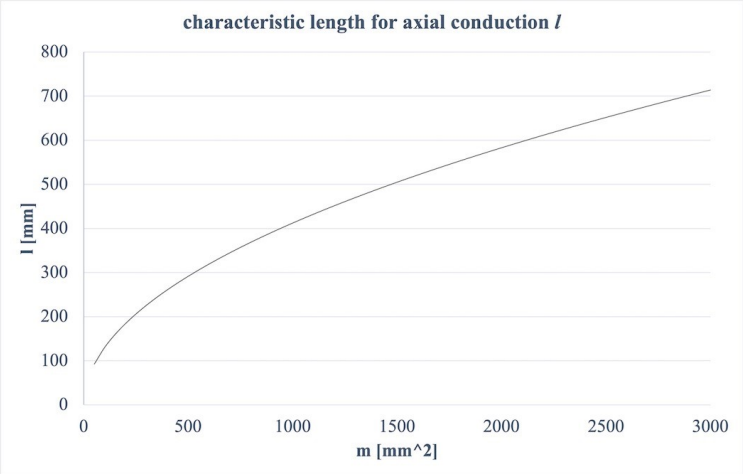


***Figure 1.24.*** *Characteristic length for the axial conduction l vs geometric parameter m - the figure is reproduced from [14]*

The results of this research show the effect, on the distributions of space charge and electric field inside the insulating layer of an HVDC cable, of the axial variation of the heat transfer conditions with the outside. The analysis has been carried out by means of simulations performed considering different scenarios. Furthermore, in the case of Scenario 1, attention has been paid to the space charge and electric field trends during the transition between the two different phases. As it can be noticed from the Figure 1.7, the growth in load causes the inversion of slope of the space charge profile because of the increased

electrical conductivity of the dielectric at higher temperatures. This behavior can be explained considering the distribution of space charge density within the dielectric layer once reached the steady state. Neglecting the axial and angular derivatives of the radial component of the electric field, the Equation (1.9) can be written as follows:

$$\sigma E_r \frac{d}{dr}\left(\frac{\varepsilon}{\sigma}\right) = \rho \tag{1.23}$$

Where $\varepsilon$ is the permittivity of the insulation. In order to assess the radial slope of the space charge density, the (1.23) is derived as follows:

$$\frac{d\rho}{dr} = \frac{d}{dr}(\sigma E_r) \cdot \frac{d}{dr}\left(\frac{\varepsilon}{\sigma}\right) + \sigma E_r \frac{d^2}{dr^2}\left(\frac{\varepsilon}{\sigma}\right) \tag{1.24}$$

It is possible to demonstrate that the first term of the right-hand side part of the equation (1.24) is negative for the insulation layers subjected to HVDC voltage and under load. On the contrary, it can be proved that the second term assumes positive values due to the exponential trend of the electrical conductivity with the temperature and therefore with the radius. In the Figure 1.25, the sign of the aforementioned derived terms, at the end of the simulated transient, are shown. Since $\sigma E_r$ is proportional with the temperature, the radial derivative of the space charge density passes from negative to positive values once exceeded a certain temperature. On the basis of the aforementioned reasons, it can be stated that the space charge profile depends on both the temperature drop and its average value. The former term prevails at low loads whilst the latter dominates when the current tends to its rated value. In other words, the higher the load, the higher the space charge accumulated near the cooler interface with the outer semiconductive layer.

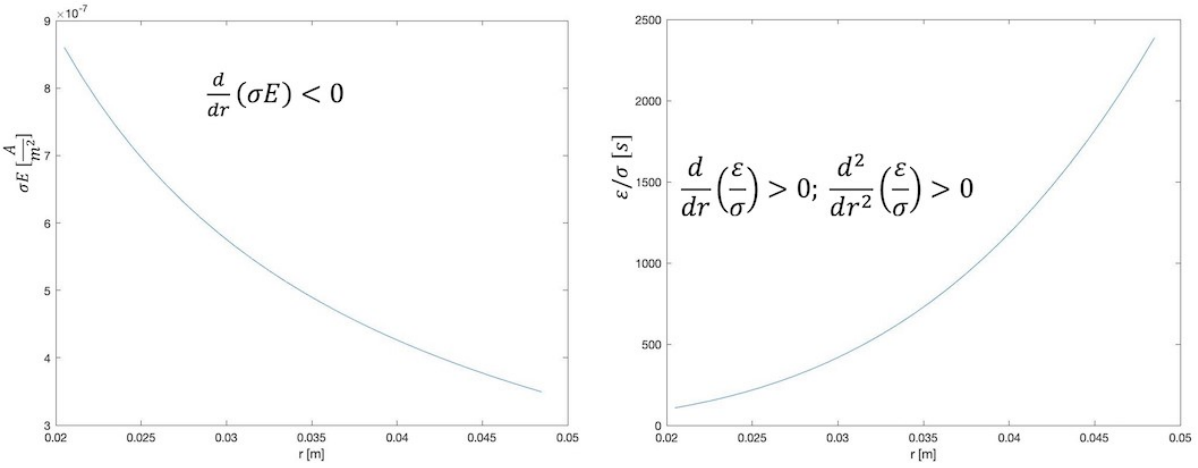


***Figure 1.25.*** *Radial trends of the terms derived in the equation (24) at the end of the simulated transient (Scenario 1) - the figure is reproduced from [14]*

## 1.2 Interaction between space charge accumulation and Partial Discharge phenomenon in HVDC joints during Transient Over-Voltages

In this study, the occurrence of Partial Discharges (PD) inception conditions in a void inside an HVDC joint during a Transient Over-Voltage (TOV) event is investigated by means of simulations performed by means of a FEM software. This type of event can be considered as one of the most severe from the point of view of the occurrence of PD as the effect of the rapid variation of applied voltage is combined with the previously established electric field distribution due to the space charge accumulation.

As described above, under relatively high temperature drops and electric stresses, the electric field distribution is strongly affected by the space charge present within the bulk of the dielectric layer. This phenomenon can play an important role in the establishment of inception conditions for PD. As demonstrated by several researchers, under HVDC stress, the PD Inception Voltage (PDIV) is proportional to the ratio between the air and the dielectric conductivities. In many cases, this leads to an increase in the PDIV and, therefore, to a reduced PD activity under HVDC than under equivalent HVAC conditions. However, several transient external conditions occur during the operating of HVDC cables and accessories, such as the energization, the grounding, the Reversal Polarity (RP) and the Transient Over Voltages (TOV). In these conditions, the polarization current through the dielectric is added to the conduction current enhancing the PD activity.

In HVDC joints, the PD activity can be enhanced by a complex three-dimensional geometry with more interfaces than in a cable and an increased insulation thickness increasing the temperature drop [27-30]. Furthermore, the encasing an air void during the manufacturing process is more likely in a joint than in a cable. For this reason, an IEEE standard on the defect detection in HVDC pre-molded joints by means of the PD measurement under an HVAC test stress has been recently published [31].

This study attempts to provide a contribution in the knowledge of the PD phenomenon in an air void defect inside an HVDC pre-molded joint during a TOV event. The investigation has been carried out through a coupled thermal and electric model implemented in a FEM software. The current continuity equation and the Maxwell quasi-static model have been coupled with a heat conduction model and they have been applied to a three-dimensional geometry modeling a typical pre-molded joint. In addition, the

Schottky injection has been applied as boundary condition at the interfaces between the semiconductive and the dielectric layers. The simulation model has been applied to a typical pre-molded HVDC joint like the one shown in Figure 1.26. In Figure 1.27, the position of the considered air void defect is shown.

The case study is consistent with a cable-joint system designed to operate under a rated voltage of 525 kV. By considering a maximum environmental temperature of 35 °C and a maximum conductor temperature of 90 °C, the ampacity of the cable-joint system is equal to 1600 A. The calculation domain for the heat transfer analysis is composed of the joint and a cable portion 400 mm long directly buried in a surrounding material. The calculation domain for the dielectric phenomena is limited to the dielectric layers of the cable and joint. In order to minimize the computational effort, the geometrical model is axially limited by the symmetry plane dividing the joint into two parts. Similarly, a plane transverse to the axis limits the cable portion. The main geometrical parameters of the case study have been listed in Table 1.4. A three-dimensional geometric model of the considered joint has been built in FEM software and it has been meshed with 416.872 tetrahedral elements as shown in Figure 1.28. The spherical air cavity has been geometrically defined by 12 elements whilst the surrounding medium has been divided into 512.453 elements. The materials considered in this case study are reported in Table 1.5. Thermal conductivity of 0.2857 W/(mK) and 0.2 W/(mK) have been considered for XLPE and Silicone Rubber (SR) respectively [25].

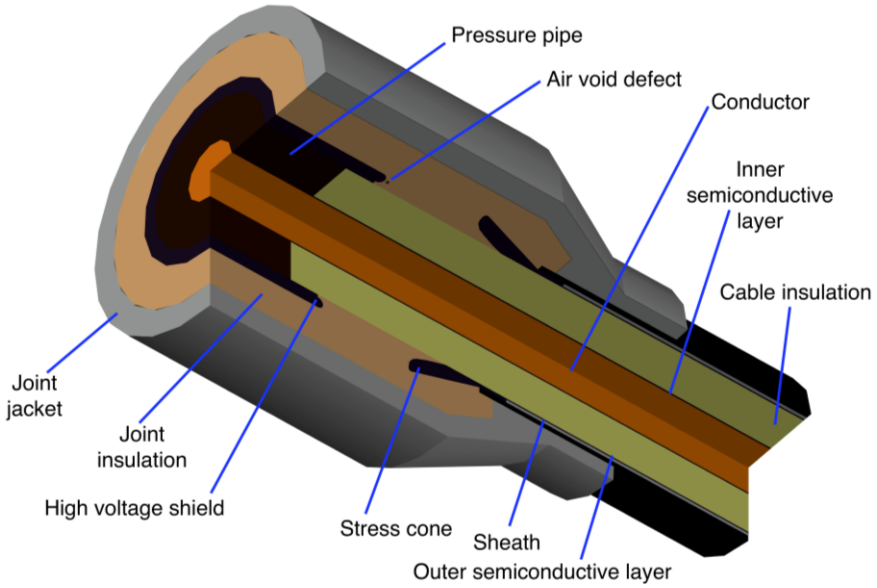


***Figure 1.26.*** *Characteristics of the case-study joint (drawing not to scale) - the figure is reproduced from [13]*

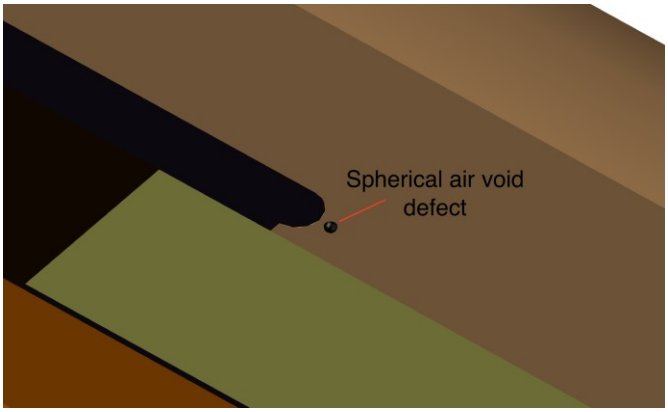


***Figure 1.27.*** *Position of the defect - the figure is reproduced from [13]*

A thermal power generation term due to the Joule effect is applied to the conductor whilst dielectric losses are considered for the insulation layers. The Joule losses inside the conductor are calculated considering a current of 1600 A and the temperature dependent conductivity of the copper stranded core. The dielectric losses are calculated and updated by means of the aforementioned transient electrical conductivity model. The temperature at the cylindrical boundaries of the surrounding material is set equal to 20 °C whilst adiabatic conditions have been considered for the aforementioned limiting transverse planes.

***TABLE 1.4.*** *Main geometrical properties*

| **Parameters** | **Dimensions** |
|---|---|
| **Radius of the cable conductor [mm]** | 20 |
| **Conductor section area [mm2]** | 1000 |
| **Cable insulation thickness [mm]** | 30 |
| **Outer radius of the cable [mm]** | 58 |
| **Thickness of the high voltage shield [mm]** | 5 |
| **Axial length of the stress cone [mm]** | 105 |
| **Distance between the stress cone and the high voltage screen along the cable insulation outer surface [mm]** | 190 |
| **Joint insulation thickness [mm]** | 28 |
| **Outer radius of the joint [mm]** | 89 |
| **Axial lenth of the joint (up to the jacket edge) [mm]** | 840 |
| **Axial length of the cable portion [mm]** | 400 |
| **Diameter of the air void defect [mm]** | 1.4 |
| **Parameters** | Dimensions |

***TABLE 1.5.*** *Materials considered for the case study*

| Layers | Materials |
|---|---|
| **Stranded conductor** | Copper |
| **Cable insulation** | XLPE |
| **Joint insulation** | Silicon Rubber |
| **Cable jacket** | PE |
| **Cable semiconductive layers** | XLPE based semiconductive compounds |
| **Joint jacket** | Aluminum |
| **Pressure pipe** | PE based semiconductive compound |
| **High voltage shield and stress cone** | XLPE based semiconductive compound |
| **Surrounding material** | Soil |

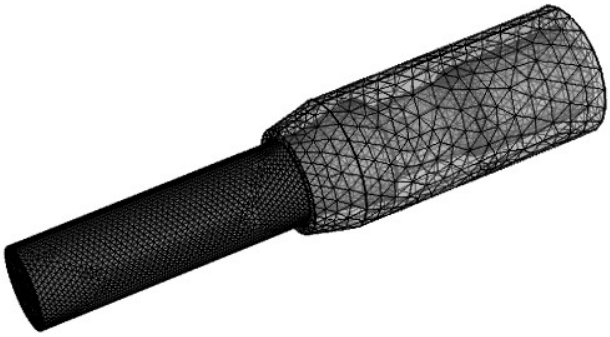

***Figure 1.28.*** *Case-study joint meshed - the figure is reproduced from [13]*

As can be noticed, the rated current is considered whilst the environmental temperature is lower than the maximum value considered in the ampacity calculation. This choice aims to investigate the effect on the electric field distribution of the achievement of the maximum temperature drop across the insulation layer when the conductor temperature is lower than the maximum rated value. In these conditions, the reduced electrical conductivity of the insulation layers can lead to higher peaks in the electric field during fast voltage transients, such as the TOV event investigated in this study. The boundary conditions for the heat transfer analysis are kept constant throughout the duration of the simulated transient.

The conductivity model for the analysis of the space charge phenomena occurring in dielectrics under HVDC voltage is based on Equation (1.4). In addition, as mentioned

above, the heat generation inside the insulation layers depends on the dielectric losses that vary with the temperature. This makes this coupled thermal and electrical model strongly non-linear, therefore, a pre-conditioning phase is needed to converge towards the steady state conditions. Firstly, a stationary analysis is performed with half the rated voltage and the rated current flowing through the conductor. Then, the rated voltage of 525 kV is reached through a ramp with a duration of 600 s. Finally, a further stationary phase is carried out in order to reach stable and stationary conditions before to simulate the TOV event. A positive voltage of 525 kV is applied to the interfaces between the dielectrics and the inner semiconductive layers whilst the outer surfaces of the dielectrics are grounded. Like the thermal model, an electrical insulation condition is applied to the limiting transverse planes.

Once reached the steady state conditions, the voltage follows the trend of a typical long TOV shown in Figure 1.29. After 5 ms from the beginning of the TOV event, the voltage is increased by 0.8 times the rated value and, after a further 5 ms, it decreases to 1.6 times the initial value and is held constant for a further 90 ms. A Schottky charge injection at the interfaces between the dielectric and semiconductive layers has been applied as a radial current generation at the radial boundaries of the calculation domain for the electrical model. As mentioned above, the electrical conductivities of XLPE and SR are obtained by means of Equation (1.4). The relative parameters $A$, $\varphi$ and $B$ are reported in the Table 1.6.

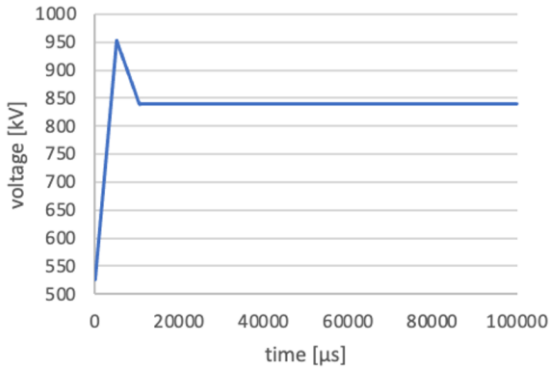


***Figure 1.29.*** *Transient Over Voltage (TOV) - the figure is reproduced from [13]*

***TABLE 1.6.*** *Materials considered for the case study*

| **Materials** | **A [V/(Ω*m²]** | **Φ [eV]** | **B[m/V]** |
|---|---|---|---|
| **XLPE** | $8.15*10^{6}$ | 0.78 | $1.40*10^{-7}$ |
| **SR** | $1.93*10^{6}$ | 0.72 | $5.43*10^{-8}$ |

Before the beginning of a PD, the electrical conductivity of the air inside the cavity, σa, is calculated through the following function of the local electric field modulus *E [13]*:

$$\sigma_a = \begin{cases} 3E - 16\ S/m, E < E_{inc} \\ 1E - 4\ S/m, E \geq E_{inc} \end{cases} \quad (1.25)$$

where $E_{inc}$ is the "Equivalent" Partial Discharge Inception Electric Field (EPDIEF) that has been experimentally obtained as described in the Chapter 4 in a similar cavity under HVDC stress and it has been found to be equal to 18 kV/mm. This value is not the actual ignition electric field for partial discharges but is obtained experimentally and compared with a conductivity model in order to obtain a threshold value to predict the occurrence of PD with repeatability.

Once begun the PD, the conductivity of air is set as follows [13]:

$$\sigma_a = \begin{cases} 3E - 16\ S/m, E < E_{est} \\ 1E - 4\ S/m, E \geq E_{est} \end{cases} \quad (1.26)$$

Where $E_{est}$ is the extinction electric field set equal to 1 kV/mm.

In Figure 1.30, the temperature distribution is illustrated by means of a color map. The maximum temperature reached inside the conductor is equal to 75.1 °C, therefore, the temperature difference between the core and the environmental is equal to that achieved under rated conditions (conductor and environmental temperature equal to 90 °C and 35 °C respectively). The maximum temperature drop across the joint insulation is equal to 34.3 °C in the portion between the stress cone and the pressure pipe whilst the temperature difference between the conductor and the outer surface of the cable insulation reaches 21.2 °C. Due to the thermal inertia of the system, the temperature distribution does not change appreciably during the TOV event. The temperature of the conductor in the middle of the joint is 0.6 °C higher than that at the axial boundary of the cable portion. Thus, in the conditions chosen for this case study, the joint can be considered as a hot spot of the cable line.

In Figure 1.31, the electric field distribution at the end of the steady state phase is shown. The maximum value of 37.8 kV/mm is reached in proximity of the interface between the two different dielectrics and the stress cone. In the cable portion, the maximum electric field of 21.7 kV/mm is achieved in proximity of the outer surface of the insulation layer whilst the minimum value of 14.9 kV/mm is reached near the inner surface. Similarly, in

proximity of the axial middle of the joint, the maximum electric field of 23.8 kV/mm is reached in proximity of the outer surface of the SR layer.

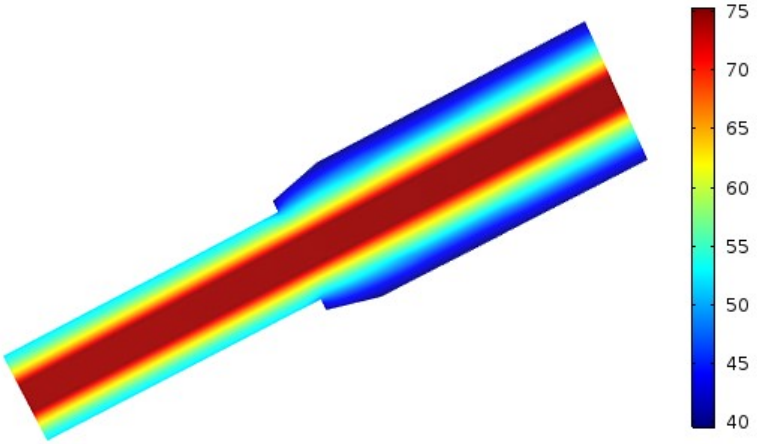


***Figure 1.30.*** *Temperature distribution at the end of the steady state phase (units in degC) - the figure is reproduced from [13]*

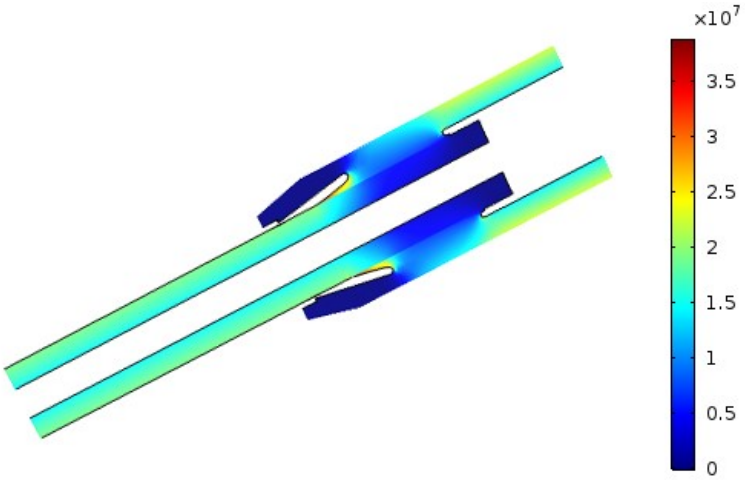


***Figure 1.31.*** *Electric field distribution at the end of the steady state phase (units in V/m) - the figure is reproduced from [13]*

In Figure 1.32, the electric field distribution near the air void defect at the end of the steady state phase, is shown. Under these conditions, the maximum electric field magnitude inside the cavity is 13.2 kV/mm. This value is 1.6 times higher than that in the same position in absence of the defect.

As mentioned above, the TOV shown in Figure 1.29 has been applied to the high voltage boundaries of the calculation domain for the electric model of the case study. The average electric field magnitude inside the cavity reaches the inception value of 18 kV/mm after 1.4 ms from the beginning of the initial voltage ramp as shown in Figure 1.33. As also found by other researchers, in the area between the stress cone and the pressure pipe, the axial

component of the electric field has the same order of magnitude of the radial one because the proximity to the grounded stress cone.

The space charge distribution before the inception of the first PD is shown in Figure 1.34. As can be observed, the space charge distribution is consistent with the direction of the electric field and reaches values of +/- 0.2 C/m$^3$ in proximity of the cavity' surface.

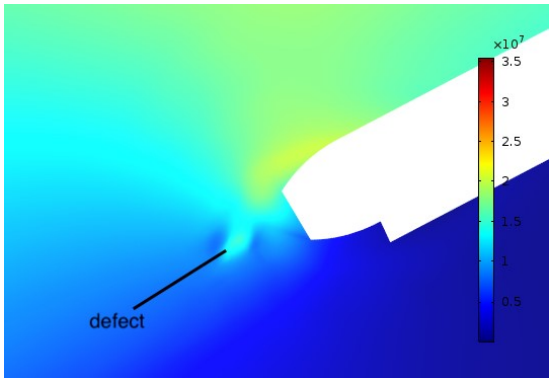


***Figure 1.32.*** *Electric field distribution at the end of the steady state phase in proximity of the air void defect (units in V/m) - the figure is reproduced from [13]*

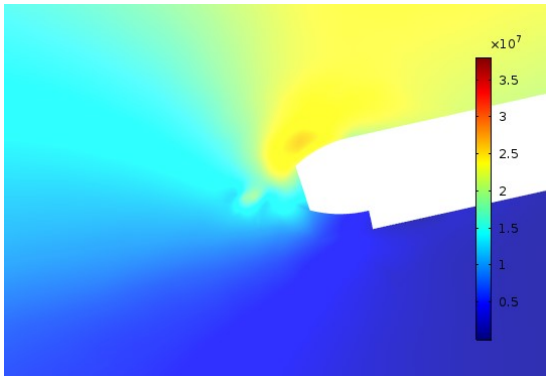


***Figure 1.33.*** *Electric field distribution before the inception of the first PD, after 1.4 ms from the beginning of the TOV (units in V/m) - the figure is reproduced from [13]*

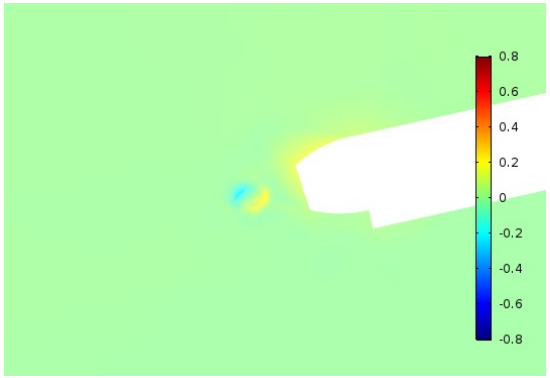


***Figure 1.34.*** *Space charge distribution before the inception of the first PD, after 1.4 ms from the beginning of the TOV (units in C/m$^3$)*

The electric field distribution at the end of the first PD is shown in Figure 1.35. As can be observed, at the end of the PD, the electric field has reached the extinction value of 1 kV/mm within the cavity whilst it is increased in proximity of the defect.

As can be seen in Figure 1.36, the space charge distribution at the end of the first PD is in opposition to the direction of the electric field and it reaches the maximum magnitude of +/- 0.6 C/m$^3$ in proximity of the cavity' surface, outside of it. The space charge distribution established after the first partial discharge opposes the sudden rise of the electric field inside the cavity and, therefore, inhibits the occurrence of new partial discharges.

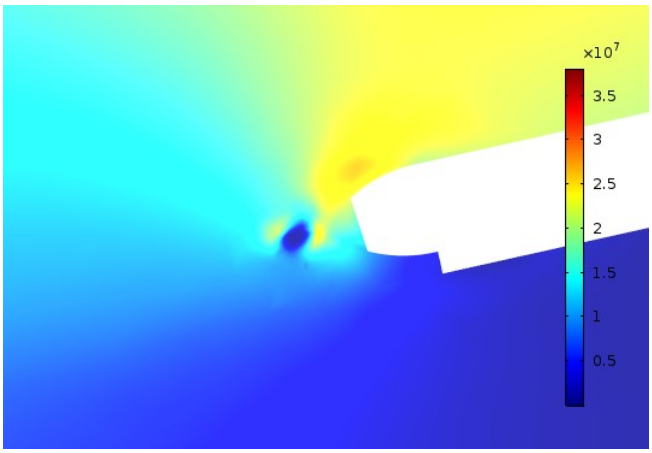


***Figure 1.35.*** *Electric field distribution at the end of the first PD (units in V/m) - the figure is reproduced from [13]*

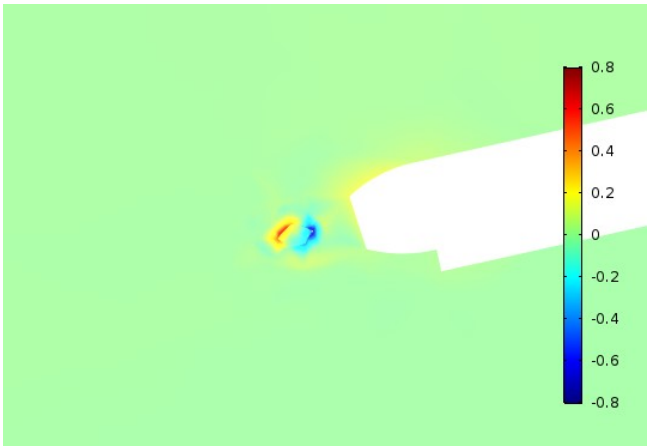


***Figure 1.36.*** *Space charge distribution at the end of the first PD (units in C/m$^3$) - the figure is reproduced from [13]*

As can be observed in the Figure 1.37, the electric field inside the cavity overcomes the inception value for PDs only one time during the TOV event. As can be observed in the Figure 1.38, the unique PD resulting from the simulation is associated to a high discharge

current and duration compared to those occurring under AC stress. By integrating the curve shown in Figure 1.38 over time, it has been obtained a total charge released from the observed PD equal to 2386 pC.

In Figures 1.39 and 1.40, the electric field distribution at the end of the rising voltage ramp of the TOV is shown. As can be observed, the maximum electric field magnitude equal to 43,4 kV/mm is reached in proximity of the high voltage shield of the joint. High magnitudes of the electric field just lower than the maximum value are reached near the cable conductor and between the stress cone and the interface between the cable and the joint insulation. In proximity of the joint axial middle, the highest value of the electric field is held near the outer surface. This can be attributed to the lower electrical conductivity of the insulation in this colder area that leads to a longer time necessary for the displacement of the residual space charge.

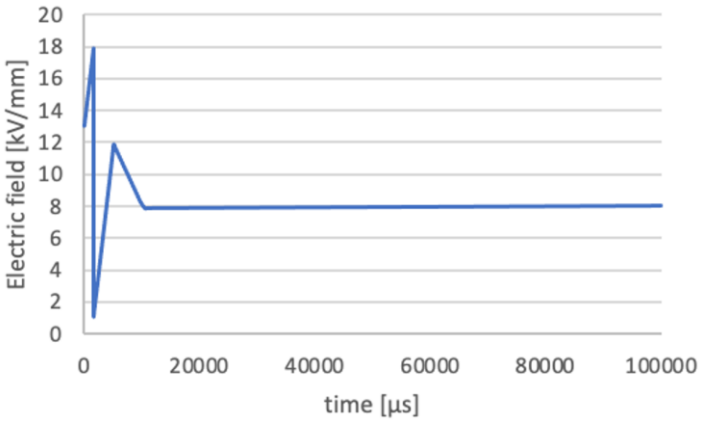


***Figure 1.37.*** *Average electric field inside the cavity during the TOV event - the figure is reproduced from [13]*

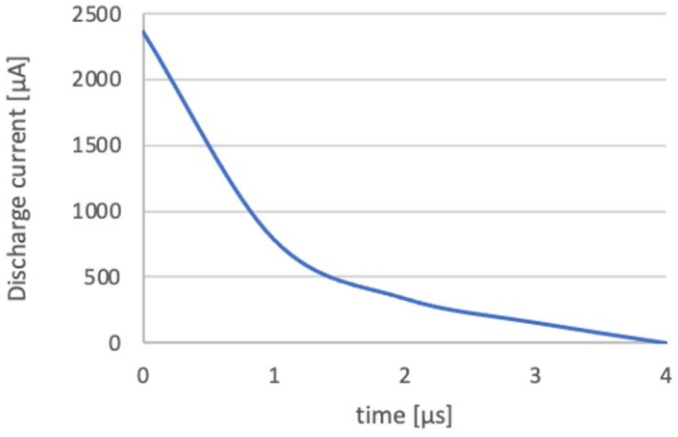


***Figure 1.38.*** *First PD – Discharge current - the figure is reproduced from [13]*

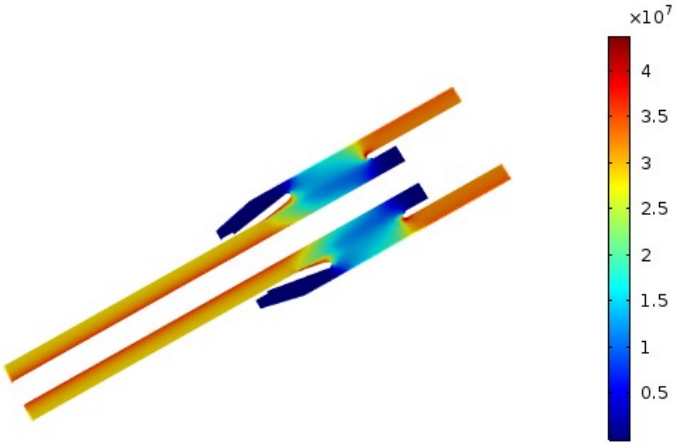


***Figure 1.39.*** *Electric field distribution at the end of the rising voltage ramp of the TOV (units in V/m) - the figure is reproduced from [13]*

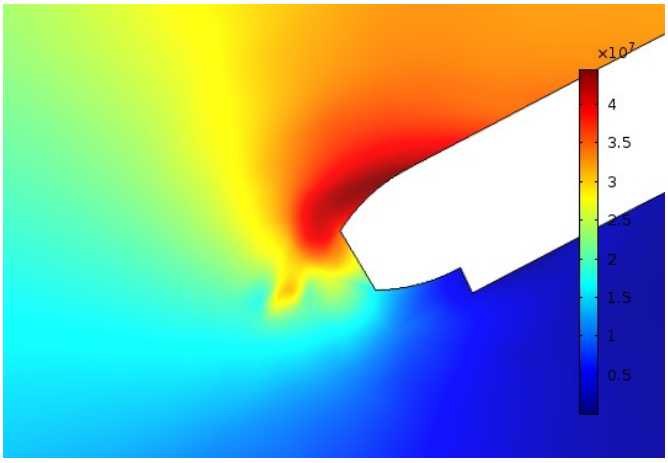


***Figure 1.40.*** *Electric field distribution at the end of the rising voltage ramp of the TOV (units in V/m) – detail*

## 1.3 Conclusions

In this chapter a conductivity model in dielectrics has been described, useful for the study of space charge accumulation and partial discharge phenomena in insulating materials subjected to HVDC stress. Although these phenomena can potentially be described with greater accuracy with models based on bipolar charge transport, it was chosen to implement models based on conductivity for several reasons. First of all, the computational effort for solving the equations that make up a conductivity model is less than that required to run a bipolar charge transport model. This allows the development of

complex geometries and the study of transients of relatively long duration. secondly, the conductivity models can be calibrated by means of a reduced number of parameters that characterize the materials. Thanks to this characteristic, it is possible to approach a method that leads to the experimental calibration of the models by comparison with experimental results obtained on cables or joints. Examples of this type of calibration will be described in Chapter 4.

The models described in this chapter have been implemented both on commercial FEM software and by means of discretization of the governing equations of phenomena carried out using the finite difference method. In the second case, the systems of linear equations deriving from this discretization have been compiled and solved in the Matlab® environment.

In this chapter, two case studies have been described in detail. The first of these case studies consists in the evaluation of the axial heat transmission effect on the radial temperature gradient in the dielectric of a cable partially immersed in water and partially in air. From the quasi-static Maxwell model and from the current continuity equation, it can be deduced that, in a loaded HVDC cable, space charge accumulates in the bulk of the dielectric due to the establishment of a radial gradient of electrical conductivity. For this reason, attention has been focused on phenomena that can lead to local peaks of temperature drop over the dielectric thickness. Indeed, from the simulations, it was found that, in the case of HVDC cables partly immersed in air and partly in water, it is possible to reach local electric field peaks near the interface between the two means. In stationary conditions, this phenomenon can lead to a local electric field peak that is a few percentage points higher than in the surrounding areas. On the other hand, in the case of dynamic events such as voltage polarity reversal, this phenomenon can lead to peaks that considerably exceed, even by 20%, the maximum values obtainable without considering this phenomenon. This study attempts to offer a contribute to generally define the aptitude of a cable to be subjected to local peaks in electric stress due to the axial thermal conduction. With this purpose, a parameter depending only on the cable's geometry and materials has been defined. Other research in this direction can be carried out for the evaluation of the electric field distribution near joints, hot points along the cable length or proximity with other cables. Finally, starting from the conductivity model described in one-dimensional form in the radial coordinate only, the existence of a load current threshold beyond which reverses the

slope of the radial space charge distribution has been demonstrated. This threshold depends on the characteristics of the cable and on the heat transfer conditions with the outside.

In the second section of this chapter, the phenomenon of onset of partial discharges in an HVDC joint during a Transient Over-Voltage event is analyzed. In the case study, a typical pre-molded joint has been modeled through a three-dimensional geometry. A 100 ms long TOV with a peak value of 1.8 times the rated voltage has been considered to occur after a steady state under rated current load. The findings of the analysis show the occurrence of only one PD with a released charge of 2386 pC. The energy associated to the observed PD is much higher the typical PDs observed under analogous AC stress. This could lead to the premature ageing of the joint insulation if a big amount of TOV events occur during the operating time.

# Chapter 2
# Space charge measurements – the Pulsed Electro-Acoustic method

This chapter describes the state-of-the-art of space charge measurements on dielectric flat specimens and on cables and model cables. In particular, the attention is focused on the method called Pulsed Electro-Acoustic which will be described in detail. The content of this chapter is based on the works of the author et al. entitled "*Review of the PEA Method for Space Charge Measurements on HVDC Cables and Mini-Cables*" [31], "*The Industrial Applicability of PEA Space Charge Measurements, for Performance Optimization of HVDC Power Cables*" [32] and "*Reliability of PEA Measurement in Presence of an Air Void Defect*" [33].

In last decades, many researchers have focused their work on the development of non-destructive methods for space charge measurements. In particular, the techniques were divided into three main groups in relation to the physical principle on which they are based, such as acoustic, thermal and optical methods. Of these groups, methods based on acoustic and the thermal phenomena have been largely used also in industrial applications. On the contrary, the methods based on optical phenomena haven not had much success due to the complexity of the measuring cell. For the purposes of this thesis, a description will be given for the Thermal Step Method (TSM) and, in particular, for the Pulsed Electro Acoustic (PEA) technique. These two techniques have had the greater success for measures of space charge on flat specimens but also on cables.

## 2.1 The Thermal Step Method

The thermal step method has been conceived in 1988 by Toureille [34] and its principle of operation is based on the application of a thermal step to the ends of the related sample in order to measure the current response due to the thermal expansion of the sample itself. More in detail, a thermal diffuser provides a heat step, which creates a thermal wave. This wave will diffuse through the thickness of the dielectric, which determines either an expansion or a contraction of the material, a variation of the insulation permittivity and causing a temporary and reversible displacement of the space charge located within the sample. This displacement will be, then, reflected on the electrodes, determining a variation

of the induced charge and, consequently, a current between the electrodes. The value of this current *I(t)* read by a pico-ammeter (pA) is related to the distribution of both the electric field and the space charge over the axis x of the capacitor shown in Figure 2.1 [35]. This setup is called TSM in short-circuit condition.

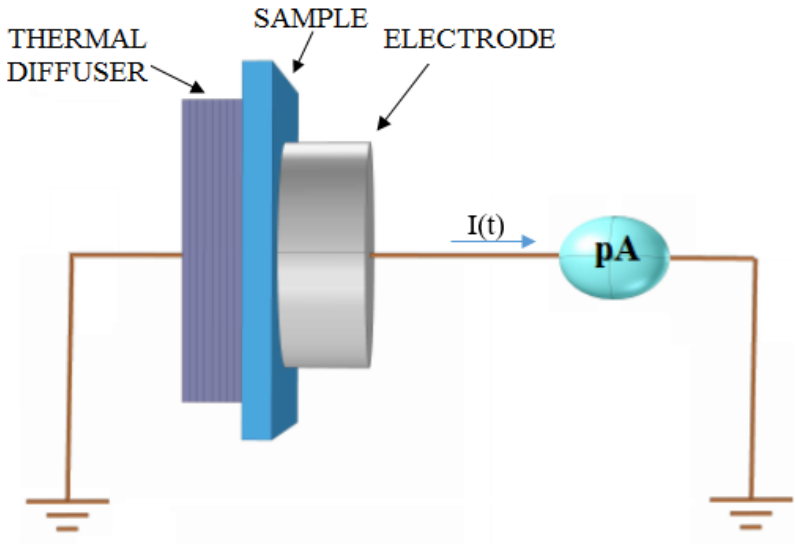


***Figure 2.1.*** *Working principle of the TSM in short-circuit condition.*

The expression of *I(t)* is reported in the following equation:

$$I(t) = -\alpha C \int_0^d E_x(x) \frac{\partial \Delta T(x,t)}{\partial t} dx \tag{2.1}$$

where $\alpha = \alpha_x - \alpha_\varepsilon$ (in which $\alpha_x$ is the coefficient of thermal expansion and $\alpha_\varepsilon$ is the temperature coefficient of the insulating material). The term *C* is the capacitance of the sample before the application of the thermal step, *d* is the sample thickness, $E_x(x)$ is the component of the electric field along the direction of the current at the abscissa *x* and $\Delta T$ the temperature step. Once $E_x(x)$ and the dielectric constant of the material $\varepsilon$ are known, from Poisson's equation, the distribution of the space charge can be determined.

For this purpose, the adoption of the deconvolution technique is needed, e.g., the "Fourier series" or the "process of successive derivatives" that allows the reduction of the deconvolution calculation time or the "technique of the inverse matrix" that reduces not only the calculation time but also the related error [36].

$$\rho = \varepsilon \frac{\partial E_x(x)}{\partial x} \tag{2.2}$$

The Equation (2.2) is an approximation of Equation (1.6), where the electric field coincides with its radial component and the permittivity is assumed to be constant in space. Initially, the TSM has been applied for 2-20 mm insulation thicknesses with 150 μm of resolution. However, by means of a faster heating, thin insulations in the range of 10-100 μm with a resolution in the order of tenths of a micrometer can be investigated [37].

An important work has been also carried out by Stancu et al. [38] which analyses the space charge behavior in a low density polyethylene (LDPE) disks of 0.5 mm thickness, with and without water trees. Experimental results have shown that the presence of water trees increases the accumulation of the space charges.

The proposed method has several significant advantages with respect to other thermal techniques. This is due to the nondestructive nature of the TSM, which is achieved by choosing the value of the maximum temperature imposed by the thermal step equal to the room temperature.

A drawback of the proposed technique is related to the thermal contact between the radiator and the sample, which could cause, if imperfect, temperature fluctuations and, therefore, attenuation or delay of the current response [39].

In year 2000 Agnel et al. developed a work finalized to perform space charge measurements under the application of a DC electric field [40]. However, the scheme of Figure 2.1 was not completely suitable for the measurements under electric field, because of the use of the current amplifier. In detail, the current amplifier must not be in contact with the high voltage, and also if a setup with the current amplifier placed between the sample (submitted to high voltage) and ground is used, the conduction and the polarization currents are likely to mask the thermal step current.

To overcome this challenge, a compensation sample (with the same dimensions of the sample under test) in front of the specimen was placed, obtaining the so called “double capacitor” configuration, which is represented in Figure 2.2 [41].

In order to measure space charge distribution, the testing procedure requires two steps: first, the high voltage is applied to the middle electrode, thus the two sample constitute two identical capacitances placed in parallel with respect to the high voltage source. In this way

the same amount of charge is accumulated on both samples, while the pA is short circuited. Second, during the measurement, the high voltage generator is disconnected in order to avoid the carriage of charges through the electrodes, compromising the correct measurement. The thermal step current is then measured by exciting thermally the specimen under test, while the pA is connected to the compensation sample. In this way the two samples are in series with each other and with the pA, therefore the short-circuit condition (as in the general case of the TSM described in the previous paragraph) are fulfilled. The space charge, in this case, can be assessed in the same manner described for the classic TSM.

The expression of the thermal step current *I(t)* is given by:

$$I(t) = -\alpha C_2 \int_0^d E_x(x) \frac{\partial \Delta T(x,t)}{\partial t} dx \tag{2.3}$$

where $C_2$ is the capacitance seen by the current amplifier. In particular, during the measurement, in which the two samples are in series, the value assumed by $C_2$ is equal to $C/2$.

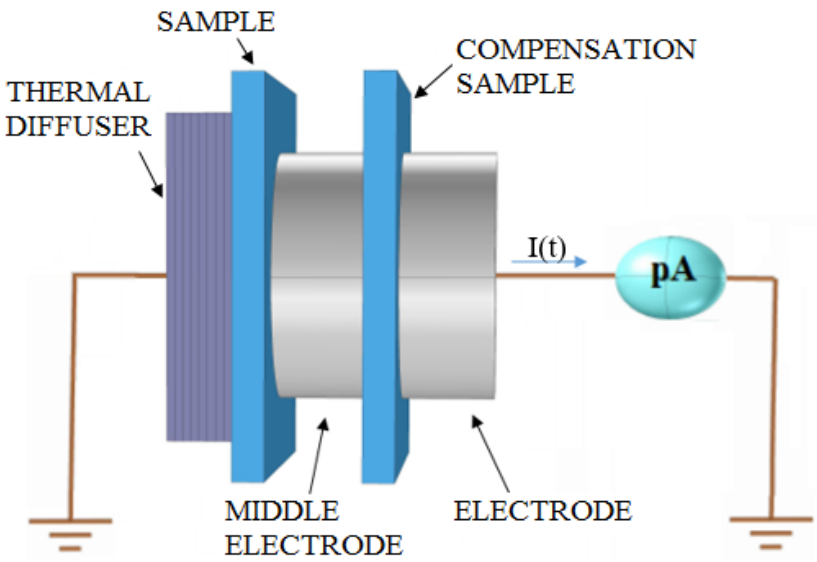


***Figure 2.2.*** *Working principle of the TSM with double capacitor.*

In 2014, Laurentie et al. proposed the "contactless" configuration in order to measure both the space charge inside the dielectric and the surface charge. In this configuration the upper face of the specimen is isolated from the upper electrode through a thin layer of air, avoiding disturbances. The diagram and explanation of the method are provided in [42].

The spatial resolution, which decreases when the distance between the space charge inside the sample and the electrode in contact with the thermal diffuser increases, is comprised between 50 and 100 µm for a polyethylene terephthalate (PET) sample of thickness of 100 µm.

In order to evaluate the influence of the electric field gradient and temperature in the charges distribution, space charge profiles were carried out in 0.5 mm of a XLPE sample, under different DC electrical stress (from 2 to 60 kV/mm) and temperatures (from 70 to 90°C). The obtained results have shown that the space charge accumulation grows with the increase of both electric field and temperature [43].

The thermal step method can also be applied to power cables by using two possible techniques:

• The Outer Cooling Technique, OCT.

• The Inner Heating Technique, IHT.

The principle of operation of both techniques does not differ from the TSM described in the preceding paragraphs. In this case the differences consist in the electrodes that are replaced by the core of cable and outer semicon, while the thermal diffuser is disposed around the cable under test. The test setup is shown in Figure 2.3, and the expression of the output signal *I(t)* is similar to that of the flat sample configuration (equation (2.1)), in which the integral one is extended to the inner and outer rays of the cable insulation, $r_0$ and $r_i$, respectively, as reported in the equation (2.4) [44, 45].

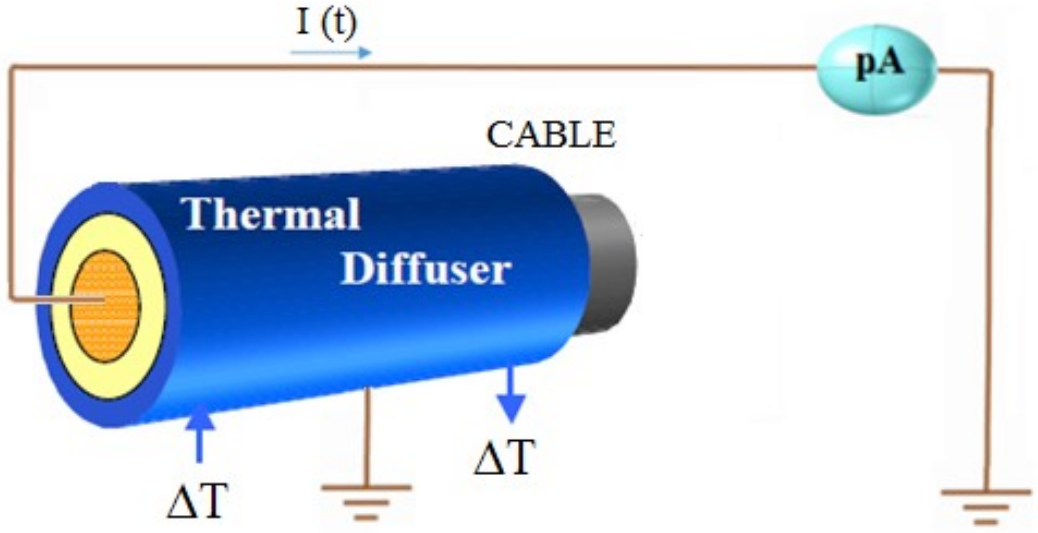


***Figure 2.3.*** *Application of the TSM to cable sample.*

$$I(t) = -\alpha C \int_{r_0}^{r_i} E_r(r) \frac{\partial \Delta T(r,t)}{\partial t} dx \tag{2.4}$$

Where $E_r(r)$ is the radial component of the electric field. In [46], a method to determine the electric field and the space charge profiles is shown. In addition, in [47], it has been demonstrated that the resolution of the method is in the order of millimeters and typically smaller than 20 mm. As well as for the flat specimens, a similar experiment was done in order to evaluate the effect of water trees on space charge accumulation in 50 cm and 70 m long cable specimens [48]. The smallest sample has been tested by using the OCT (a thermal step of −30°C), whilst the longest one was studied by means of IHT. The presence of water trees, as for flat specimens, results in a greater accumulation of charge for both samples. The described method has been also developed for onsite applications, by using power DC/DC converters for the control of high currents circulating in the inductor wrapped on the cable [49]. The TSM has been applied by Mazzanti et al. to the cables during both pre-qualification and type tests [50]. The same article reports the most relevant problems related to this method. A relevant challenge for this method can be identified by the significant space occupied by the measurement setup, which is also composed by an additional cable (namely "compensation cable"), identical to the cable under test and connected to its terminals. This is made with the aim to avoid the problems related to the current amplifier.

Another issue consists in the test procedure, because before the space charges measurement the DC source must be disconnected, while the cold liquid must begin to flow. This fact involves longer times between two subsequent measurements, when compared to other techniques, such as the Pulsed Electro Acoustic (PEA) method that is described in the next section.

## 2.2 The Pulsed Electro-Acoustic Method (PEA)

Since the eighties, PEA method has been implemented for space charge measurements on flat specimens in order to investigate space charge phenomena and to evaluate the ageing of dielectrics. In recent years, this technique has been adapted to the cylindrical geometry of cables and model cables. Experiments have been conducted using different arrangements of the measurement setup and focusing attention on different aspects of space charge

phenomena. In this section, the importance of space charge measurement is highlighted and the state-of-the-art PEA method application to flat specimen, full size cables and mini-cables is described. In addition, limits on the use of PEA method are examined and main possible directions of research are proposed in order to improve the applicability, reliability and replicability of this method.

Thanks to a relatively simple measurement system and a good spatial resolution, the PEA method is currently the most reliable way to detect space charge accumulation into the dielectric material of HVDC cables [51]. Since 1985, the year in which the group of Professor Tatsuo Takada demonstrated the possibility of measuring space charge accumulation with a non-destructive method, the scientific community has made important progress in the use of PEA method [52].

Many researchers have used PEA method to carry out space charge measurements on flat samples of dielectric materials and more recently on HVDC mini and full size cables. Many progresses have been achieved in the knowledge of performance and applicability of the PEA method. In addition, this technique has shown the occurrence of new phenomena observed for the first time in recent years and it has been used to evaluate the ageing of cables. However, further improvements to the PEA method are needed to obtain a universally accepted measurement protocol and to achieve the possibility of measuring on-site the aging of HVDC cables during their lifetime. To date, a protocol for the space charge measurements on cables has been proposed by IEEE Std 1732TM-2017 entitled “IEEE Recommended Practice for Space Charge Measurements on HighVoltage Direct-Current Extruded Cables for Rated Voltages up to 550 kV” [24]. This standard recall the contents reported in [53] and assumes that PEA method is ripe for its use for long term pre-qualification test and type test of HVDC extruded cables.

### 2.2.1 Working principles of the PEA method for flat specimen

The PEA method is physically based on the measurement of the acoustic waves generated by the vibrations of each charge laying into the dielectric material obtained through the application of a superimposed pulsed voltage between the electrodes. The effect on a sample of thickness $d$ and permittivity $\varepsilon$ of the sum of the DC applied voltage $V_{DC}$ and of the superimposed pulsed voltage $v_p(t)$ induces an electrostatic pressure $P_M$ on the charges evaluable as follows [54]:

$$P_M = \frac{1}{2}\varepsilon E(t)^2 = \frac{1}{2}\varepsilon\left[\frac{V_{DC}+v_p(t)}{d}\right]^2 \quad (2.5)$$

Once a pulsed electric field is applied across a sample with space charge in the bulk, several pressure waves may be detected at the borders of the specimen at different times on dependence by the distance between the excited charges and the measurement position. With reference to Figure 2.4, after the induced vibration of the charges laying in the thickness *dz* generate a pressure wave that is detected at the left electrode after the time *z/v*, where *v* is the sound velocity into the dielectric.

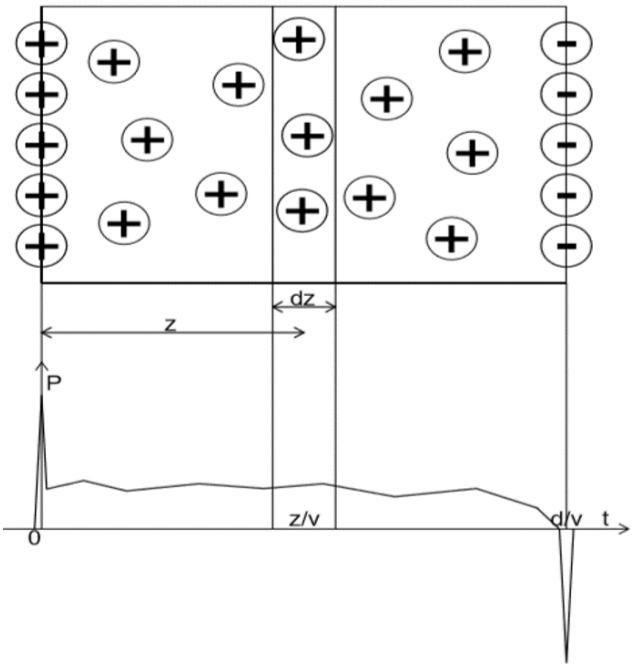


***Figure 2.4**. Pressure vs time at the first electrode interface after the application of an impulsive electric field to a flat specimen of dielectric material*

The pressure waves reaching one of the specimen interfaces are then propagated toward a metallic grounded electrode and are converted in electric signals by a piezoelectric membrane. Downstream of the latter, an absorber avoids the reflection of the pressure waves.

The waves produced into the sample are propagated up to the piezoelectric transducer with a final amplitude depending on the acoustic impedances *Z* of the crossed materials, defined as the product between the acoustic velocity and the mass density. When the acoustic wave passes from a material with acoustic impedance $Z_1$ to a material with acoustic

impedance $Z_2$, the ratio of the transmitted pressure amplitude $p_2$ depends on the arriving pressure amplitude $p_1$ as follows:

$$p_2 = \frac{2Z_2}{Z_1+Z_2} p_1 \tag{2.6}$$

From the above equation, it may be deduced that it's necessary to optimize the continuity between the piezoelectric sensor and the sample in order to avoid the presence of gas. The acoustic impedance of the latter is several orders of magnitude lower than that of the solid materials, therefore, high values of reflection factors could be reached distorting the measurements.

In Figure 2.5, a schematic of the measurement setup for flat specimens is shown. On the left-hand side, the high voltage aluminum electrode is connected with the output of the DC voltage source $V_{dc}$ and with the pulse generator $V_p(t)$. A bias resistor $R_{DC}$ and a decoupling capacitor $C_C$ are inserted between the high voltage electrode and respectively the $V_{DC}$ source and the pulse generator in order to protect the system from high currents. A backing material is interposed between the high voltage electrode and the dielectric sample in order to optimize the interface by the point of view of the electrical and acoustic characteristics.

On the right-hand side of the sample, a grounded aluminum electrode is crossed by the pressure waves generated by the vibration of charges and it is adjacent to the piezoelectric transducer. The latter is faced to another aluminum electrode by means of a backing material. The electric signal produced by the interaction of the pressure waves with the piezoelectric membrane is measured between the grounded and the extreme right hand side electrodes and it is amplified before to be connected to an oscilloscope. The value of $R_{DC}$ is typically much greater than the impedance of the sample capacity at high frequencies. PMMA is typically used as backing material thanks to its acoustic impedance very similar to that of the dielectric material. A thin PVDF (polyvinylidene difluoride) film is typically used as piezoelectric transducer when the measurements are carried out at environmental temperature. If high temperatures are reached, a crystal sensor of Lithium Niobate is more reliable thanks to its stability in presence of temperature changes. The thickness of the piezoelectric membrane has an important role in the quality of the measurement since the wave crossing time through the film is strictly related to the spatial resolution of the measurements. Nevertheless, a thin film generates a small signal amplitude, therefore an optimization is necessary in order to reach the desirable output characteristics.

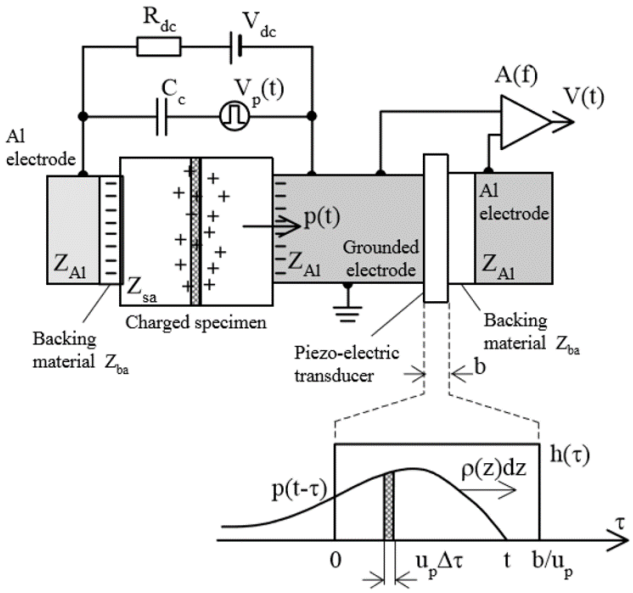


***Figure 2.5**. Measurement setup schematic for flat specimens – the figure is reproduced from [54]*

Considering the acoustic impedance of the backing material equal to that of the sample, it can be demonstrated that the pressure wave reaching the PVDF film, $p(t)$, can be calculated as follows [54]:

$$p(t) = \frac{Z_{al}}{Z_{al}+Z_{sa}}\left[\sigma_0 e_p(t) + u_{sa}\int_{-\infty}^{+\infty}\rho_Z e_p(t-\tau)d\tau + \sigma_d e_p\left(t-\frac{d}{u_{sa}}\right)\right] \quad (2.7)$$

Where:

- $Z_{al}$ and $Z_{sa}$ are respectively the aluminum electrode and the sample acoustic impedances;
- $\sigma_0$ and $\sigma_d$ are the superficial charge density at the sample flat surfaces;
- $\rho_Z$ is the volumetric charge density within the sample;
- $e_p$ is the pulsed electric field;
- $\tau$ is a time variable defined as $\tau = u_{sa}/z$;
- $z$ is the spatial coordinate;
- $u_{sa}$ is the sound velocity through the sample;
- $d$ is the sample thickness..

The spatial resolution of the PEA setup may be defined as the minimum distance $z$ over which a volumetric charge density variation can be measured. The spatial resolution is related to the pulse width $\Delta T_p$, the sample thickness d and the sound velocity in the sample (between 2000 m/s and 2200 m/s in most part of the commercial dielectric materials) as follows [55]:

$$\eta_{sa} = \frac{\Delta T_p}{d/u_{sa}} \tag{2.8}$$

Usually, $\eta_{sa}$ is comprised between 0.02 and 0.05. The spatial resolution of the PVDF film is calculated relating the time necessary for the pressure wave to cross the piezoelectric membrane with the time necessary to cross the sample [55]:

$$\eta_{PVDF} = \frac{b/u_p}{d/u_{sa}} \tag{2.9}$$

Where $b$ and $u_p$ are respectively the piezoelectric film thickness (with an order of magnitude of about 50-500 μm) and sound speed within (2600 m/s for PVDF film). Nonetheless, the ratio $b/u_p$ has to be much smaller than $\Delta T_p$ in order to accurately transform the measured pulse by means of signal deconvolution.

As mentioned above, the presence of material interfaces along the path of pressure waves leads to the reflection of part of the pressure amplitude depending on the change of acoustic impedances. Multiple reflection of the generated waves causes the distortion of the measurement output pattern. In particular, the high value of the sound velocity in the aluminium grounded electrode (6400 m/s) could lead to the superimposing of the doubly reflected waves generated at the closer sample interface with the direct wave started at the farther one. In order to avoid the waveform distortion due to the aforementioned phenomenon, an optimization of the material thicknesses of the PEA measurement setup has to be carried out. Nevertheless, since the acoustic impedances depend on the temperature and on the mechanical stress of the materials, the status of the sample has to be well known before the beginning of the PEA measurements. In fact, the clamping force necessary to guarantee the adhesion between the facing surfaces can generate a compression and, therefore, a variation in the volumetric mass density.

With reference to Figure 2.5, the voltage signal reaching the piezoelectric membrane has an order of magnitude of some mV. In order to measure this small signals by means of an oscilloscope, the voltage outgoing from the sensor must be amplified with a gain of about 40 dB.

In order to obtain a reliable space charge pattern at the output of the PEA setup, the outgoing signal of the amplifier, measured by the oscilloscope, has to be deconvoluted and calibrated. In Figure 2.6, an example of deconvolution procedure is shown. The deconvolution aims to correct the distortion resulting at the amplifier deriving by reflections at the interfaces close to the piezo-electric membrane and by the frequency

response characteristic of the measurement circuit. The aforementioned distortion can be considered as a systematic error leading the output signal to be the result of the following convolution [54]:

$$v_S(t) = h(t) * \rho(t) \tag{2.10}$$

where $v_S(t)$ is the output signal, $h(t)$ is the impulse response of the system, $\rho(t)$ is the charge density and * indicates the convolution operation.

By the determination of $h(t)$ the charge density can be calculated by the means of a deconvolution process. By obtaining the Fourier transforms in frequency domain of the above functions, the convolution relation can be expressed as follows [54]:

$$V_S(f) = H(f)R(f) \tag{2.11}$$

where $H(f)$, can be considered as a "transfer function" of the measurement system. The transfer function can be evaluated by applying a small electric field at the sample and measuring the measurement output signal. In these conditions, it can be assumed that the charges are laid exclusively at the electrode interfaces while no charge is present in the bulk of the dielectric. With this assumption, the charge density on the electrode can be analytically calculated as [54]:

$$\sigma_0 = \varepsilon_0 \varepsilon_r \frac{V_{DC}}{d} \tag{2.12}$$

$$\rho_0 = \frac{\sigma_0}{\tau_S u_{sa}} \tag{2.13}$$

where $\tau_S$ is the sampling time due to the resolution of the oscilloscope and $V_{DC}$ is the applied voltage. The measurement output in the aforementioned conditions leads to obtain two peaks with different heights due to the partial absorption of the pulse generated at the farthest electrode. The higher peak measured at the oscilloscope can be compared with the calculated value of $\rho_0$ in order to evaluate the transfer function. Since $\sigma_0$ is an impulse, the Fourier transform of $\rho_0$ is a constant [54]:

$$R_0(f) = \frac{\varepsilon_0 \varepsilon_r V_{DC}}{d \tau_S u_{sa}} \tag{2.14}$$

The transfer function is therefore determined by the calculation of $R_0(f)$ and the Fourier transform of the measured signal output $V_0(f)$ *[54]*:

$$H(f) = \frac{V_0(f)}{R_0(f)} \tag{2.15}$$

The Fourier transform of the de-convoluted space charge measurement is therefore [54]:

$$R(f) = R_0(f)\frac{V_S(f)}{V_0(f)} \tag{2.16}$$

Small values of $V_0(f)$ occurring at high frequencies lead to divergent values of $R(f)$, therefore, a Gaussian corrective function $G(f)$ has to be applied as low pass filter. The deconvoluted output in frequency domain is therefore [54]:

$$V_{decon}(f) = G(f)R(f) \tag{2.17}$$

The final expression of the deconvoluted signal $V_{decon}(t)$ is, therefore, obtained by operating its inverse FFT.

Once the output deconvoluted signal is obtained in mV, a further operation is necessary in order to calculate the value of space charge in C/m$^3$. Assuming that the pulsed voltage is square shaped, the following expression can be used in order to convert the output deconvoluted signal in space charge [54]:

$$v_{decon}(t) = K\rho \tag{2.18}$$

where $K$ is calculated on the basis of a comparison with the signal obtained from a known value of space charge.

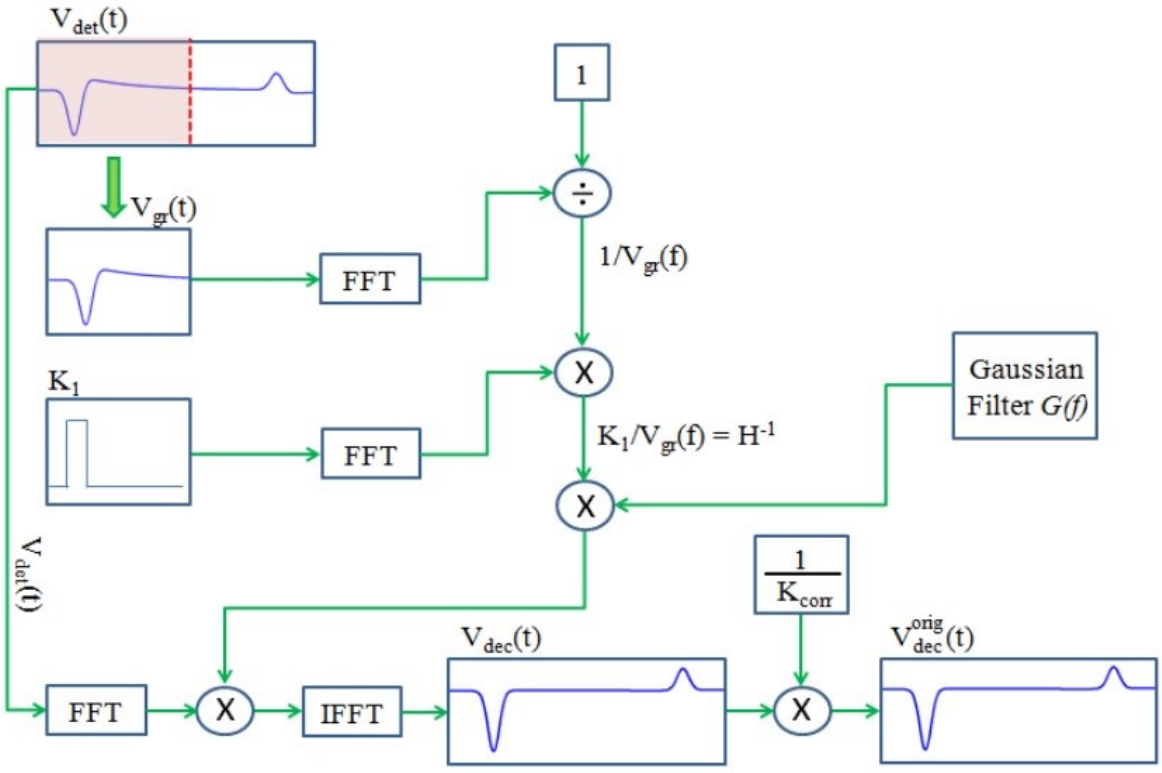


***Figure 2.6**. Example of Deconvolution*

### 2.2.2 PEA method for cables and mini-cables

The In 1990, K. Fukunaga and its group developed for the first time the application of the PEA method to cables [56].

The space charge measurement by PEA method in cables and mini-cables is a reproduction of the above described principles on cylindrical geometry. With reference to Figure 2.5, the upper and lower electrodes are substituted by the inner and outer semiconductive layers. The pulsed voltage generating the pressure waves is therefore applied between the cable conductor and an external flat or rounded electrode adjacent to the outer semiconductive layer. With reference to Figure 2.7, the space charge distribution can be measured in a portion of cable having sizes depending on the extensions of piezoelectric membrane and the contact surface between the cable outer and the bottom electrode.

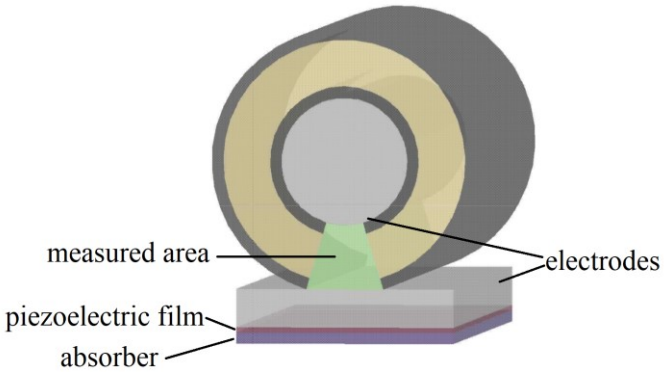


***Figure 2.7****. Space charge measurement on a cable portion by PEA method*

Unlike the application of PEA method to flat specimens, in cable systems, one of the two electrodes is not directly accessible. For this reason, various measurement setups have been developed in the last decades for the application of the PEA method on cables and mini-cables. The latter are commonly considered as a good solution for the qualification of semiconductive-dielectric-semiconductive compounds. The typical structure of a mini-cable is shown in Figure 2.8.

In all setups described below, the pulse generator output is indirectly connected to electrodes of the measurement area. This leads to obtain a deformed and delayed waveform at the interfaces of the dielectric portion in which the space charge has to be measured. The main purpose of the different approaches is to find an optimized solution to apply the pulsed electric field to the measured area based on the cable thickness and length.

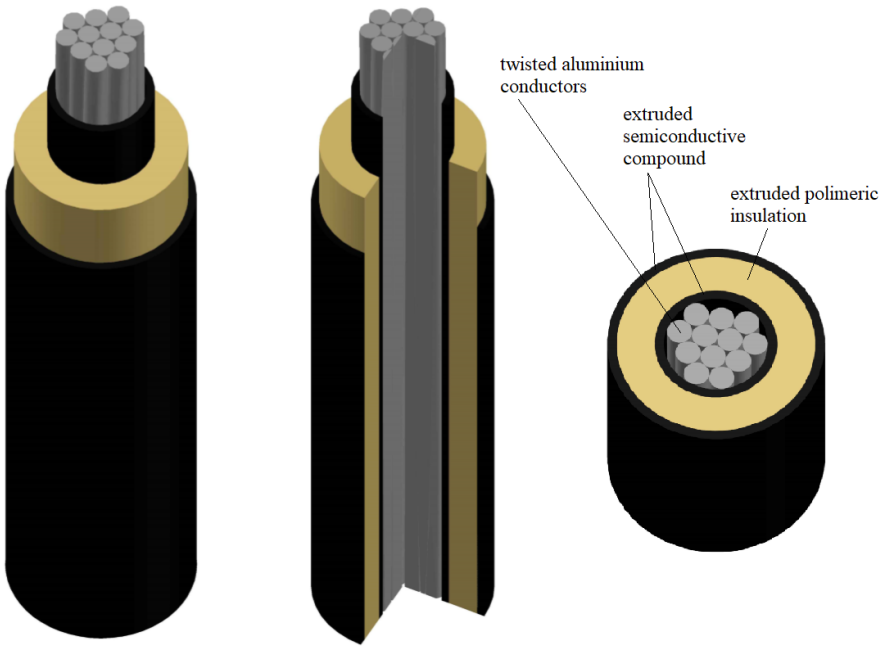


***Figure 2.8**. Typical mini-cable for tests under HVDC stress*

The first PEA measurement setup for cables described in this chapter and here called Setup 1 is illustrated in Figure 2.9. It was proposed for the first time by K. Fukunaga et alii [56] and derives directly from the configuration adopted in the case of flat specimens shown in Figure 2.5. In this approach, the HVDC supply and the pulsed voltage are both applied to the cable conductor. In Figure 2.10 a schematic of the Setup 1 is shown where a bias resistor $R_b$ is interposed between the HVDC source and the cable conductor while a capacitor $C_0$ decouples the latter from the pulse generator output. The sizes of the cable are taken into account through the impedance $Z_{cab}$ and the capacitance $C_{cab}$. In order to maximize the amplitude of $V_{sa}$, the impedance of $C_x$ has to be much higher than that of $C_0$. The schematic shown in Figure 2.10 is valid if the cable specimen is short enough to be treated as a lumped capacitance within the frequency region of the pulsed voltage [57]. For long cables it should be considered that the pulses are reflected at the terminals due to the impedance mismatch. For this reason, the Setup 1 is inapplicable to cables with length up to 1 m. In the first version of the Setup 1, a round PEA cell electrode was faced to a sector of the outer semiconductive layer of the cable specimen [58,59]. In this way, the curvatures of the ground electrode and cable external surface must be the same, therefore customed PEA cells should be created. Moreover, the impossibility of obtaining in practice a perfect contact of the facing surfaces leads to the presence of air gaps responsible of reflection of a part of the pressure waves. In order to overcome the aforementioned disadvantages, the configuration of the Setup 1 illustrated in Figure 2.8 was proposed by M. Fu et alii in 2000

[60]. In this case, the absence of air gaps in the contact surface between the semiconductive layer and the ground electrode is guaranteed by a clamping force applied to the cable.

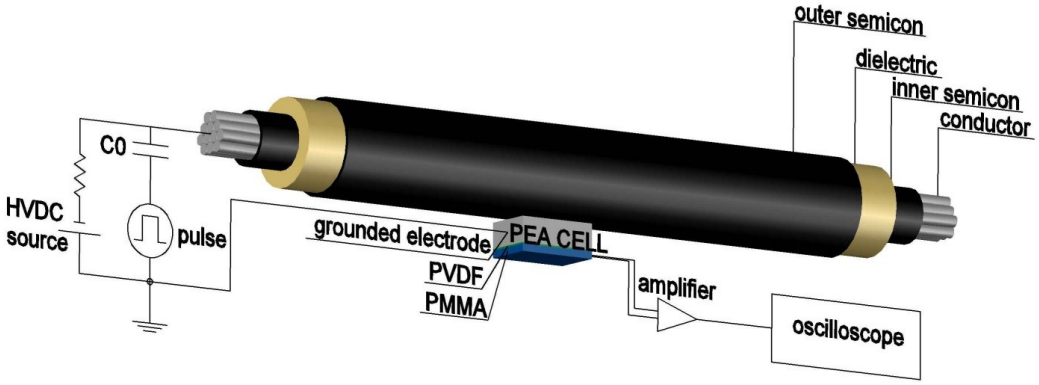


***Figure 2.9**. Setup 1: pulsed voltage applied to the cable conductor*

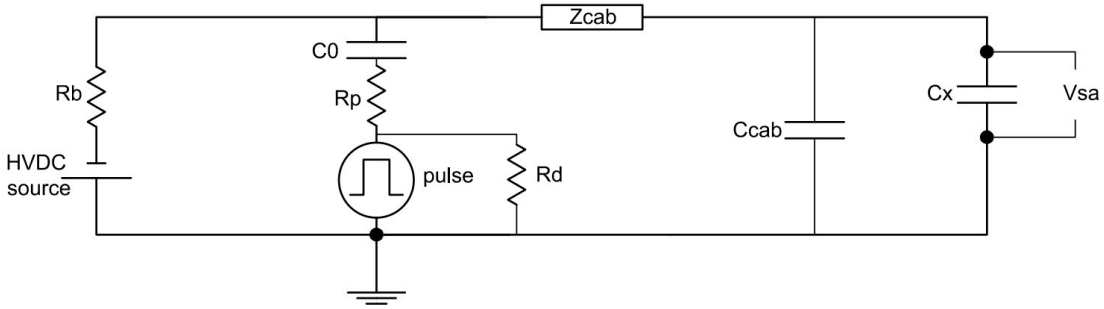


***Figure 2.10**. Schematic of the Setup 1*

In Figure 2.11 the PEA configuration here called Setup 2 is shown, This setup is detailed in [61] and it is based on applying the pulsed voltage to two symmetric conductive tapes wound around the outer semiconductive layer at the sides of the measurement area. The dielectric layer capacity transmits the pulse, therefore, the decoupling capacitor needed in Setup 1 is not needed. As shown in Figure 2.11, the outer semiconductive layer is partially removed in order to limit the transmission of the pulse directly through the cable surface. In Figure 2.12, the schematic of the Setup 2 is show. As it can be seen, the pulsed voltage is applied at the cable conductor by the means of two equivalent capacitances $C_1$. The areas between the side tapes and the measurement region can be modelled as a capacitive impedance $Z_g$. Due to the partial removal of the outer semiconductive layer, the Setup 2 can be considered as a destructive method. Nevertheless, the partial stripping of the external semiconductive layer induces a floating voltage on the surface adjacent the grounded electrode of the PEA cell which is no longer uniformly grounded. For this reason, this measurement setup is not applicable for long cables [54].

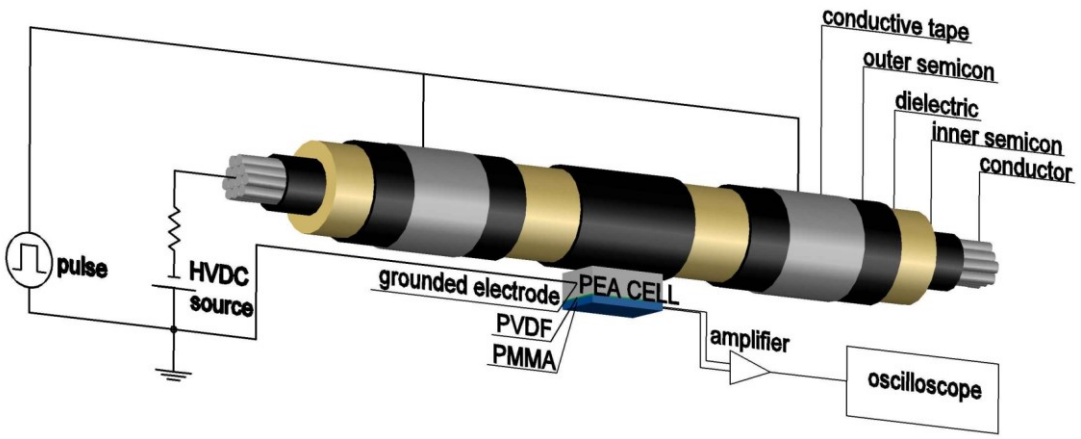


***Figure 2.11**. Setup 2: pulsed voltage applied to the partially stripped outer semiconductor*

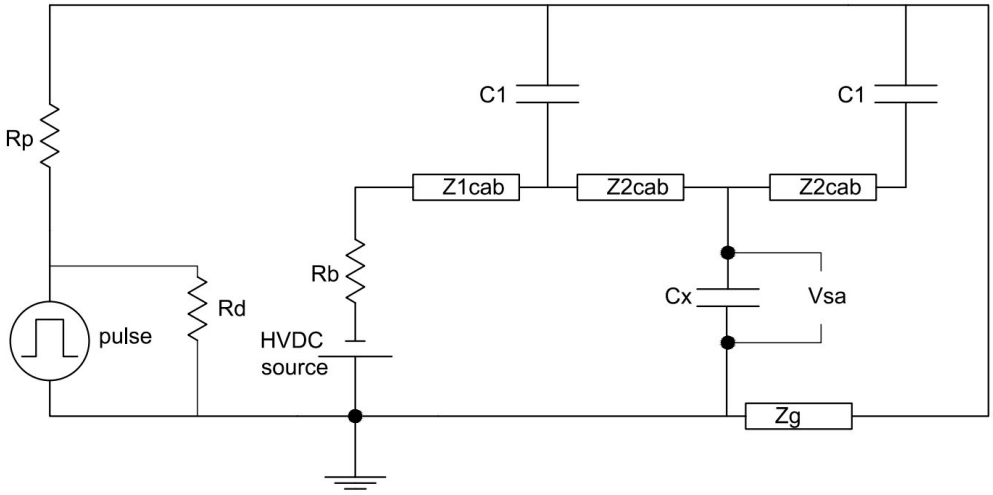


***Figure 2.12**. Schematic of the Setup 2*

In Figure 2.13, the PEA configuration here named Setup 3 is shown. In this configuration, the pulsed voltage is applied directly to the outer layer of the measure area through a conductive tape wound around the cable. In the first version proposed by N. Hozumi et alii [57], a PET film was interposed between the aforementioned conductive layer and the aluminum block of the PEA cell in order to decouple the measurement devices from the high voltage. Compared to the other setups, in this case, the pressure waves have to cross two additional layer before to reach the piezoelectric membrane. An improved version of the Setup 3, proposed by N. Hozumi et alii in 1994, consists in the application of the pulsed voltage to the PEA cell electrode and in the decoupling of the amplifier from the oscilloscope by means of an optical fiber [62].

The use of this method requires the insulation of the PEA cell and of the amplifier from the ground. With reference to Figures 2.13 and 2.14, the impedance $Z_g$ is mainly resistive.

Since the pulsed voltage is directly applied to the measurement region, this setup is less influenced by reflection and attenuation of the HV signal than the other methods described above [57]. This makes this method applicable for long full size cables as proposed by N. Hozumi et alii in 1998 [63]. In this case, the removal of the outer layers with respect to the semiconductor makes this PEA setup inapplicable to finished cables.

In this configuration, the properties of the E/O and O/E converters, particularly in terms of sampling rate, has to be taken into account in order to avoid to cut high frequencies contributes. For this purpose, an improved version of the Setup 3 is proposed in [55] and it involves the direct connection between the amplifier and the oscilloscope. The latter is therefore insulated from the ground and connected to a PC by means of optical fiber.

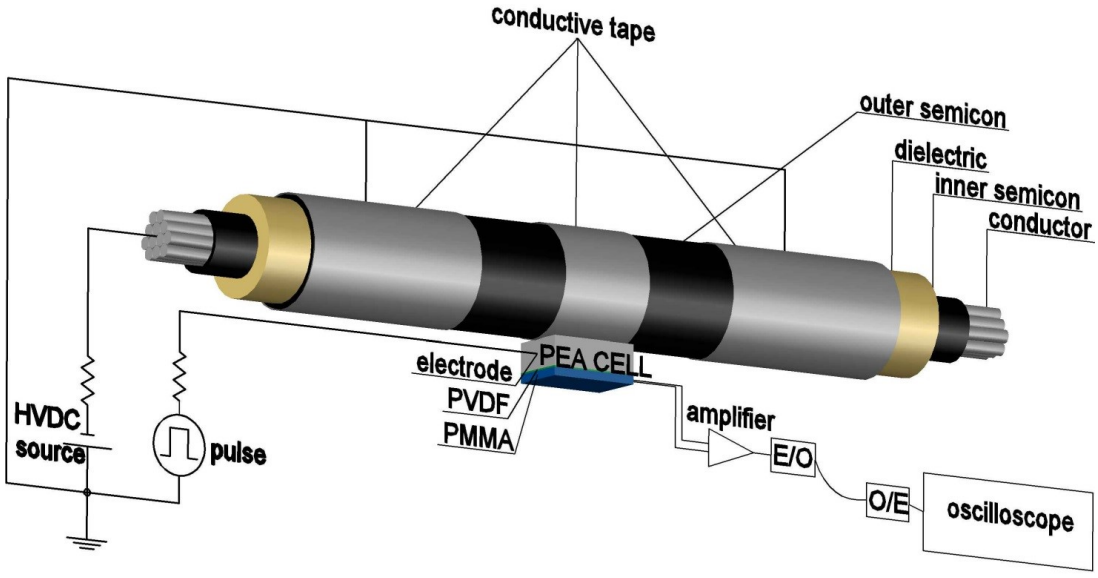


***Figure 2.13**. Setup 3: pulsed voltage applied to the PEA cell's electrode*

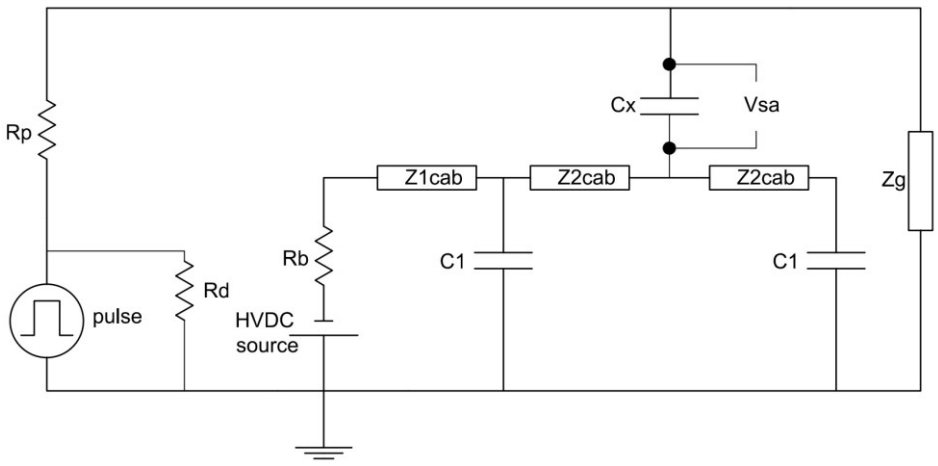


***Figure 2.14**. Schematic of the Setup 3*

As described above, the measurement setup for a certain sample should be chosen considering the waveform of the pulse reaching the measure area. For this reason, absorptions, reflections and delays of the electric pulse should be considered. In particular, the delay line of the pulse generator output cable must carefully designed with the aim to minimize the distortion of the pulsed voltage waveform. In Figure 2.15, the effect of reflection of pulses is schematized. The phenomenon can significantly affect the space charge measurement depending on the cable length, circuital impedances and schematic.

Many researchers have proposed the use of delay line for pulse generator few hundred meters long in order to perform space charge measurements by PEA method on full size cables [64].

As mentioned above and experimented by many researchers, several parameters have an important role in the reliability of space charge measurements by means of the PEA method. The length of the delay line, the pulse width, the ground electrode and piezoelectric film thickness should be designed considering the characteristics of the cable to test [65]. Therefore, the suitability of a commercial PEA system should be verified considering the cable specifications. Moreover, an acoustic model should be implemented to evaluate the reflected pressure waves reaching the piezoelectric membrane [66].

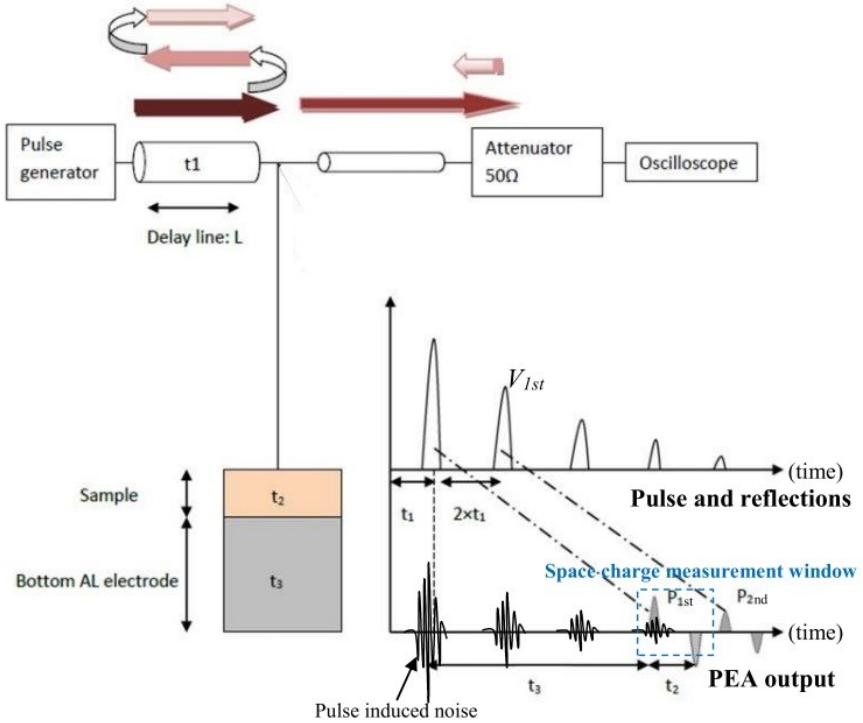


***Figure 2.15**. Effect of the pulse generator output delay line – figure reproduced from [64]*

Hitherto, the PEA method is a destructive test for finished cables. Alternatively, this technique should be used on unfinished cables, once completed the extrusion of the outer semiconductive layer.

## 2.3 Case study - space charge measurements on a model cable

In this section, the results of a space charge measurement campaign are reported and discussed. The measurements described were performed using the PEA measurement setup for model cables implemented at the LEPRE laboratory of the University of Palermo. In particular, using a commercial PEA cell, measurements were carried out on a model cable subjected to HVDC stress and inside which a current flows. In Figure 2.16, the implemented PEA setup is shown. The HVDC voltage was applied by means of an 125 kV HVDC generator whilst the pulses were generated with an amplitude up to 8 kV and a width of 90 ns. In order to limit the current in the HVDC generator, a 100 MΩ resistor was connected between the generator output and the cable conductor.

The pulses were applied to the outer semiconductive layer of the model cable by means of two conductive tapes wounded around the sample in proximity of the measure area and symmetrically respect to the PEA cell. As shown in Figure 2.17, on the basis of the experience of the LEPRE laboratory staff, the width of the wounded tapes was set to 20 cm. The distance between the conductive tapes and the boundary of the PEA cell was equal to 5 cm whilst the distance from the remaining part of the cable shield was 35 cm.

The cable under test featured a conductor with a diameter of 10 mm, semiconductor thicknesses of 1 mm and a 5 mm thick thermoplastic insulation. In order to establish a radial temperature gradient in the dielectric layer, an ad hoc transformer primary was created. By making a current flow in the 350 turns of the primary, a current of up to 300 A is induced in the secondary consisting of the cable under test closed to form a coil. The induced current in the mini-cable is controlled by a Rogowsky ammeter whose analog signal is read by a PRY-CAM Minilog® and sent to a PC for the control of an AC generator. This control is carried out both taking into account a pre-set time course of the current, and the value of the temperature outside the cable in order not to exceed critical thresholds that would definitively damage the equipment.

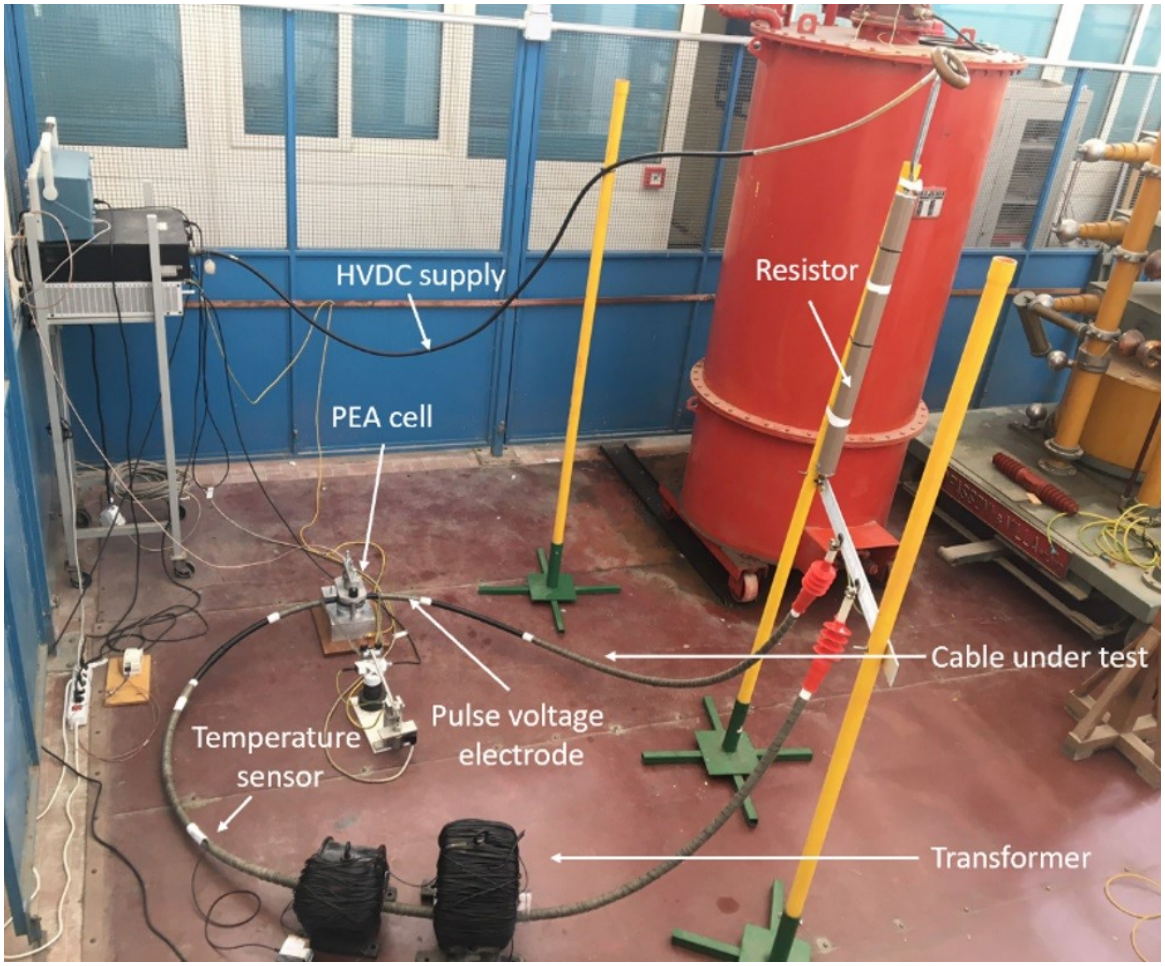


***Figure 2.16**. PEA measurement setup for mini-cables at LEPRE Laboratory*

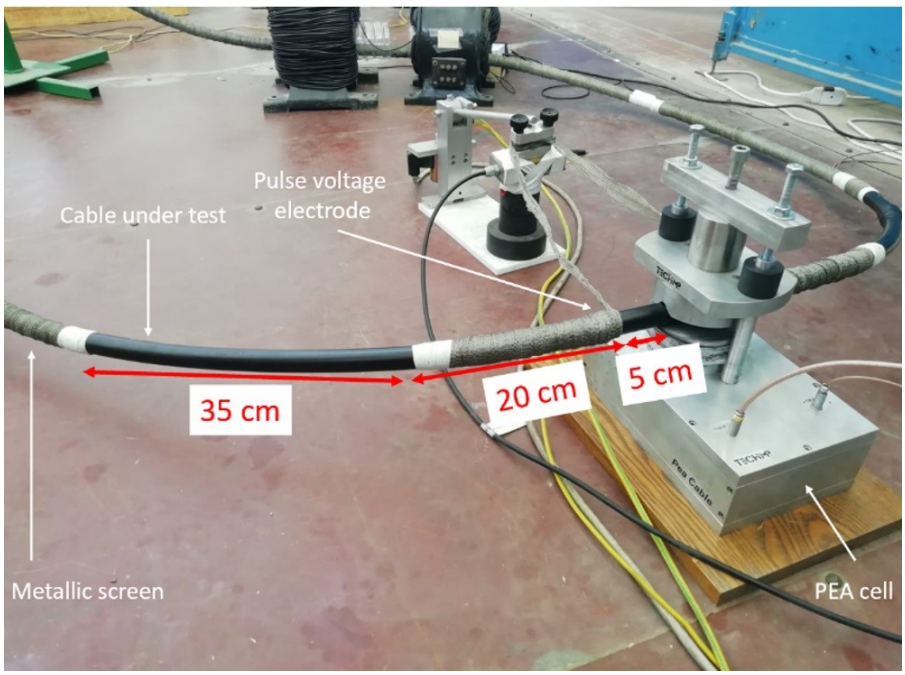


***Figure 2.17**. Geometrical properties of the metallic tapes for the voltage pulse application*

The temperature was measured by a PT100 sensor adjacent to the external surface of the cable and isolated from the external environment. The analog signal coming from the PT100, as well as that of the applied voltage, read directly by the HVDC generator, are sent to two respective PRY-CAM Minilog® which allow transmission to a PC with Modbus RTU protocol. The conductor temperature is obtained by means of a thermal model capable of running in real time. Once the setup of PEA measurements had been arranged, several experiments were conducted in order to obtain reliable and repeatable space charge measurements. After numerous attempts, it was decided to increase the thickness of the ground electrode by 18 mm in order to temporally move forward the arrival of the first impulse to the piezoelectric sensor. In fact, the first impulse arrived when the disturbances attributable to the pulsed voltage were still legible by the oscilloscope. With this modification to the commercial PEA cell used, it was possible to proceed with the deconvolution and calibration of the output signals from the amplifier.

In this section, the results of two tests are reported. A 10 m long cable has been subjected to 90 kV for a duration of 1 h with and without the application of current load. the tests were carried out at a distance of 24 h from each other in order to prevent the charges accumulated at the end of the first from influencing the measurements during the second. However, the tests were carried out in conditions of very similar humidity and ambient temperature, namely 30 °C and approximately 40% relative humidity.

In the case study described in this section, a pulsed voltage with an amplitude of 6 kV was applied. Under these conditions and without application of current load, the space charge profiles shown in Figure 2.18 were obtained. As can be seen, already after 30 minutes, the charge density peaks relative to the interfaces between the dielectric and the semiconductive layers are smaller and larger. This behavior can be attributed to the charge injection to the interfaces or to any accumulation of heterocharges that cannot be measured with the available setup due to resolution limits.

In Figure 2.19, the space charge profiles obtained by means of application of an average current of 264 A is shown. In order to obtain this current value, a voltage of 194 V was applied to the terminals of the primary of the transformer. as the temperature of both the primary and secondary, inevitably, the current dropped to 245 A after 60 minutes. The time trends of the measured external temperature of the cable and of the estimated one at the conductor are shown in Figure 2.20. After one hour from the start of the test, the conductor reached a temperature of 73.4 ° C while the external surface was 61.2 ° C. As can be seen

from Figure 2.19, after one hour from the start of the test, when the thermal difference on the dielectric thickness is now at 12.2 ° C, there is an accumulation of charge in the bulk of the insulation near the conductor. The slope of the radial charge profile is decreasing from the inside towards the outside in accordance with what can be deduced from the conductivity models described in Chapter 1. However, there is a distinct difference in the charge density values measured and predicted by the aforementioned conductivity models. These discrepancies can be attributed in part to the spatial resolution of the PEA measurement which leads to overestimating the width of the peaks at the electrodes and underestimating the amplitude. Furthermore, as noted above, the conductivity models do not take into account the phenomenon of trapping and de-trapping nor of the injection at the electrodes enhanced by the roughness of the facing surfaces.

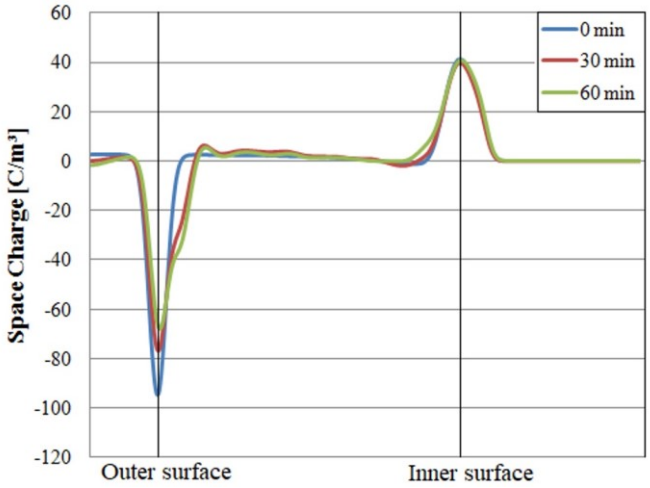


***Figure 2.18**. Charge distribution with the cable kept at environment temperature - after 0 (blue line), 30 (red line) and 60 minutes (green line) from the test start.*

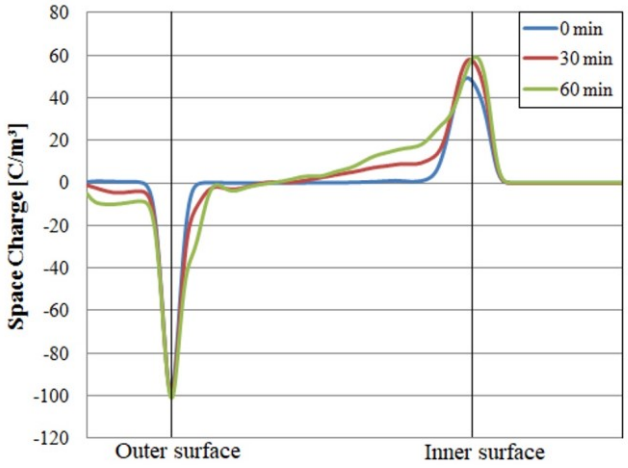


***Figure 2.19**. Charge distribution with the cable heated up by an average current of 264 A - after 0 (blue line), 30 (red line) and 60 minutes (green line) from the test start.*

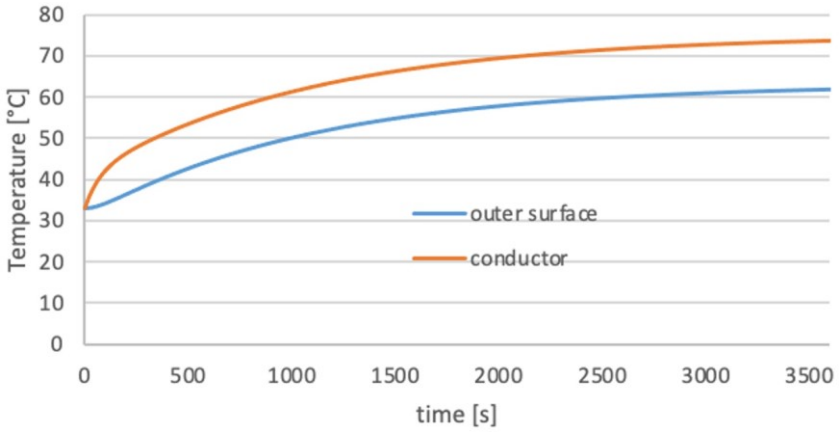


***Figure 2.20**. Time trend of the cable temperatures*

However, as also claimed by various researchers, the role of the temperature gradient in the phenomenon of the accumulation of space charge is greater the greater the dielectric thickness. Unfortunately, precisely in these conditions, space charge measurements using the PEA method are less reliable due to the attenuation of the acoustic signals.

## 2.4 Conclusions

In this chapter, the state of the art of space charge measurement methods has been summarized. In particular, the attention was focused on the method called Pulsed Electro-Acoustic (PEA).

In addition to the PEA method, the technique called Thermal Step Method has been briefly described. Both these methods are recommended for Pre-Qualification tests by the IEEE Std 1732TM-2017 standard.

The working principle of TSM is based on the application of a thermal step across the dielectric thickness in order to generate a temporary displacement of the charges within. This affects the amount of charges at the interfaces generating a current with a typical order of magnitude of pA if the dielectric is short-circuited. The generated current signal is then amplified, deconvoluted and calibrated in order to obtain the relation between the charge density and the radial coordinate.

The thermal step can be generated heating the conductor or cooling the outer surface. In the first case, the short-circuited cable works as the secondary of a transformer and it's crossed by a current of several kA. Alternatively, the cooling of the outer surface is carried

out by means of a cylindrical thermal diffuser crossed by a cold fluid and adjacent to the cable' surface. Whilst the inner heating method provide information about the whole cable, the outer cooling is used for get space charge measurements in small portion of the sample (20-40 cm).

Contrary to TSM, the PEA method returns the radial distribution of space charge on a narrow cable sector delimited axially and angularly. The PEA method is based on the interaction between the charges arranged in the dielectric and a pulsed electric field superimposed on the DC voltage applied to the sample. This interaction causes a vibration of the charges in the dielectric with consequent emission of pressure waves which are picked up by a piezoelectric sensor arranged downstream of one of the two electrodes. Normally, the piezoelectric film is adjacent to the ground electrode. Since the 1980s, PEA setups and cells have been developed for flat specimens while, since the last few decades, systems suitable for cable measurements have been developed.

Whilst measurements on flat specimens, especially those with a thickness of less than 1 mm, are considered reliable and replicable, several difficulties are encountered in carrying out measurements on cables. One of these difficulties lies in the specificity of the performance of the PEA cell on a particular cable geometry. In particular, as described in detail in this chapter, the spatial resolution of the measurement system strongly depends on the characteristics of the sample. For this reason, a given commercial PEA cell is suitable for cables with dielectric thickness within a fairly narrow range. Another important limitation of the PEA method is the fact that there cannot be layers of materials of different densities between the dielectric and the piezoelectric sensor. In fact, high differences in density correspond to high differences in the speed of sound. This causes high reflection indices and, consequently, to a reduction in the amplitude of the signal reaching the piezoelectric sensor.

In the last section of this chapter, the results of measurements made with a commercial PEA cell on a mini-cable insulated with thermoplastic material are described. A PEA setup for model cables was assembled at the LEPRE high voltage laboratory of the University of Palermo. In this chapter, the results of two tests performed under similar conditions are described except for the load current flowing through the conductor. In particular, the same test, lasting 1 h, was performed first keeping the cable at room temperature and then subjected to an average load current of 264 A. The measurements show that the temperature drop over the insulation thickness generates, beginning from about 30 minutes from the

start of the test, an accumulation of space charge in the bulk of the dielectric layer near the interface with the conductor.

# Chapter 3
## Design of a novel Pulsed Electro-Acoustic apparatus

As discussed in the previous chapters, one of the main goals of the space charge measurements is to investigate the effect of the space charge accumulation occurring under HVDC stress on the electric field distribution. With reference to the widespread accepted ageing models, such as the Inverse Power Law, the achievement of high electric fields can accelerate the premature ageing of portion of insulation until it leads to its breakdown [67-70]. As discussed above, space charge can be accumulated within a dielectric layer because of charge injection at the interfaces with conductive or semiconductive layers or due to phenomena occurring into the bulk. In particular, in full size HVDC cables and accessories, the thermal gradient over the insulation thickness leads to space charge accumulation within the bulk of the dielectric layer. In addition, it has been demonstrated that the higher is the insulation thickness, the greater is the role of the thermal gradient on the modification of the electric field distribution.

Most of the PEA systems for flat specimens described in the literature are suitable for space charge measurements on thin samples, generally not more than 1 mm [71-75]. Relatively thin samples may have inadequate homogeneity to replicate the characteristics of the bulk of the dielectric layer of a cable or joint. Moreover, the ratio between the roughness of the outer surfaces and the thickness of the specimen can be such as to have a non-affected area of the material significantly reduced with respect to the thickness of the sample. Nevertheless, it would be particularly difficult to study the effects of a temperature gradient on the accumulation of space charge on a thin sample. On the other hand, to date, the use of the PEA method on cables and mini cables cannot be considered sufficiently reliable to provide quantitative information on the distribution of volumetric charge density. These reasons have led the author to consider the possibility of designing a PEA apparatus useful to measure the accumulation of space charge in flat specimens of relatively high thickness and to consider the possibility of applying a temperature difference between the two faces of the sample. It is the author's opinion that the use of the PEA method on samples with a thickness of a few mm can be useful to study of space charge phenomena in conditions similar to those that occur on HVDC cables and accessories.

The novel PEA apparatus has been optimized for specimens with a thickness between 3 and 5 mm subjected to DC voltage up to 100 kV. Thanks to this configuration, it is possible to subject flat dielectric specimens to conditions in terms of electric field and thermal gradient comparable to those occurring on operating HVDC cables and accessories. In the Table 3.1, the design targets are listed.

***TABLE 3.1.*** *Main design targets*

| **Parameter** | **symbol** | **min.** | **max.** | **unit** |
|---|---|---|---|---|
| **DC voltage** | *HVDC* | 30 | 100 | kV |
| **Sample thickness** | $d_{sa}$ | 3 | 5 | mm |
| **Sample diameter** | $diam_{sa}$ | 160 | 200 | mm |
| **Semicon thickness** | $d_{sem}$ | 0 | 1 | mm |
| **Spatial resolution due to the pulse width** | $\eta_{ep}$ | _ | 8 % | __ |
| **Spatial resolution due to the sensor thickness** | $\eta_{PVDF}$ | _ | 1.5 % | __ |
| **HV electrode diameter** | $diam_{HV}$ | 10 | 12 | mm |

In the first section of this chapter, based on size and type of samples to be subjected to space charge measurement, the thicknesses of the various components of the PEA cell have been optimized, as well as the optimal duration of the voltage pulse to be applied. In the second section the High Voltage (HV) electrode design criteria have been described whilst, in the third, a pulse generator has been designed with the possibility of carry out polarity reversal procedures. In the fourth section, the choice of the signal amplificatory to connect to the piezoelectric sensor is justified whilst, in the fifth, the temperature control of the PEA cell is described. In particular, a thermal study of the heating and cooling systems of the PEA apparatus, useful to apply a thermal gradient to the sample, is presented. After having calculated the temperature distribution inside the sample in different scenarios, the space charge and electric field distributions are calculated by means of a conductivity model for dielectrics as described in the sixth section. At the end of this section, the expected space charge distribution for a case study, obtained by means of PEA cell simulation, is presented. In the seventh section, a set of drawing of the designed PEA cell is shown with the aim to illustrate the structure and the assembly procedure of this device. Finally, this chapter terminates with a conclusion section.

## 3.1 Requirements for thicknesses of the PEA cell components and optimal voltage pulse width

The working principles of the PEA method have been discussed in the previous chapter. In this section, the role of the component' size has been investigated with the aim to obtain a spatial resolution for the space charge distribution measurements less than the target value of 8% of the sample thickness.

In Figure 3.1, a block diagram of the proposed PEA cell and the electric circuit of the external apparatus are shown. Unlike the PEA system for flat specimens described in the previous chapter, in the novel apparatus, the dielectric sample is interposed between two semiconductor sheets. This choice aims to reproduce a condition as similar as possible to that occurring in HVDC cables in terms of injection and spatial distribution of charge in proximity of the interfaces with the dielectric layer. On the other hand, the semiconductive material typically has an acoustic impedance similar to that of the sample under test.

The system shown in Figure 3.1 consists of HV, ground and bottom electrodes, two semiconductive layers, the dielectric sample, the piezoelectric sensor, the absorber as well as the external electric circuit composed of the HVDC generator, the resistance R, the pulse generator ep(t) and the capacitor C.

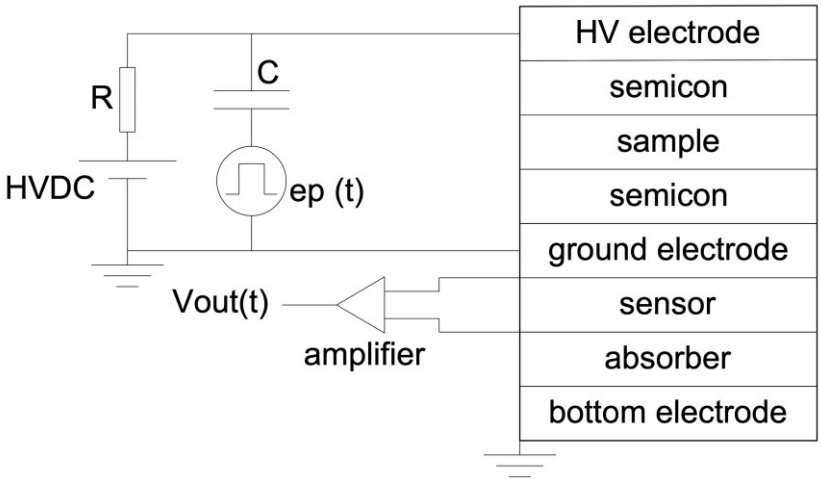


***Figure 3.1.*** *Block diagram of the PEA cell.*

The maximum pulse width depends on the spatial resolution of the PEA apparatus as follows [55]:

$$\Delta_{ep} \leq \eta_{ep} \cdot \frac{d_{sa}}{v_{sa}} \tag{3.1}$$

Where $\eta_{ep}$ is the spatial resolution of the space charge measurement due to the duration of the voltage pulse, $\Delta_{ep}$ is the pulse width at half height, $d_{sa}$ is the sample thickness and $v_{sa}$ is the velocity of the acoustic waves through the sample. The speed of sound in polymers used commercially as dielectrics is between 2000 and 2200 m/s, therefore, considering the minimum sample thickness reported in Table 3.1, the maximum $\Delta_{ep}$ should be equal to 120 ns [55].

As described in Chapter 2, the acoustic waves produced by the interaction between space charge and voltage pulses are converted in electric signals by means of a sensor based on the piezoelectric characteristics of a poled PVDF membrane. The amplitude of the signal is proportional to the space charge density whilst the delay depends on its position.

The maximum sensor thickness depends on the spatial resolution of the PEA apparatus as follows:

$$d_{PVDF} \leq \eta_{PVDF} \cdot \frac{d_{sa}}{v_{sa}} \cdot v_{PVDF} \tag{3.2}$$

Where $\eta_{PVDF}$ is the spatial resolution of the space charge measurement due to the sensor thickness, $d_{sa}$ and $v_{sa}$ are specified above and $v_{PVDF}$ is the velocity of the acoustic waves through piezoelectric membrane, which can be assumed equal to 2600 m/s [55]. Considering the minimum sample thickness reported in Table 3.1, the maximum $d_{PVDF}$ should be equal to 53 $\mu m$.

The choice of the spatial resolutions reported in Table 3.1 considers the need to maximize the ratio between the duration of the voltage pulse and the crossing time of the acoustic waves through the sensor. This is to avoid that two successive pressure waves are transformed into a single “long” electrical impulse by the piezoelectric sensor.

In order to optimize the accuracy of the deconvoluted signal, the following condition should be satisfied [55]:

$$\frac{d_{PVDF}}{v_{PVDF}} \ll \Delta_{ep} \tag{3.3}$$

The condition (3.3) leads to minimize the sensor thickness and/or maximize the pulse width. On the other hand, the smaller the piezoelectric film thickness the weaker the signal output as well as the longer the pulse duration, the greater the spatial resolution of the PEA system. Based on these considerations, the aforementioned spatial resolution limit values have been chosen.

In order to determine the optimal thickness for the lower semiconductive layer and the ground electrode, the reflections of the generated acoustic wave shall be considered. In Figure 3.2, the path and the time distribution of the main expected acoustic waves which can reach the piezoelectric film are shown. In the framework of designing a PEA system, the analysis of the reflections is necessary to minimize the presence of reflected waves between the two main peaks referred to the charges accumulated at the two electrodes. For this reason and for sake of simplicity, only the charges accumulating in proximity of the interfaces between dielectric and semiconductive layers have been considered.

With reference to the Figure 3.2, $d_{sa}$, $d_{sc}$ and $d_{al}$ are the thicknesses of the sample, of the semicon and of the ground electrode respectively whilst $v_{sa}$, $v_{sc}$ and $v_{al}$ are the sound speed in the sample, in the semicon and in the ground electrode respectively. The sound speed in the semicon is equal to that in the dielectric, therefore, it can be assumed $v_{sc}$ between 2000 m/s and 2200 m/s. The velocity of the acoustic waves through the ground electrode, $v_{al}$, can be assumed equal to 6400 m/s, considering that it is made of aluminum.

The first acoustic wave that reaches the piezoelectric sensor is $S_1$, which comes from the interface between the dielectric sample and the lower semiconductor layer. As shown in the Figure 3.2, the time spent by $S_1$ to reach the sensor is the following:

$$t(S_1) = \frac{d_{sc}}{v_{sc}} + \frac{d_{al}}{v_{al}} \tag{3.4}$$

Which is the second wave detected by the sensor depends on the ratio between the thicknesses of the dielectric and the lower semiconductive layer as well as on the quality of the dielectric-lower semicon interface. If the lower semiconductive layer is applied separately from the dielectric sample, the roughness of the interfacing surfaces could lead to the reflection of waves as shown in the Figure 3.2 for the waves $S_1$' and $S_1$'''.

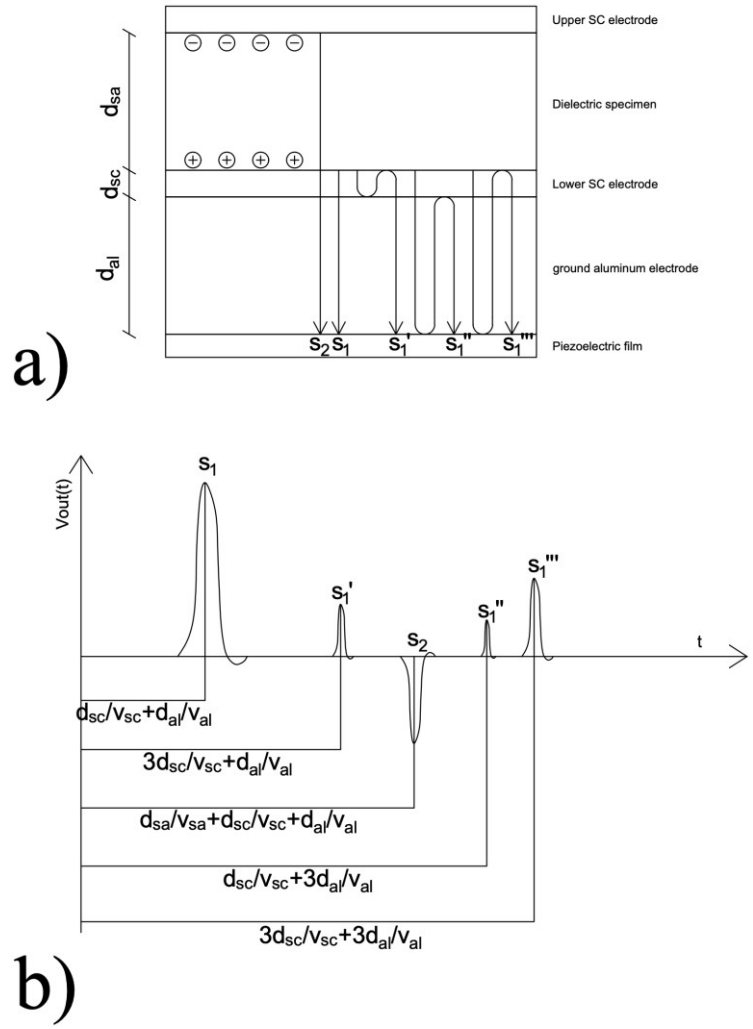


***Figure 3.2.*** *a) path of original and reflected waves; b) time distribution of original and reflected waves.*

In order to minimize the impact of waves reflection due to air gap between dielectric and lower semiconductive layer, a specimen where the semicon layer is physically attached to the dielectric should be used. In this case, the specimen reproduces the manufacture of an HVDC cable or joint. Moreover, in this configuration, since the sound speeds in semicon and dielectric are similar, no reflections should occur. Alternatively to providing an integrated dielectric-semicon specimen, silicon oil can be interposed between all the interfaces crossed by the acoustic waves. Any residual distortions of the output signal due to minor reflection can be eliminated by the deconvolution process.

With reference to the Figure 3.2, the peak $S_1''$ derives from the reflection of the peak $S_1$ firstly at the interface between the sensor and the ground electrode and secondly at the interface between the latter and the lower semicon layer. Since the mass density differences between semiconductive polymer, metal and piezoelectric film are significant, the

amplitude of $S_1''$ can reach the same order of magnitude as the main peaks. On the other hand, the time spent by $S_1$ to reach the sensor is the following:

$$t(S_1'') = \frac{d_{sc}}{v_{sc}} + \frac{3d_{al}}{v_{al}} \tag{3.5}$$

the acoustic wave $S_2$, coming from the interface between the dielectric and upper semiconductive layers, derives from the interaction between a charge quantity about equal to that accumulated at the lower dielectric surface. $S_2$ is characterized by a smaller amplitude than $S_1$ due to the partial absorption of the wave in the dielectric and it reaches the piezoelectric sensor after a time that can be calculated as follows:

$$t(S_2) = \frac{d_{sa}}{v_{sa}} + \frac{d_{sc}}{v_{sc}} + \frac{d_{al}}{v_{al}} \tag{3.6}$$

In order to avoid that $S1''$ reaches the sensor before $S_2$, the following condition shloud be satisfied:

$$t(S_1'') > t(S_2) \Longrightarrow d_{al} > \frac{d_{sa} * v_{al}}{2v_{sa}} \tag{3.7}$$

From condition (3.7), considering the aforementioned sound velocity and the maximum thickness of the specimen, it follows that the ground electrode should be thicker than 8 mm. Considering the requirements of the condition (3.7) and taking into account the need to delay the space charge signal with respect to the residuals of the disturbances from the voltage pulse, a thickness of 20 mm has been chosen for the aluminum ground electrode.

As it will be explained below, the temperature of the ground electrode is controlled by means of a heat exchanger with the feedback of an optic fiber sensor. As shown in Figure 3.3, a duct for the temperature sensor with a diameter of 2.5 mm and a length of 70 mm and a location for the heat exchanger tube are included into the design. As can be observed, the hole of the temperature sensor terminates 44 mm away from the projection of the edge of the piezoelectric sensor in order not to interfere with the transmission of acoustic waves. For the same reason, the seat of the heat exchanger tube is also located in the peripheral area. Thanks to the high thermal conductivity of aluminum, positioning both the temperature sensor and the heat exchanger tube away from the axis does not affect the effectiveness of the temperature control. Controlling the temperature of the earth electrode is also essential to avoid damaging the piezoelectric membrane or reaching temperatures that limit the reliability of the output signal. As indicated in Figure 3.3, the roughness of

the upper surface of the ground electrode must be limited to a value *Ra 0.2* (UNI EN ISO 1302:2004) in order to minimize reflections due to the presence of an air gap.

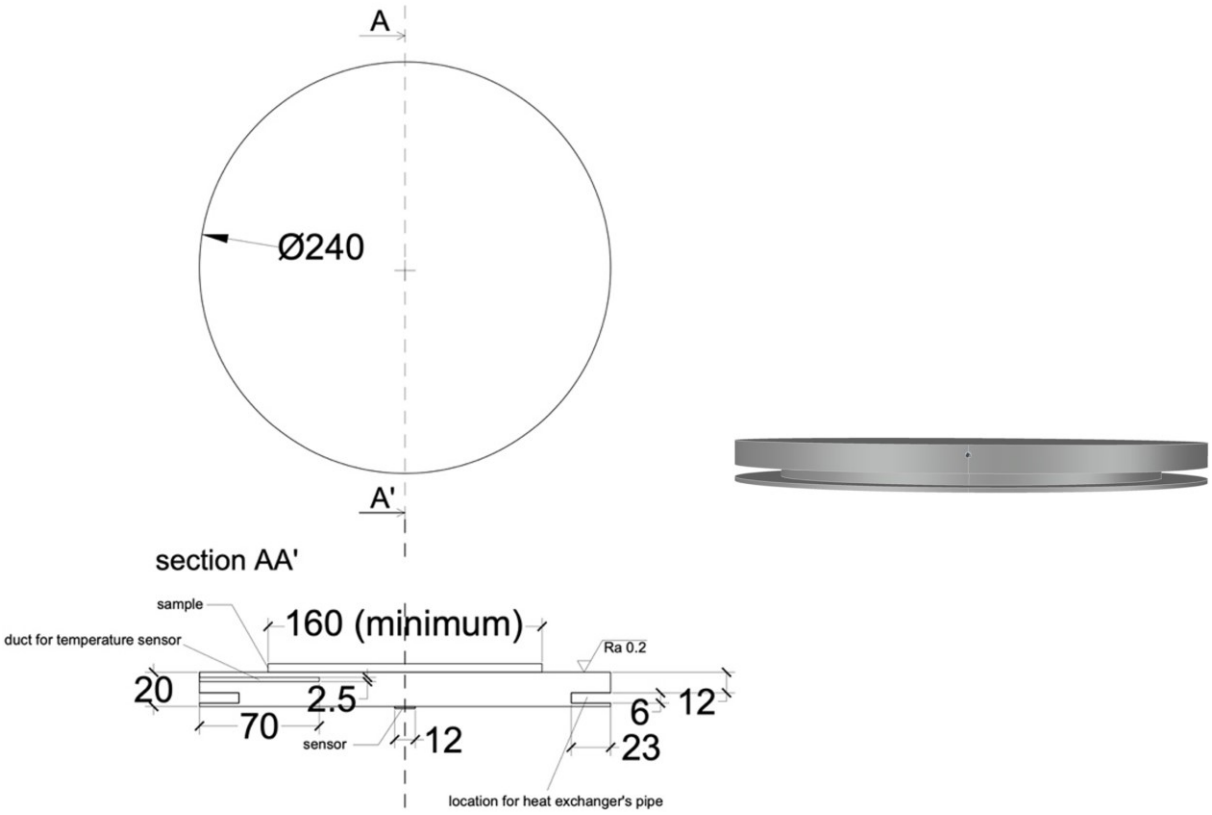


***Figure 3.3.*** *Aluminum ground electrode (units in mm)*

In the light of the considerations described above, a piezoelectric film available on the market can be chosen. PVDF is one of the most widely used piezo-polymers because its strong piezo- and pyro-electric response [76,77]. Moreover, PVDF has an acoustic impedance closer to dielectric polymers than conventional piezo-ceramic materials [78,79].

To date, the piezo-polymers available on the market transducer are characterized by high levels of piezo activity, low acoustic impedance, an extremely wide frequency range and a broad dynamic response, which contribute to lack of oscillations in the received output signal. The polymeric transducer is a flexible plastic film that can be easily cut and adhered to form transducers according to the user's needs.

In accordance with the need of reaching a spatial resolution as indicated above, a PVDF film like the one shown in Figure 3.4, with a thickness of 52 $\mu m$, has been chosen. The piezoelectric properties of PVDF begin to degrade once the temperature of 60 °C is exceeded . For this reason, as specified below, a temperature control of the ground electrode

is mandatory. The chosen PVDF sensor is coated with gold, therefore, the electrodes for the signal output can be bonded by means of silver loaded epoxy resin. To bond the piezoelectric film to the ground electrode, a low viscosity epoxy adhesive can be used with aim to minimize the presence of interfacial voids due to the surfaces roughness and to guarantee an acoustic impedance of the glue similar to that of the sensor. Moreover, the application of a sufficient pressure during cure is recommended by the sensor supplier. Finally, it is recommended to use a sharp scalpel to cut the PVDF sheet in order to limit fraying of the edges and avoid short-circuiting the two gold thin layers.

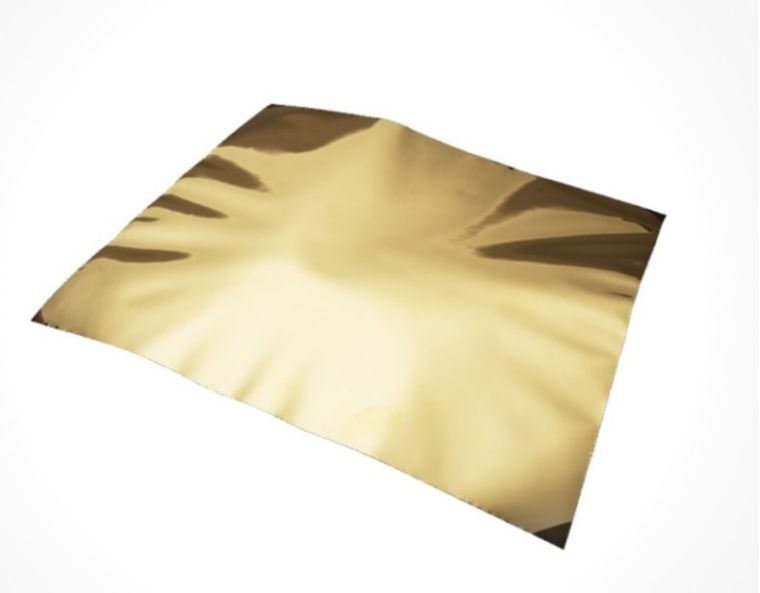

***Figure 3.4.*** *Polarized PVDF film with a thickness of 52* $\mu m$

As specified in Chapter 2, a layer capable of absorbing acoustic waves must be placed adjacent to the bottom surface of the piezoelectric sensor. The pressure waves generated by the interaction between space charge and pulsed voltage can be assimilated to plane waves, therefore, the acoustic impedance of a medium can be calculated by the following expression of the characteristic acoustic impedance:

$$Z = \rho_m v \tag{3.8}$$

Where $\rho_m$ is the mass density and $v$ is the sound speed through the medium. In Table 3.2, the acoustic characteristics of the mediums crossed by the pressure waves in the PEA cell described in this document are listed.

With reference to Figure 3.2, let consider a *P* wave reaching the upper surface of the piezoelectric sensor between $S_1$ and $S_2$. As shown in Figure 3.5, once the interface between the ground electrode and the sensor is reached, P can be divided in 4 main pressure waves

covering different paths. A first part of the original wave, $P_0$, crosses both the planar surfaces of the sensor and it is dissipated outside the PEA cell after passing the interface between the absorber and the aluminum case. The amplitude of $P_0$ can be estimated as follows:

$$P_0 = \frac{2Z_{al}}{Z_{al}+Z_P} \cdot \frac{2Z_P}{Z_P+Z_{ab}} \cdot \frac{2Z_{ab}}{Z_{ab}+Z_{al}} \cdot P \tag{3.9}$$

Where $Z_P$, $Z_{al}$ and $Z_{ab}$ are the acoustic impedance of the piezoelectric film, the aluminum layers and absorber respectively.

A second part of the original wave, $P_1$, crosses both the planar surfaces of the sensor and it is reflected at the interface between the absorber and the aluminum case of the cell. The amplitude of $P_1$ can be estimated as follows:

$$P_1 = \frac{2Z_{al}}{Z_{al}+Z_P} \cdot \frac{2Z_P}{Z_P+Z_{ab}} \cdot \frac{Z_{al}-Z_{ab}}{Z_{ab}+Z_{al}} \cdot P \tag{3.9}$$

The wave $P_1$ is, after having crossed the piezoelectric membrane, come back to the sensor after a time $t(P_1)$ which can be calculated as follows:

$$t(P_1) = \frac{2d_{ab}}{v_{ab}} \tag{3.10}$$

Where $d_{ab}$ and $v_{ab}$ are the thickness and sound speed of the PMMA absorber. In order to avoid the arrival of the wave $P_1$ between the two main peaks, the following condition has to be satisfied:

$$t(P_1) > t(S_2) \Longrightarrow d_{ab} > \frac{v_{ab}}{2}\left(\frac{d_{sa}}{v_{sa}} + \frac{d_{sc}}{v_{sc}} + \frac{d_{al}}{v_{al}}\right) \tag{3.11}$$

From condition (3.11), considering the aforementioned the dimensions specified above, it follows that the PMMA absorber should be thicker than 8 mm. In order to limit reflections at the interface between the sensor and the absorber, the latter must have an acoustic impedance as close as possible to that of the PVDF. Therefore, using a non-polarized PVDF layer would be the best choice. Unfortunately, it is not easy to find non-polarized PVDF layers on the market with a thickness compatible with the needs of the PEA cell whose design is described in this thesis. For this reason, a 17 mm thick layer of PMMA like the one shown in the Figure 3.6 has been chosen.

In Table 3.3, the results of the calculation described in this section are summarized.

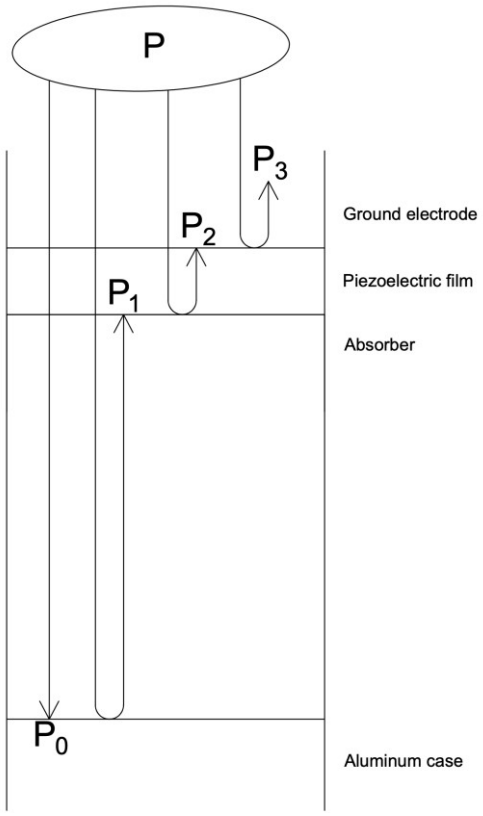


***Figure 3.5.*** *Reflections of pressure waves at the sensor surfaces*

***TABLE 3.2.*** *Acoustic characteristics of the mediums crossed by the pressure waves in the PEA cell*

| | **Sound speed** | **Mass density** | **Characteristic acoustic impedance** |
|---|---|---|---|
| **Material\Parameter** | $v$ [m/s] | $\rho_m$ [kg/m$^3$] | Z [$10^6$ * Pa*s/m] |
| **Sample (polymeric dielectric materials)** | ~2200 | ~900 | ~1.98 |
| **Ground electrode and cell case (Aluminum)** | 6400 | 2700 | 17.28 |
| **Piezoelectric sensor (PVDF)** | 2600 | 1780 | 4.63 |
| **Absorber (PMMA)** | 2760 | 1430 | 3.95 |
| **Epoxy resin** | ~2650 | ~1200 | 3.18 |

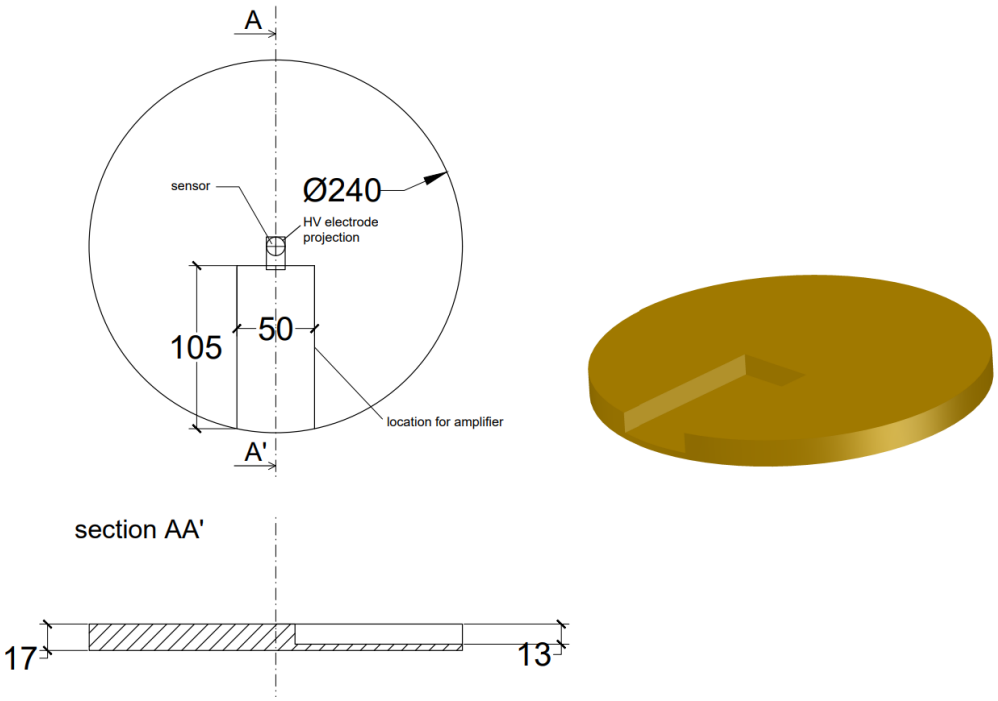


***Figure 3.6.*** *PMMA disk (units in mm)*

***TABLE 3.3.*** *Requirements for thickness and materials of components disposed along the path of the acoustic waves*

| | **Thickness [m]** | **Diameter [m]** | **Material** |
|---|---|---|---|
| **Piezoelectric sensor** | $5.2 \cdot 10^{-5}$ | $1.2 \cdot 10^{-2}$ | PVDF |
| **Absorber** | $1.7 \cdot 10^{-2}$ | $2.4 \cdot 10^{-1}$ | PMMA |
| **Ground electrode** | $2.0 \cdot 10^{-2}$ | $2.4 \cdot 10^{-1}$ | Aluminum |

## 3.2 High voltage electrode

The role of the high voltage electrode in the PEA cell is to apply a DC voltage between the upper surface of the dielectric flat specimen under test and the lower surface connected to ground. The contact between the HV electrode and the sample can be direct or through a semiconductive layer having a maximum thickness of 1 mm. The HV electrode must be designed considering its insulation from the aluminum housing and the ground electrode, as well as the need to minimize corona Partial Discharges (PD) which could affect the output signals. In Figure 3.7, the drawings of the designed HV electrode are shown. As it can be seen, at the top of the aluminum electrode, two cylindrical holes have been made for the connection of the HVDC and pulsed voltage sources.

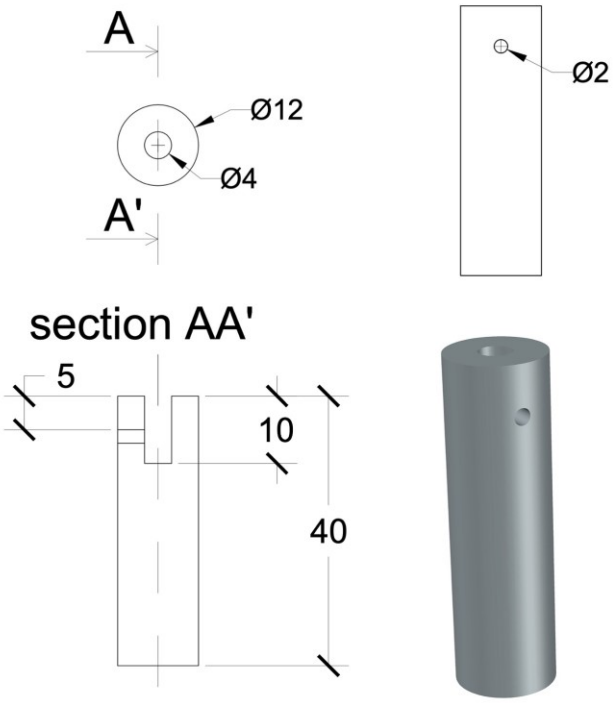


***Figure 3.7.*** *High Voltage electrode (units in mm)*

As can be observed, the two holes are perpendicular to each other in order to distance the output terminal of the HVDC source from that of the pulse generator as much as possible. As will be described in detail in the following sections, the high voltage electrode is inserted in a PTFE body inside which two capacitors are encapsulated for coupling with the pulse generator and the coil of the heat exchanger. In order to guarantee the integrity of the cell, it is necessary to avoid the possibility that an electric discharge could cover the path between the high voltage electrode and the ground electrode. For this purpose, the simplified axisymmetric model reported in Figure 3.8 has been built.

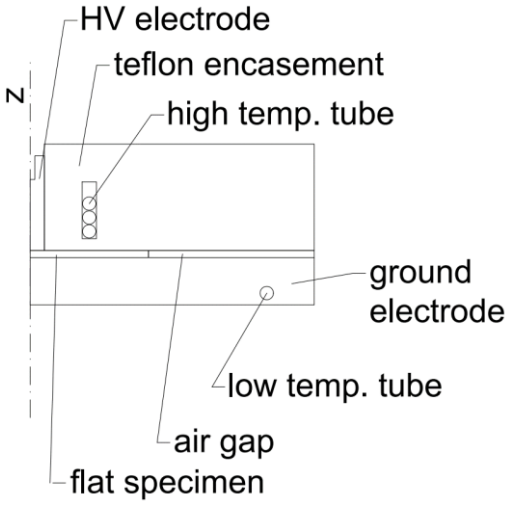


***Figure 3.8.*** *Schematic axial-symmetric section of the PEA cell*

This model has been used to evaluate the maximum electric field reached in the air gap during two different scenarios. In order to obtain the maximum electric field values reached in the air gap, a coupled thermal and electrical model in time domain has been developed in a FEM software. The thermal model is based on the conductivity in solids and a convective heat exchange with a coefficient of 4 $W/m^2K$ is considered at the external surfaces. This coefficient is compatible with a heat exchange in the still air of a laboratory. The calculation of electric field and space charge within the PEA cell is based on a conductivity and current continuity model. In the case studio, an XLPE flat specimen with a thickness of 3 mm and a diameter of 100 mm has been considered. Moreover, the dependency on temperature and electric field of the electrical conductivity of the insulation is described by the following [18]:

$$\sigma = A \cdot exp\left(\frac{-\varphi q}{k_b T}\right) \cdot \frac{\sinh\left(B|E|\right)}{|E|} \tag{3.12}$$

where A, φ and B are respectively a material depending parameter, the thermal activation energy and the field constant, q is the elementary charge, kb is the Boltzmann's constant and |E| is the magnitude of the electric field. The parameters used for this case study are the following [18]:

A = 8.15E6 V/(Ohm*m2)

φ = 0.78 eV

B = 1.40E-7 m/V.

For each scenario, three different phases are considered as follows:

Phase 1. From 0 to 120 kV (120% of the rated value) in 10 s;

Phase 2. 120 kV for 3600 s;

Phase 3. From 120 kV to 125 kV in 10 ns (rising ramp of the first pulse).

During the first scenario, the inlet temperature of the upper heat exchanger tube is set at 80 °C and the lower one is at 20 °C. In the second scenario, the entire PEA cell is kept at 20 °C. The main results of the simulations are shown in Figures 3.9-3.11 and in Table 3.4. During the first phase of the simulated transient, the maximum electric field is reached at the end of the voltage ramp. As it can be observed in Figure 3.9, at the end of the first phase, in both scenarios, a maximum electric field of 0.75 kV/mm is reached in the air gap in proximity of the flat sample outer surface. After only 10 s, the temperature profile in the

areas of the air gap and sample are the same, therefore no differences are expected in terms of electric field. As it can be observed in Figure 3.10 a, under homogeneous temperature profile, the electric field distribution in the air gap at the end of the Phase 2 is very close to that at the end of the Phase 1. A slight deformation of the electric field profile at the end of the one-hour transient occurs due to the dependence of the electrical conductivity of the sample on the electric field. As shown in Figure 3.10 b, the maximum electric field reached in the air cavity decreases with time when the upper part of the PEA cell is heated up. This can be attributed to the higher conductivity of the polymeric specimen at higher temperature. Under these conditions, the maximum electric field reached at the end of the Phase 2 is equal to 0.34 kV/mm.

In Figure 3.11, the electric field distribution at the end of the Phase 3 is shown. As it can be observed, the electric field reaches the peak value of 0.62 kV/mm if the PEA cell is kept at 20 °C whilst its maximum is equal to 0.11 kV/mm under temperature gradient. In Table 3.4, the main results of the above described simulations are reported.

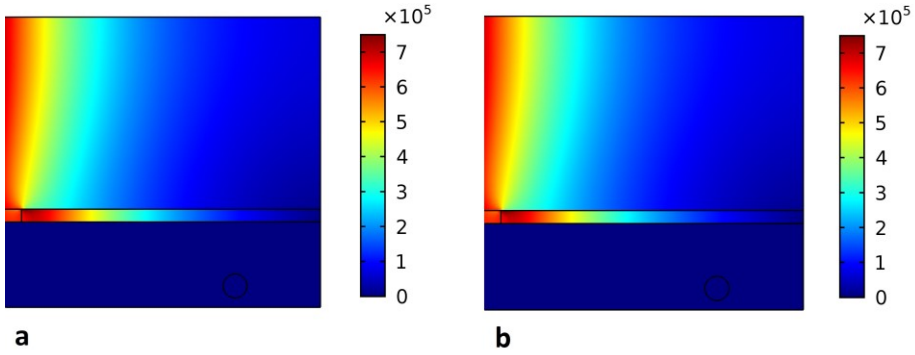


***Figure 3.9.*** *Electric field in the air gap of the PEA cell at the end of the Phase 1 (units in V/m) – a) the entire cell is at 20 °C; b) the inlet of the upper heat exchanger is kept at 80 °C and the lower one is at 20 °C*

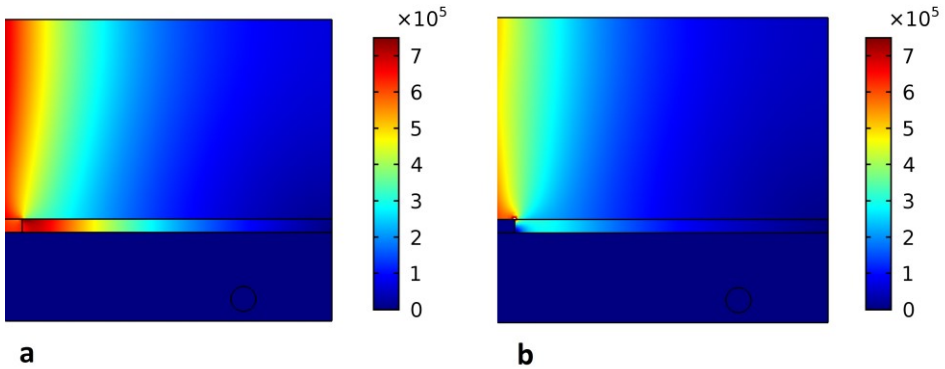


***Figure 3.10.*** *Electric field in the air gap of the PEA cell at the end of the Phase 2 (units in V/m) – a) the entire cell is at 20 °C; b) the inlet of the upper heat exchanger is kept at 80 °C and the lower one is at 20 °C*

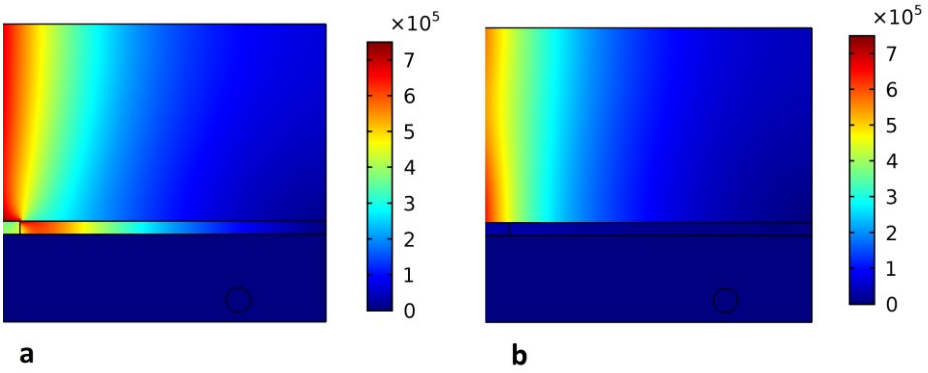


***Figure 3.11.*** *Electric field in the air gap of the PEA cell at the end of the Phase 3 (units in V/m) – a) the entire cell is at 20 °C; b) the inlet of the upper heat exchanger is kept at 80 °C and the lower one is at 20 °C*

***TABLE 3.4.*** *Maximum electric fields – results of simulations*

| | **Voltage [kV]** | **duration [s]** | **max. Electric field [kV/mm]** | |
|---|---|---|---|---|
| | | | homogeneous temperature | application of temperature difference |
| **Phase 1** | 0-120 | 10 | 0.75 | 0.75 |
| **Phase 2** | 120 | 3600 | 0.72 | 0.34 |
| **Phase 3** | 120-125 | 1E-8 | 0.62 | 0.11 |

From the results of the simulations listed in Table 3.4, it can be concluded that the maximum electric field reachable in the air gap of the PEA cell is lower than 1 kV/mm, therefore the occurrence of discharges during the operation of the system can be excluded.

In order to avoid corona discharge at the connection between the HVDC source output and the PEA cell, a pool has been prepared at the top of the PTFE encasement of the HV electrode. This pool shall be filled with mineral oil as shown in Figure 3.12.

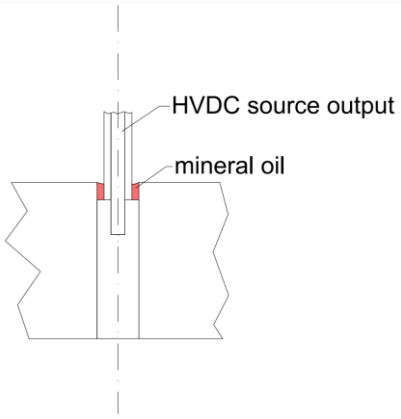


***Figure 3.12.*** *Mineral oil pool at the top of the HV electrode*

As shown in Figure 3.13, the DC High Voltage is applied by reversable polarity, 100 kV Glassman KT100R20 HVDC supplier. This type of HVDC generator can be supplied with 230 V RMS, single phase, 50 Hz. Thanks to this HVDC supplier, it is possible to apply both negative and positive voltages to the dielectric sample up to the limit value of 100 kV with a maximum current of 20 mA. In order to protect the HVDC supplier against a possible breakdown of the PEA cell, the 10 MΩ resistance *R* has been connected as shown in Figure 3.13. With this purpose, a 110 W resistor of the series 500.100 of Nicrom Electronic has been selected. The coupling capacitor C, which will be evaluated in the next paragraph, is instead interposed between the pulse generator and the HVDC supplier.

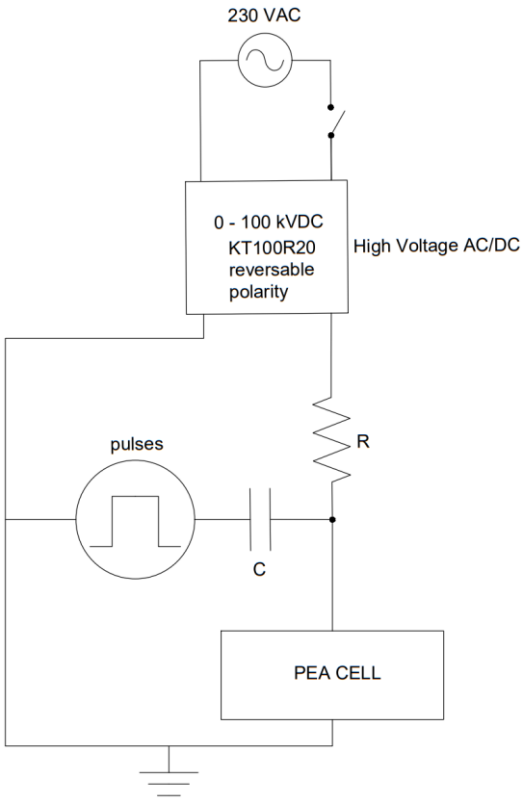


***Figure 3.13.*** *Schematic of the reversable polarity HV application to the PEA setup*

## 3.3 Pulse generator

As mentioned in Section 3.1, a pulse generator with a pulse width lower than 120 ns must be designed with the aim to obtain space charge measurements with a spatial resolution compatible with the requirements listed in Table 3.1. With this purpose, the pulse generator shown in Figure 3.14 has been designed. In order to correctly determine the pulse generator components, the main circuit has been modeled in Simulink® according to the

scheme shown in Figure 3.15. In this schematic, the operating mode with positive HVDC supply is considered. The model shown in Figure 3.15 has been used to perform simulations in time domain with a time step equal to 1 ns. The duration of the simulated transients has been set considering the time necessary to reach a steady state. This time resulted equal to 50 ms. The DC High Voltage sources are supplied from two 8 kV Glassman 300 W regulated module. The positive and negative voltages are supplied from a MQ8P37 and a MQ8N37 respectively. This type of HVDC generator can be supplied with 230 V RMS, single phase, 50 Hz. The selection between application of positive or negative voltage is made by means of two diverters controlled by the same signal. As explained in the previous chapters, due to the phenomenon of space charge accumulation, the polarity reversal is one of the events that have the greatest probability of causing a fault in the insulation of an HVDC cable connected to a Current Source Converter (CSC). For this reason, a PEA system has been designed capable of reversing the polarity of the voltage applied to a relatively thick flat dielectric sample. One of the main objectives of this project is indeed to create a test setup capable of replicating as faithfully as possible the space charge accumulation phenomena that occur in the dielectric layer of an operating cable.

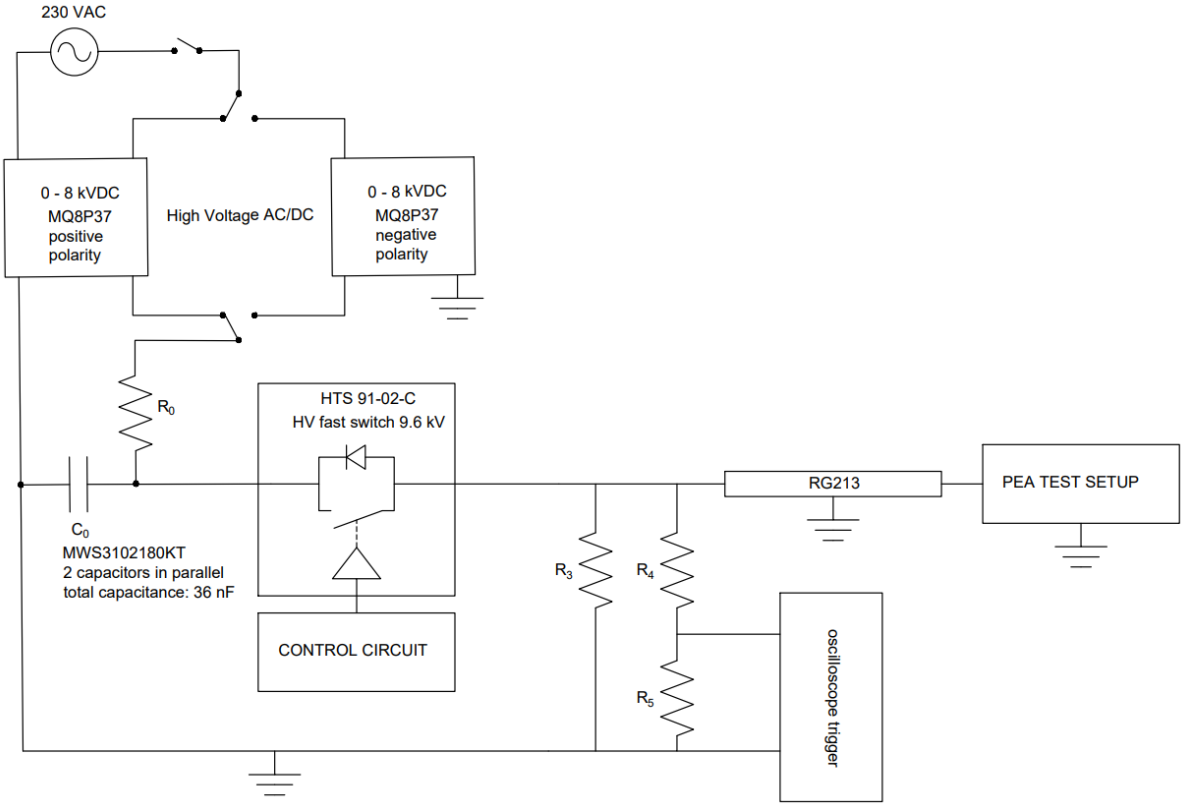


***Figure 3.14.*** *Schematic of the pulse generator*

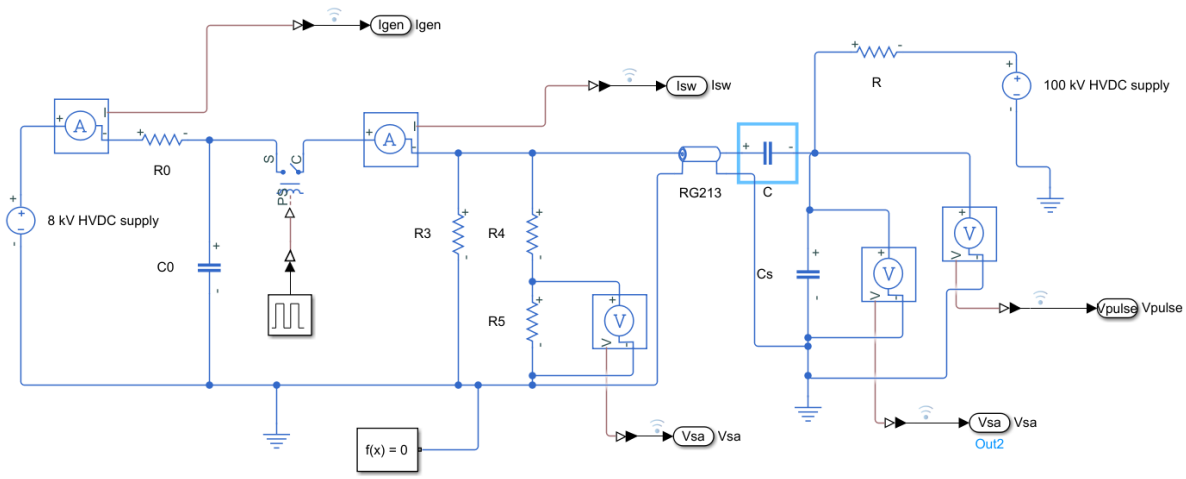


***Figure 3.15.*** *Schematic of the pulse generator model implemented in Simulink®*

As can be seen from the Figure 3.14, the capacitor $C_0$ is charged by one of the two 8 kV HVDC generators by means of the current flowing through $R_0$. The values of $R_0$ and $C_0$, are optimized in order not to exceed the maximum current of 37 mA of the generator and, at the same time, to load $C_0$ in the waiting time between two successive pulses.

In order to protect the 8 kV HVDC supplier against a possible breakdown of the pulse generator, a 250 kΩ, 23 W resistor of the series MS500.10 of Nicrom Electronic has been selected. Moreover, as shown in Figure 3.14, the capacitance $C_0$ consists of two 18 nF MWS3102180KT capacitors connected in parallel. In figure 3.16, the time trend of the current crossing R0, obtained from the simulations, is plotted. As can be observed, the maximum current is equal to 32 mA at the switch-on of the generator and, therefore, the limit value of 37 mA is not exceeded.

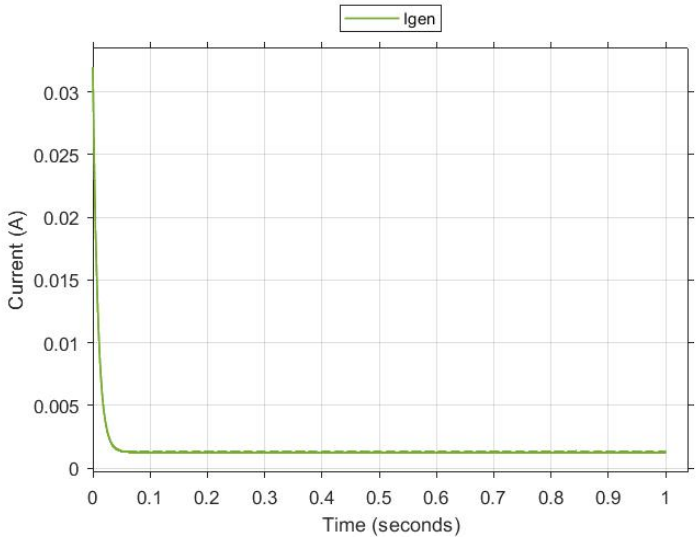


***Figure 3.16.*** *Output current of the 8 kV HVDC supplier for the pulse generator*

The discharge of the capacitor C0 occurs through the fast high voltage transistor switch BEHLKE HTS 91-02-C. This HV switch has a controlled variable on-time with a minimum value of 50 ns. A control circuit for the fast switch has been designed with the goal of meeting the set goals for the pulse generator. This circuit is described below and consists of a fast timer in astable configuration generating pulses with a width of 66 ns. The main characteristics of the selected HV switch are the following:

- Max operating voltage: 9.6 kV;
- Max power dissipation: 10 W (standard device, forced air at 4 m/s);
- Typical turn-on resistance, $R_{stat}$: 72 Ω;
- Typical turn-on rise time: 23 ns (@ expected operating conditions);
- Typical turn-off rise time: < 10 ns;
- Minimum pulse width: 50 ns;
- Control voltage range: 2-6 V;
- Aux voltage supply: 4.5-5.5 V.

The main power losses in the HV switch are due to the load current flowing through the internal resistance $R_{stat}$. These losses must be kept below the maximum power dissipation of the device $P_{d(max)}$. As shown in Figure 3.17, the maximum load current $I_L$ resulting from the simulations is equal to 17 A, therefore, the average power losses in the HV switch can be cautiously calculated, considering the duty cycle $\Delta_{ep}/T$, as follows:

$$P_d = \frac{R_{stat} \cdot I_L^2 \cdot \Delta_{ep}}{T} = 0.25\ W \tag{3.13}$$

Where $\Delta_{ep}$ is the maximum pulse width equal to 120 ns and $T$ is the period between two pulses set to 10 ms (100 Hz). As can be seen, the power losses are abundantly below the limit value of 10 W.

With references to the Figures 3.14 and 3.15, the resistance $R_3$ equal to 500 Ω is used as resistive load for the discharge. The resistances $R_4$ and $R_5$ are used as voltage divider for the oscilloscope trigger and the selected values are 10 MΩ and 10 kΩ respectively.

With reference to the Figure 3.1, the pulsed voltage applied to the sample $V_{sa}$ depends on the amplitude of the pulse at the terminals of $V_{pulse}$ the capacitances of the dielectric specimen $C_{sa}$ and the coupling capacitor $C$ as follows:

$$V_{sa} = \frac{C}{C + C_{sa}} \cdot V_{pulse} \tag{3.14}$$

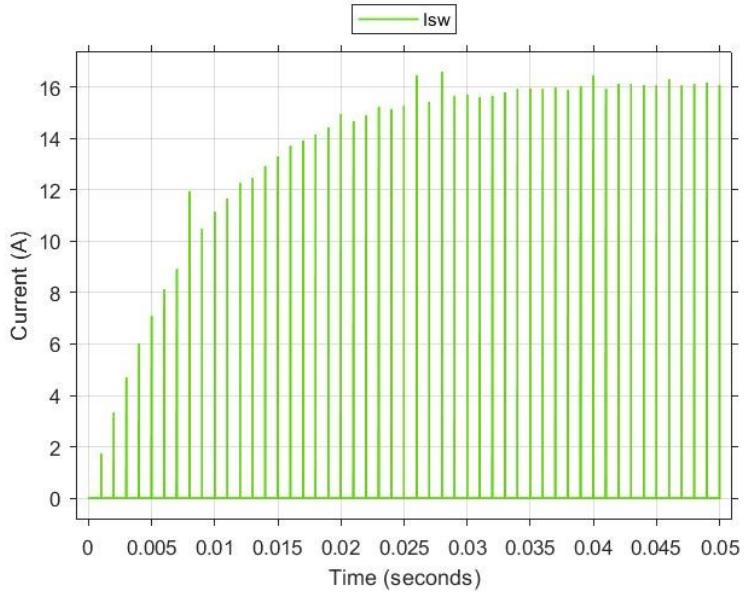


***Figure 3.17.*** *HV switch current*

From the equation (3.13) follows that, in order to obtain $V_{sa}$ as close as possible to $V_{pulse}$, should be $C >> C_{sa}$. From the sample dimensional range described in Table 3.1, it follows that $C_{sa}$ has a capacitance value between 2.6 pF and 8.0 pF, therefore, a 100 pF coupling capacitor has been chosen. The capacitor $C_{sa}$ is formed with two TDK 60712ZT201K4HDA connected in series with a capacitance of 200 pF and a rated voltage of 50 kV. These cylindrical Ultra High Voltage Ceramic Capacitors have a diameter of 30.00 mm ±1.00 mm and a length of 35.00 mm ±1.00 mm.

With references to the Figures 3.14 and 3.15, the length of the RG 213 coaxial cable plays a very important role in the quality of the pulse applied to the sample. The Velocity Factor of a RG 213 coaxial cable is equal to 66%, therefore, a delay of 5 ns is introduced for each meter of the output line of the pulse generator. The pulse generated reflects once arrived to the sample and reflects again when reaches the resistor $R_3$, therefore, the signals returns to the sample with an amplitude depending on the impedances mismatch.

One of the most used strategies is to use a coaxial cable of sufficient length to make the first reflected pulse arrive in a time greater than that which elapses between the arrival at the piezoelectric of the two peaks relating to the charge accumulated at the interfaces between the dielectric and the electrodes. In this case study, the time required for the acoustic waves to pass through a dielectric thickness of 5 mm is approximately 2.5 µs. This time should be less than the time it takes for the pulse to travel twice the length of the coaxial cable. To make this possible, it would be necessary to use an RG213 cable with a

length of approximately 300 m. This choice would in any case cause problems of attenuation and distortion of the signal, altering the reliability of the final signal arriving at the piezoelectric sensor.

Another strategy is to use the shortest possible pulse generator output cable. In this case, the reflexed impulses reach the PEA system before the original impulse is finished. This causes an increase in the duration of the impulse compared to that generated by the closing and opening of the HV switch. In the pulse generator design described in this thesis, the second of these two strategies has been found to be the most appropriate for the needs of the application.

With the above described components, listed in Table 3.5, the designed apparatus generates the voltage pulse applied to the sample shown in Figure 3.18. As it can be observed, the half-amplitude width of the generated pulse is equal to 112 ns, less than the target value of 120 ns. It follows that, in case of samples with a thickness of 3 mm, the spatial resolution due to the pulse width will be, therefore, equal to 7.4%. In the case of 5 mm thickened specimens, the spatial resolution results equal to 4.5%.

As it can be observed from the Figure 3.18, the amplitude of the voltage pulse applied to the sample is equal to 6.7 kV, equal to about 84% of the HVDC generator output voltage.

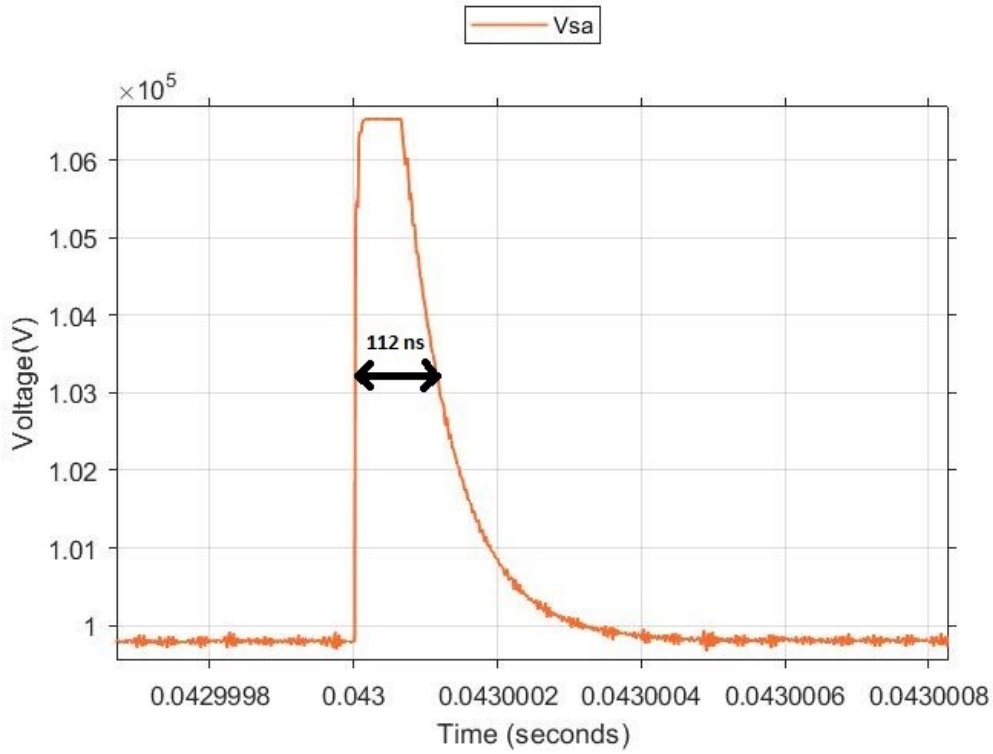


***Figure 3.18.*** *Voltage applied to the sample over time*

***TABLE 3.5.*** *Main components of the pulse generator*

| **Component** | **main characteristics** |
|---|---|
| **8 kV HVDC source** | *max operating voltage equal to 8 kV, max current higher than 32 mA, positive end negative polarity for polarity reversal procedures.* |
| **R0** | 250 kΩ, non-inductive mass resistor, max operating voltage > 10 kV |
| **C0** | *36 nF,* max operating voltage > 10 kV |
| **HV switch** | minimum pulse width < 60 ns, max operating voltage > 8 kV, maximum peak current > 20 A, maximum continuous load power > 5 W, maximum turn-on and turn-off rise time < 25 ns. |
| **$R_3$** | 500 Ω, non-inductive mass resistor, maximum continuous load power > 25 W, max operating voltage > 10 kV. |
| **$R_4$** | 10 MΩ, non-inductive mass resistor, maximum continuous load power > 10 W, max operating voltage > 10 kV. |
| **$R_5$** | 10 kΩ, non-inductive mass resistor. |
| **RG213** | max length equal to 0.4 m, impedance equal to 50 Ω |
| **C** | 100 pF |

As mentioned before, the HV switch is controlled by means of a timer circuit based on the use of a LTC6991 in astable configuration, as shown in Figure 3.19. The LTC6991 is a silicon oscillator with a programmable period range of 1.024ms to 9.54 hours (29.1µHz to 977Hz), specifically intended for long duration timing events. A single resistor, $R_{SET}$, programs the LTC6991 internal master oscillator frequency. The output clock period is determined by this master oscillator and an internal frequency divider, $N_{DIV}$, programmable to eight settings from 1 to $2^{21}$ as follows:

$$t_{OUT} = \frac{N_{DIV} \cdot R_{SET}}{50k\Omega} \cdot 1.024\text{ms} \tag{3.15}$$

The selected oscillator can be supplied with a DC voltage up to 6 V and it is characterized by output rise and fall time equal to approximately 1 ns. As shown in Figure 3.20, the astable configuration of the oscillator has been optimized by means of a software provided from the manufacturer of the device. The value of $N_{DIV}$ equal to 8 has been set by using resistances $R_1$ and $R_2$ equal to 976 kΩ and 102 kΩ respectively. Considering the

aforementioned target frequency of 100 Hz, a $R_{SET}$ equal to 60.4 kΩ has been chosen. The output pulse width $t_{PULSE}$ of the oscillator is equal to the product of the resistance $R_{PW}$ and the capacitance $C_{PW}$. In order to obtain an input pulse width to the HV fast switch, the values of 10.7 kΩ and 6.6 pF have been chosen for $R_{PW}$ and $C_{PW}$ respectively.

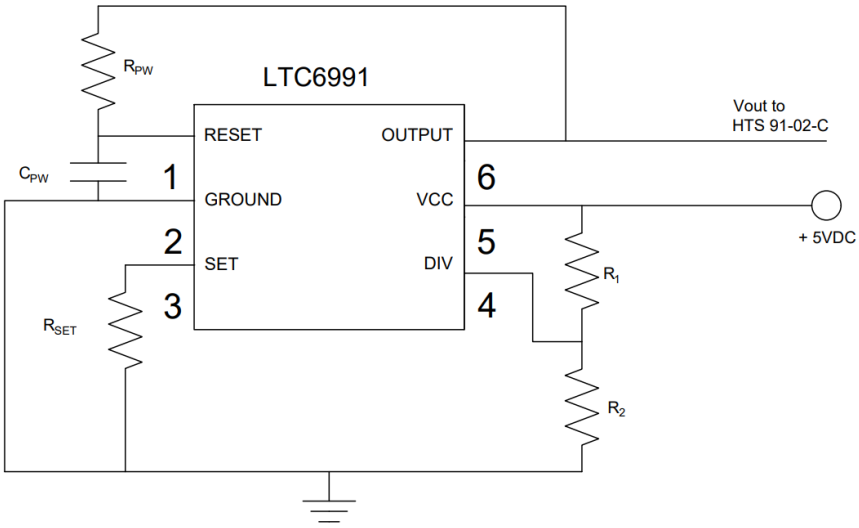


***Figure 3.19.*** *Control circuit for the HV switch*

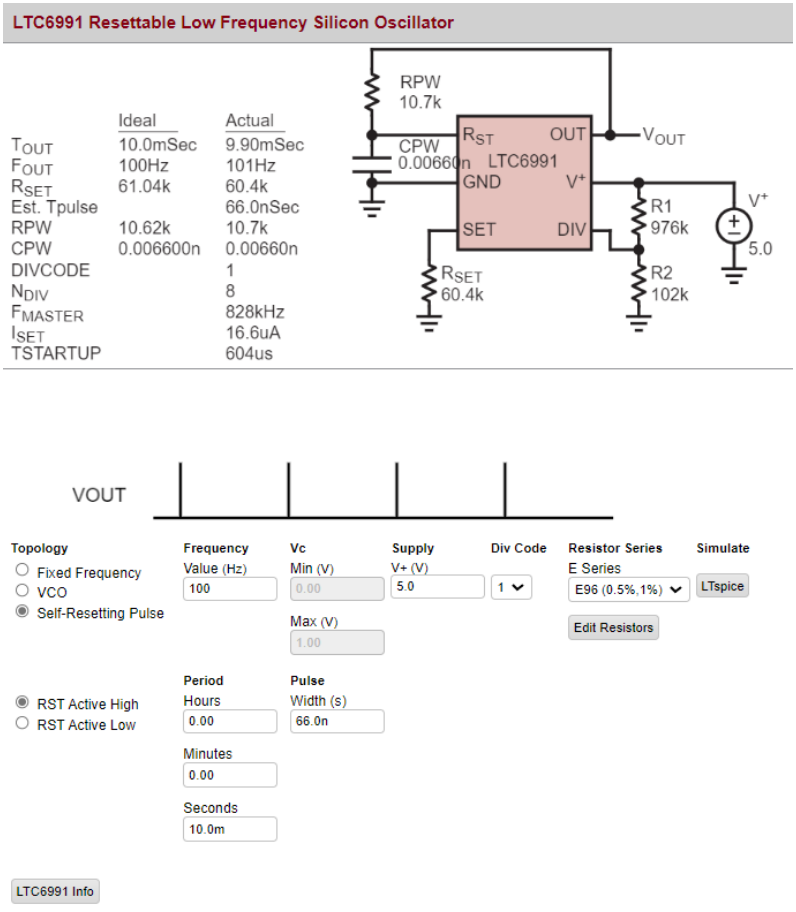


***Figure 3.20.*** *Configuration of the LTC6991 oscillator*

## 3.4 Signal amplification

The output signal of a PVDF piezoelectric transducer is typically lower than 100 μV. Therefore, a signal amplifier is needed to improve the signal to noise ratio of the system. Amplification of ca. 40 dB is sufficient for good signal acquisition. The measurement also contains very wide spectrum of frequencies, and to attain high enough accuracy, the amplifier should have as large a bandwidth as possible. High bandwidth also reduces the low-pass filtering effect of the amplifier circuit, giving better measurement resolution. Among commercial wideband signal amplifiers, a broadband low noise amplifier PE15A63012 by Pasternack has been selected. This amplifier has a frequency range between 1 kHz and 1 GHz and its rated power gain is equal to 40 dB. To minimise EMI issues originating from external radiation sources, the amplifier was placed inside an aluminium shielding case together with the piezoelectric signal detector.

## 3.5 Temperature control

In order to apply a temperature gradient to the dielectric sample, two heat exchangers have been designed. In Figure 3.21, a schematic of the thermal system designed for the PEA apparatus is shown. The thermal energy is brought to the upper part of the PEA cell by a silicone rubber coil inside which flows mineral oil which is heated by an electric resistance and moved by a pump. In order to cool the lower surface of the flat sample and to protect the piezoelectric sensor, sensitive to high temperatures, an additional heat exchanger is installed in the ground electrode. This exchanger consists of a single coil of silicone rubber tube inside which flows mineral oil moved by a pump and exchanged with the external environment by means of a radiator. Silicone rubber has a low thermal conductivity and is therefore not very suitable for making tubes for heat exchangers. However, in this case, the coil of the heat exchanger must be close to the high voltage electrode, so a dielectric material must be used. In order to preserve the ground electrode cooling system pump, also the low temperature heat exchanger tube made of silicone rubber. As can be seen from Figure 3.21, the inlet temperature of the upper coil is controlled in order to avoid exceeding the limit value of 80 °C and therefore damaging the components of the heating system. This temperature is controlled by an optical fiber sensor acquired by a control system capable of switching off the *P1* pump if the limit value is exceeded. Similarly, a PT100 type sensor controls the temperature inside the tank where the heating

resistance is present in order to avoid exceeding the limit value of 85 ° C. This control acts by disconnecting the resistor if the maximum temperature is exceeded. Both the controls described above are based on a hysteresis of 5 ° C in order to avoid too frequent switches. The heat exchange between the heater, the cooler and the PEA cell can be schematized as in Figure 3.22. The thermal power *Q1* enter in the PEA cell system, drawn as a rectangle, by means of the heat exchange between the high temperature mineral oil and TPFE encasement of the HV electrode. *Q1* can be calculated as the enthalpy difference between inlet and outlet fluid using the following equation:

$$Q1 = \dot{m}_{oil,h} C_{p,eff} \left( T_{in,h} - T_{out,h} \right) \tag{3.16}$$

Where $\dot{m}_{oil,h}$ is the oil mass flow rate, $C_{p,eff}$ is the specific heat at constant pressure and $T_{in,h}$ as well as $T_{out,h}$ are the inlet and the outlet temperature respectively. All the parameters described above refer to the high temperature side.

Similarly, also the thermal power Q2 can be calculated by means of the following equation:

$$Q2 = \dot{m}_{oil,l} C_{p,eff} \left( T_{out,l} - T_{in,l} \right) \tag{3.17}$$

Where $\dot{m}_{oil,l}$ is the oil mass flow rate and $T_{in,l}$ as well as $T_{out,l}$ are the inlet and the outlet temperature respectively. All the parameters described above refer to the low temperature side. The thermal power released towards the outside *Qext* depends on the temperature distribution on the external surface of the PEA cell.

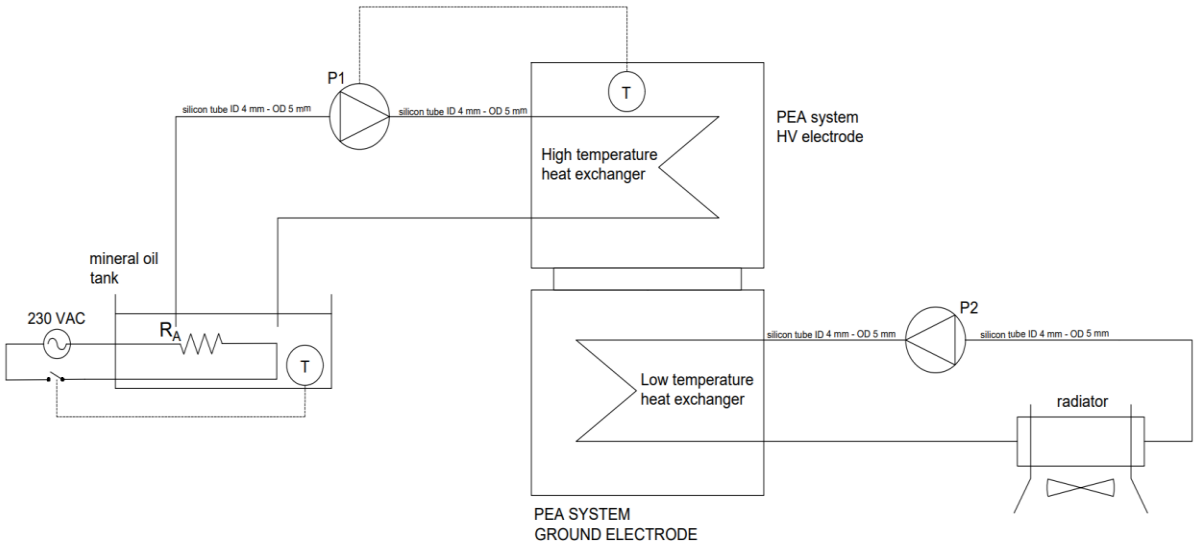


***Figure 3.21.*** *Thermal system for the application of a temperature drop*

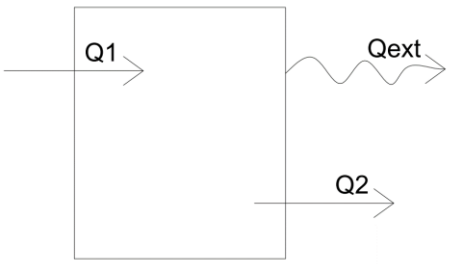


***Figure 3.22.*** *Schematic of the heat exchange between the heater, the cooler and the PEA cell*

In order to calculate the parameters of the two heat exchangers in such a way as to obtain a temperature difference of at least 20 ° C between the surfaces of a 3 mm thick dielectric sample, a thermal analysis has been carried out with an FEM software in the time domain. The duration of the simulated transient is 2 hours. The thermal model used is based on the Fourier equation for conduction in solids. The outgoing thermal power *Qext* is calculated considering a convective heat exchange between the PEA cell and still air. This replicates the conditions of an indoor laboratory. Moreover, the following boundary conditions have been considered:

- Environmental temperature: 20 °C;
- Convective heat exchange coefficient (still air): 4 W/(m$^2$*K);
- Oil inlet temperature (high temperature side): 80 °C;
- Oil outlet temperature (high temperature side): 60 °C;
- Oil inlet temperature (low temperature side): 20 °C;
- Oil mass flow rate (low temperature side): 10 ml/min;
- $C_{p,eff}$: 1870 J/(kg*K);
- Oil mass density, $\rho_m$: 895 kg/m$^3$ (Transformer oil 10, Green Star)

The main results of the simulation are listed below:

- *Q1* = 8.72 W;
- *Q2* = 6.97 W;
- *Qext* = 0.84 W;
- $\dot{m}_{oil,h}$ = 2.7*10$^{-4}$ kg/s (equal to a volumetric flow rate of 18 ml/min.

As can be observed from the results of the simulation, the incoming power *Q1* is greater than the sum of the outgoing powers *Q2* and *Qext*. This is due to the fact that, as can be seen from the Figure 3.23, a thermal equilibrium has not yet been reached after two hours.

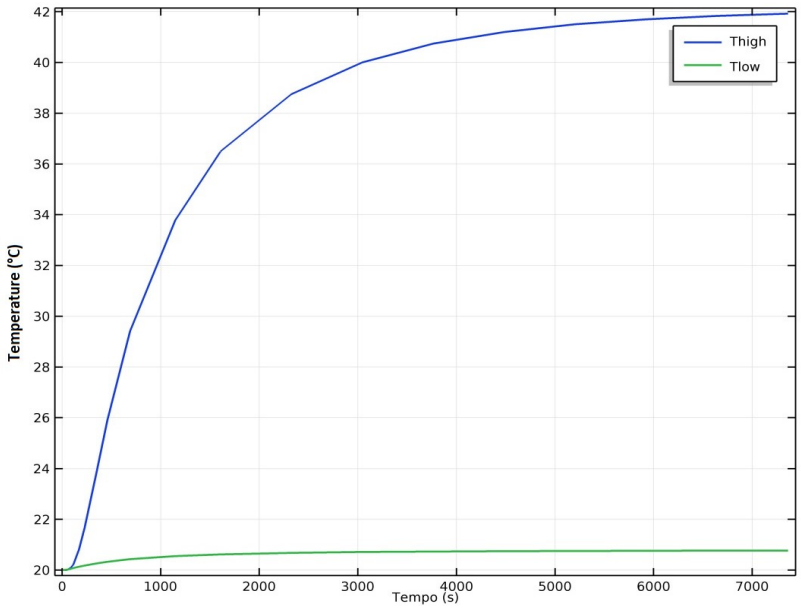


***Figure 3.23.*** *Time trend of the temperatures at the upper and lower surfaces of a 3 mm thick sample*

In any case, starting from the conditions specified above, the calculations show that a volumetric flow rate of about 20 ml/min is sufficient to obtain a temperature difference of 20 °C between the surfaces of a 3 mm thick dielectric. Such low flow rates can be obtained by means of peristaltic pumps typically used for medical applications. Figure 3.24 shows a 3D view of the temperature distribution inside the PEA cell at the end of the simulated transient lasting 2 hours.

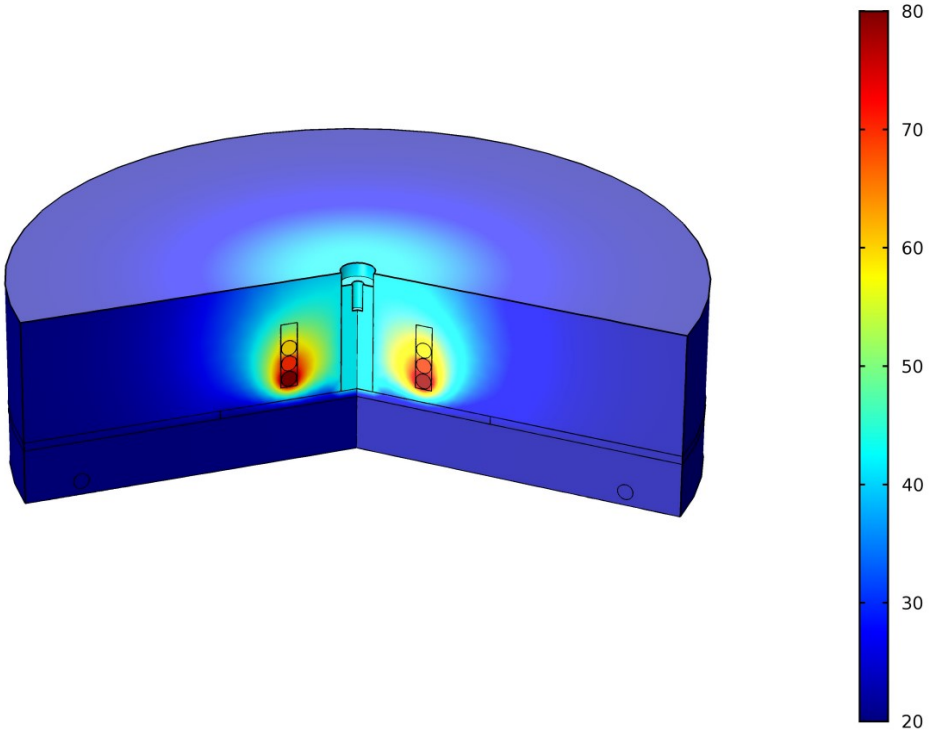


***Figure 3.24.*** *Temperature distribution inside the PEA cell*

In Figure 3.25, the high-temperature exchanger tube is shown. This has an internal diameter *Din* of 4 mm and an external diameter *Dout* of 5 mm, takes place on 3 coils and has an overall length $L$ of 0.47 m. Since the cross area results equal to 12.6 mm$^2$, the oil circulation speed $u_h$ will be equal to 26 mm/s. The Reynolds number of the oil flowing in the high temperature coil can be calculated by means of the following equation:

$$Re = \frac{u_h Din}{\eta_c} \tag{3.18}$$

Where $\eta_c$ is the viscosity of the mineral oil, considered equal to 12 mm$^2$/s. The Reynolds number results equal to 8.67, therefore, the motion of the oil can be considered as laminar. The pressure drop over the high temperature circuit can be calculated by means of the following equation [80]:

$$\Delta P = \frac{f_D L_{TOT}}{Din} \frac{\rho_m {u_h}^2}{2} \tag{3.19}$$

Where $L_{TOT}$ is the total length of the circuit and $f_D$ is the Darcy friction factor. The total length is equal to the sum of the length of the exchanging portion of the coil and twice the distance between the PEA cell and the tank. For laminar flow, the Darcy friction factor can be calculated as follows [80]:

$$f_d = \frac{64}{Re} \tag{3.20}$$

Considering $L_{TOT}$ = 2.5 m, it follows that $\Delta P$ = 1396 Pa. The pump power $W_P$ can be calculated by means of the following equation [80]:

$$W_P = \frac{1}{\eta} \Delta P \frac{\dot{m}_{oil,h}}{\rho_m} \tag{3.21}$$

Where $\eta$ is the net efficiency of the pump. Conservatively considering a pump efficiency equal to 50%, the necessary power would be equal to 0.83 mW. For this specific application, a Verderflex® M025DC peristaltic pump was chosen. According to the datasheet, this pump has an input power of 6 VA, a maximum flow rate of 18.5 ml / min with an internal diameter of the tube of 3.2 mm and a rotation speed of 30 rpm. This pump is therefore suitable for circulating the oil through the heating circuit of the upper part of the PEA cell.

The length of the low temperature circuit encapsulated in the ground electrode differs by only 150 mm from the upper one. As the pressure drops are practically identical, it is possible to use the same type of pump for both the heating and cooling circuits. In Figure 3.26, the low-temperature exchanger tube is shown.

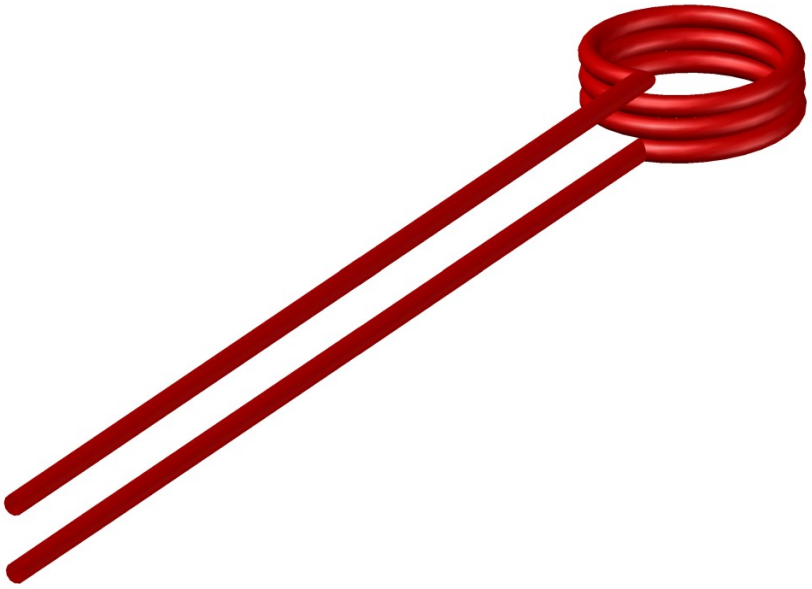

***Figure 3.25.*** *High temperature heat exchanger coil*

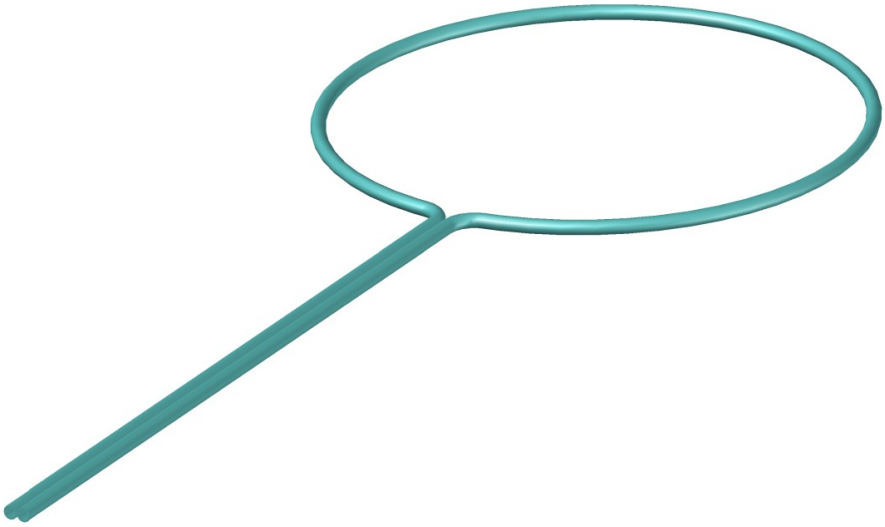

***Figure 3.26.*** *Low temperature heat exchanger coil*

## 3.6 Working simulations of the designed PEA system

The coupled thermal and electrical model described in Section 3.2 has been used to evaluate the space charge and electric field distribution within a 3 mm thick XLPE specimen.

The equation (3.12) has bee used to calculate the electrical conductivity of the sample whilst other electrical parameters of the PEA cell components are kept constant.

The Schottky injection model has been considered for the charge injection at the electrodes. As can be seen from equation (3.12), electrical conductivity depends not only on temperature but also on the electric field.

To prevent the calculation system from diverging due to this intrinsic non-linearity, it is necessary to limit the time step. Considering the number of elements that make up the computation mesh, it was found that the model converges with a time step of 0.5 s.

The simulated transient consists in the application of a voltage ramp up to 100 kV in 10 s without activating the heating/cooling systems. Once reached the target voltage, the upper part of the PEA cell is heated with an inlet temperature of the oil equal to 80 °C and a flow rate of 20 ml/min whilst the lower part is cooled with oil at 20 °C and a flow rate of 10 ml/min. At the same time, the DC voltage of 100 kV remains constant.

In Figure 3.27, the electric field distribution at the end of the voltage application ramp is shown. As it can be observed, the electric field modulus appears quite constant along the axial direction because no thermal gradient has yet been established within the sample. However, electric field peaks are noted near the edges of the high voltage cylindrical electrode. It is therefore recommended to fillet these edges.

***TABLE 3.6.*** *Main parameters for the operating simulation*

| **Parameters** | **value** | **Parameters** | **value** |
|---|---|---|---|
| transient duration | *3600 s* | sample permittivity | 2.3 |
| max time step | 0.5 s | PTFE thermal conductivity | 0.2728 W/(m*K) |
| mesh | *19907 elements* | PTFE mass density | 2125 kg/m$^3$ |
| sample thermal conductivity | 0.2857 W/(m*K) | PTFE specific heat | 965 J/(kg*K) |
| sample mass density | 930 kg/m$^3$ | PTFE permittivity | 2.1 |
| sample specific heat | 2580 J/(kg*K) | PTFE electrical conductivity | 1*10$^{-23}$ S/m |

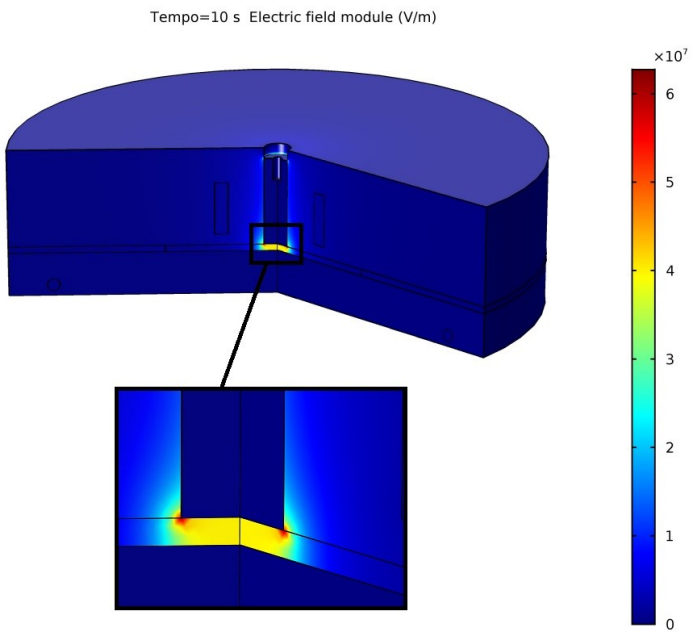


***Figure 3.27.*** *Electric field distribution at the end of the voltage application ramp (10 s)*

In Figure 3.28, the electric field distribution at the end of the 1 hour transient application is shown. As it can be observed, the electric field modulus increases from the high voltage to the ground electrode due to the thermal gradient established. The maximum value of electric field is therefore reached in proximity of the ground electrode.

In Figure 3.29, the distribution of the electric field modulus along the axial direction of the specimen is shown. As can be observed, the maximum electric field, reached near the interface between the dielectric and the ground electrode, achieves the value of 49 kV/mm. This value is 58% higher than that of the electric field in the vicinity of the HV electrode.

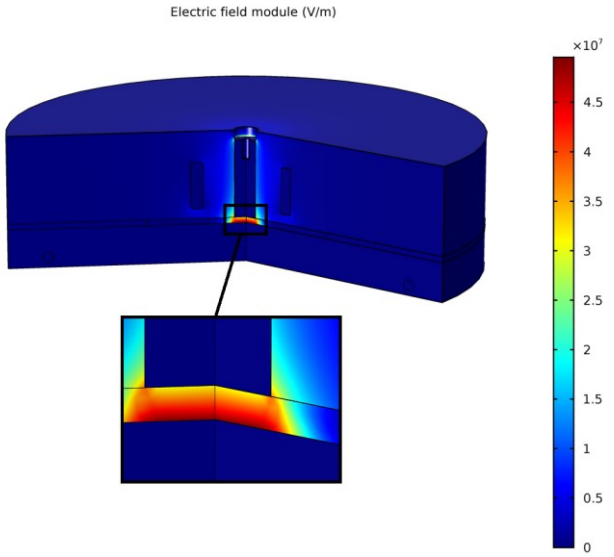


***Figure 3.28.*** *Electric field distribution at the end of the stable voltage application (3600 s)*

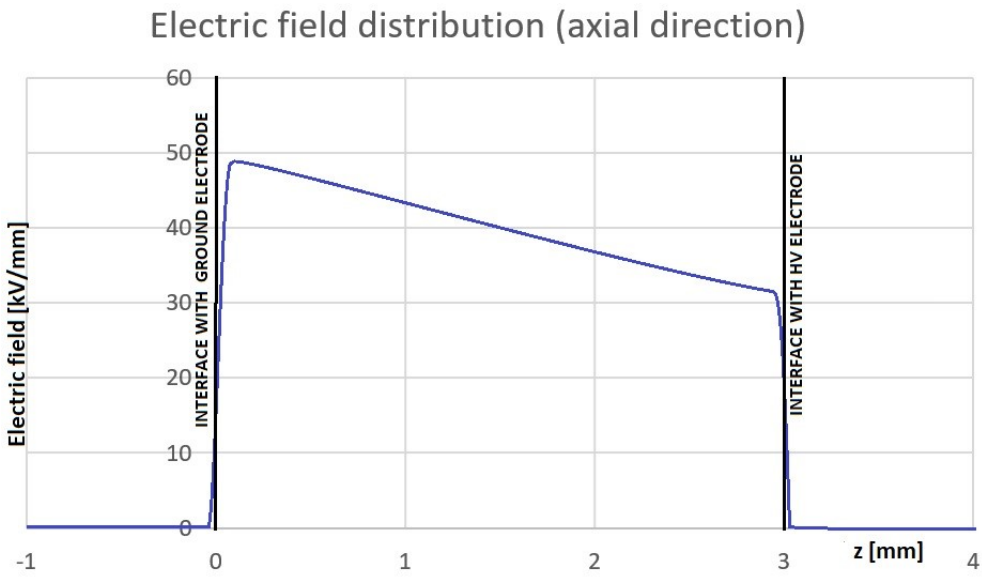


***Figure 3.29.*** *Electric field distribution along the axial direction at the end of the stable voltage application*

In Figure 3.30, the expected space charge distribution measured by the PEA system is shown. This distribution is the result of the simulations carried out starting from the above described conditions. As it can be observed, under the hypothesized test conditions, it should be possible to measure a space charge density of the order of tenths of a $C/m^3$ in the bulk of the dielectric. According to the simulations of the designed PEA system, it would therefore be possible to use this device to study space charge accumulation phenomena in the bulk of relatively thick specimens subjected to thermal gradient.

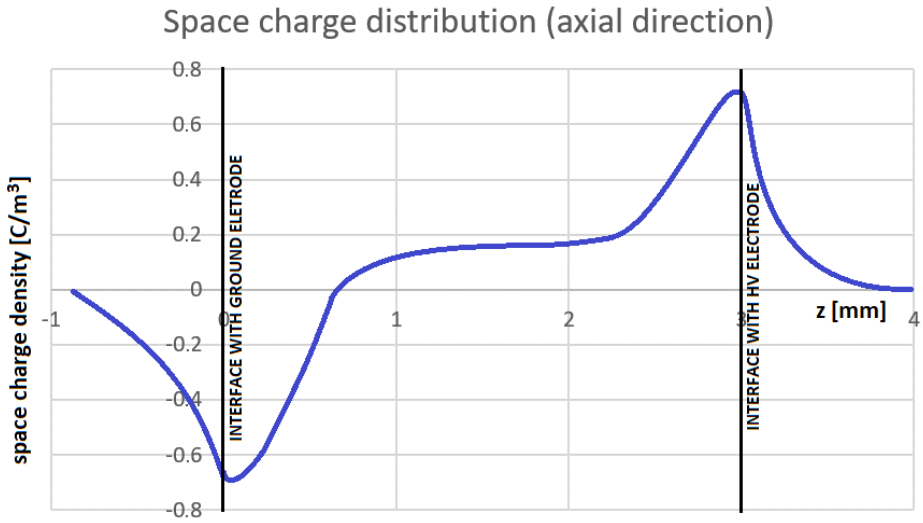


***Figure 3.30.*** *Expected space charge distribution along the axial direction at the end of the stable voltage application*

## 3.7 Drawings of the designed PEA cell

This section shows the drawing of the PEA cell designed and of the components not shown above, in order to better understand its structure and assembly procedure.

In Figures 3.31 and 3.32, the TPFE structure for the encasement of the HV electrode is shown. This component can be produced by machining a molded cylinder. In addition to the HV electrode seat, this component is characterized by a hole for the input of the fiber optic temperature sensor, a seat for the pair of coupling capacitors for the pulse generator, the seat for the heat exchanger coil to high temperature. TPFE material ensures good electrical insulation between the high voltage electrode and the aluminum cell case. In addition, the thermal conductivity of TPFE is similar to that of polymers typically used for high voltage cable insulation.

In Figure 3.33, the aluminum upper case is show. As can be seen, this component includes a 20 mm wide opening for the inlet of the tubes of the two exchangers, a 10 mm wide opening for the inlet of two fiber optic temperature sensors and a hole for the BNC connector for pulse generator output.

The upper part of the aluminum case has 4 holes for connection with the lower part shown in the Figure 3.34 by means of 4 socket head screws M8. The bottom of the case has 4 M8 threaded holes and one M4 threaded hole for the ground connection.

Figure 3.35 shows the assembly of the components that form the lower part of the complete PEA cell. A 5 mm thick dielectric specimen is also shown at the top of this assembly. Figure 3.36 shows the upper assembly of the PEA cell instead. The two parts, upper and lower, must be tightened using the 4 M8 screws with a tightening torque such as to allow total adhesion between the surfaces of the dielectric and those of the electrodes. To minimize the possibility that air gaps are present between these surfaces, it is advisable to treat them with silicone oil before closing the cell and starting the test.

In Figure 3.37-3.40, three-dimensional views of the fully assembled PEA cell are offered in order to show the details. Finally, in Figure 3.41, an exploded view of the PEA cell is shown.

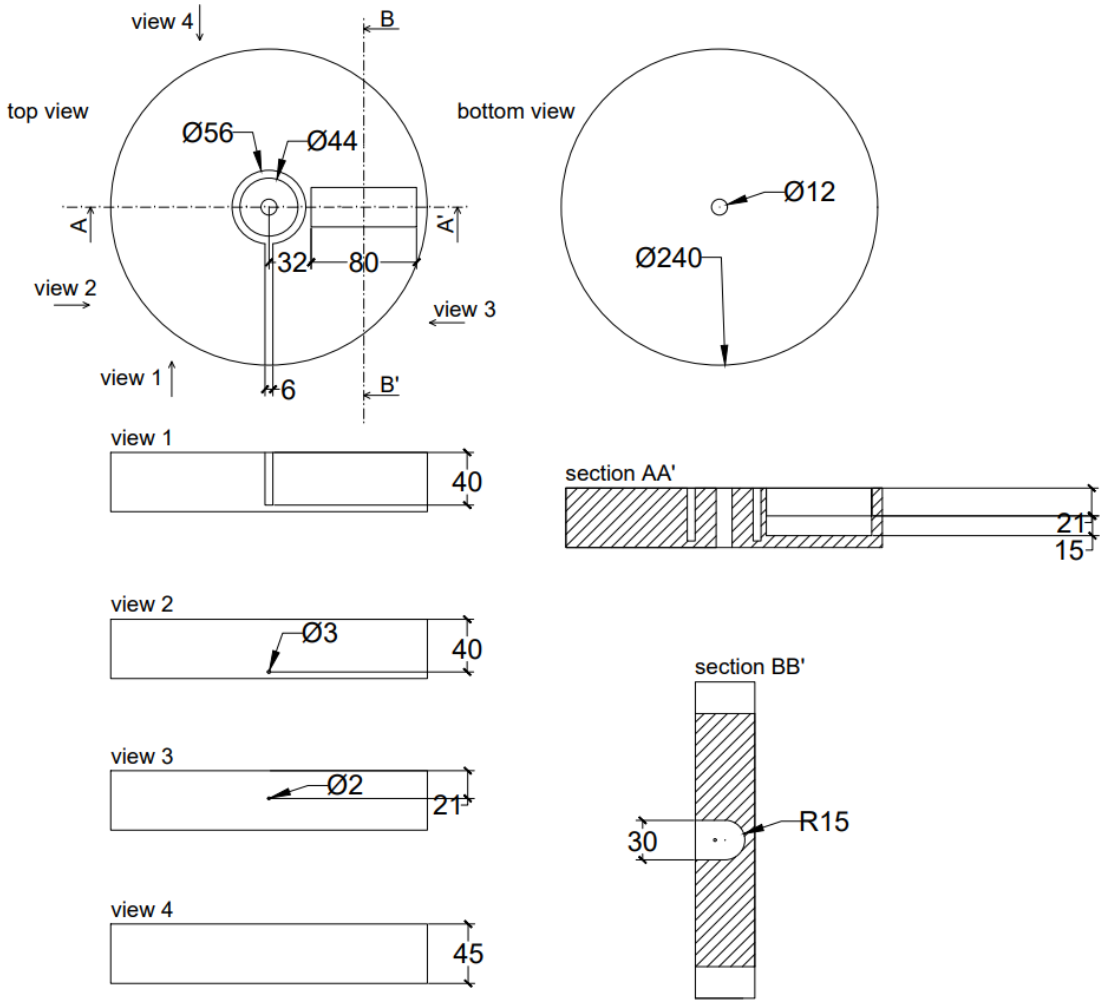


***Figure 3.31.*** *2D drawings of the TPFE structure for the HV electrode encasement*

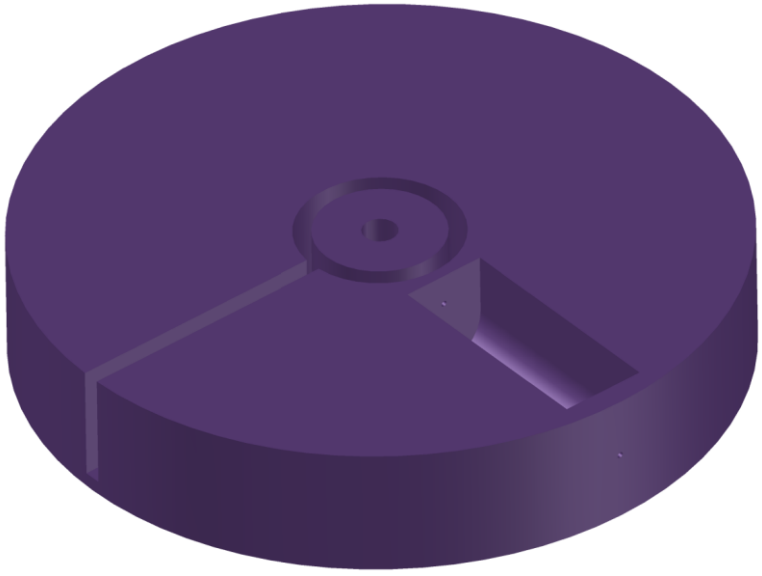

***Figure 3.32.*** *3D view of the TPFE structure for the HV electrode encasement*

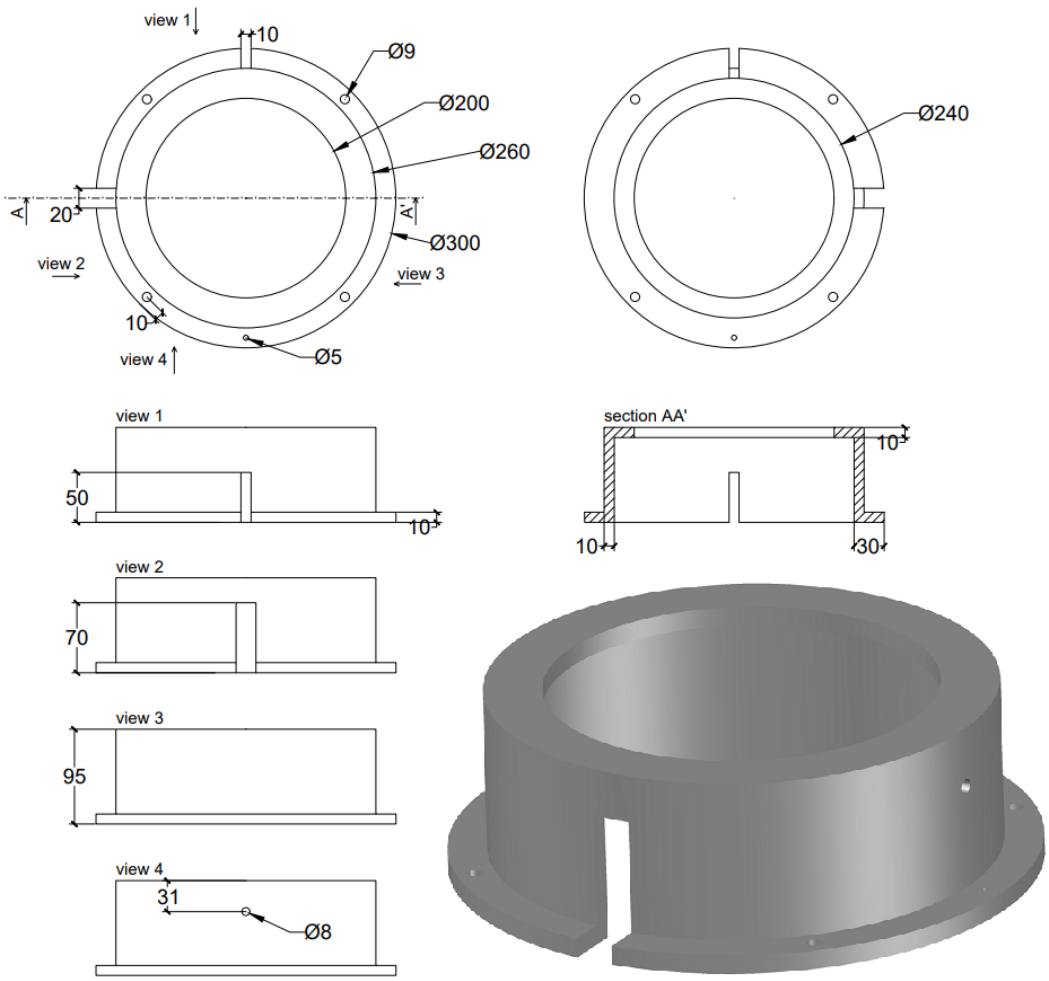


***Figure 3.33.*** *Aluminum case – upper part*

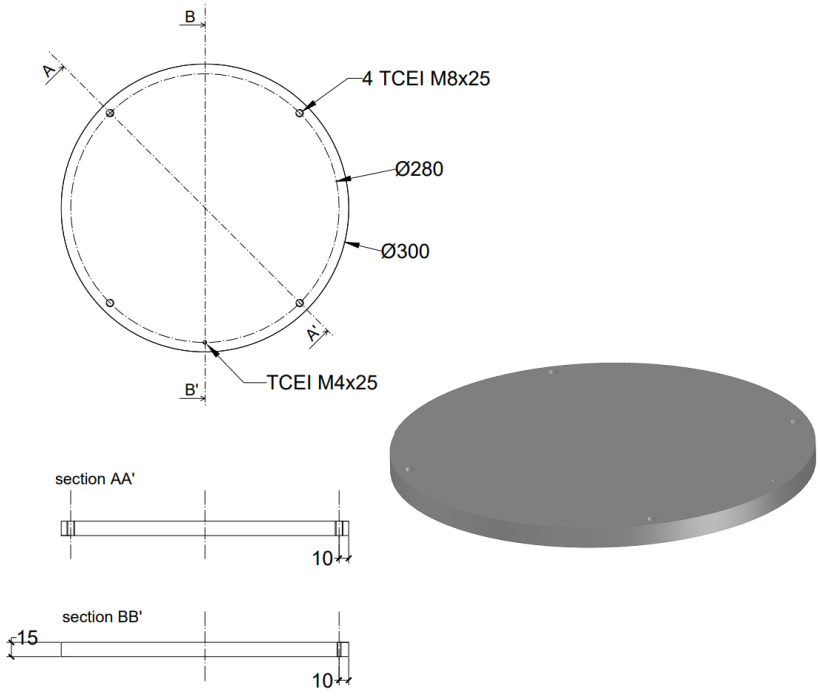


***Figure 3.34.*** *Aluminum case – lower part*

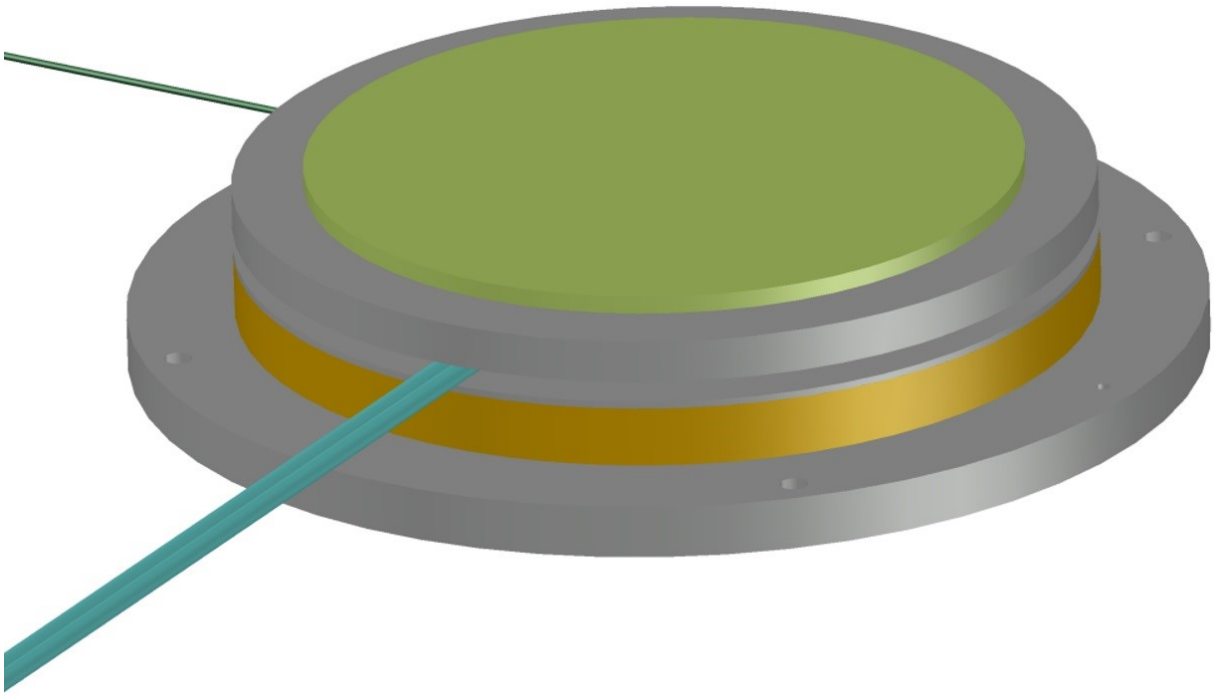

***Figure 3.35.*** *3D view of the PEA cell assembly – lower part*

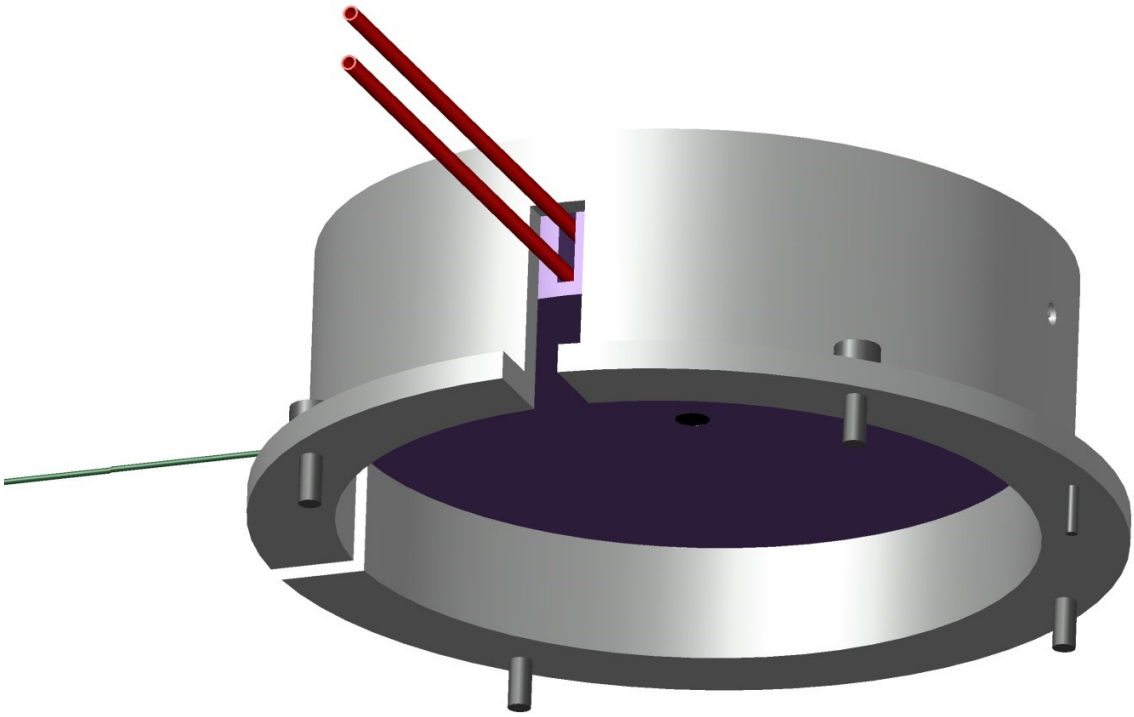

***Figure 3.36.*** *3D view of the PEA cell assembly – upper part*

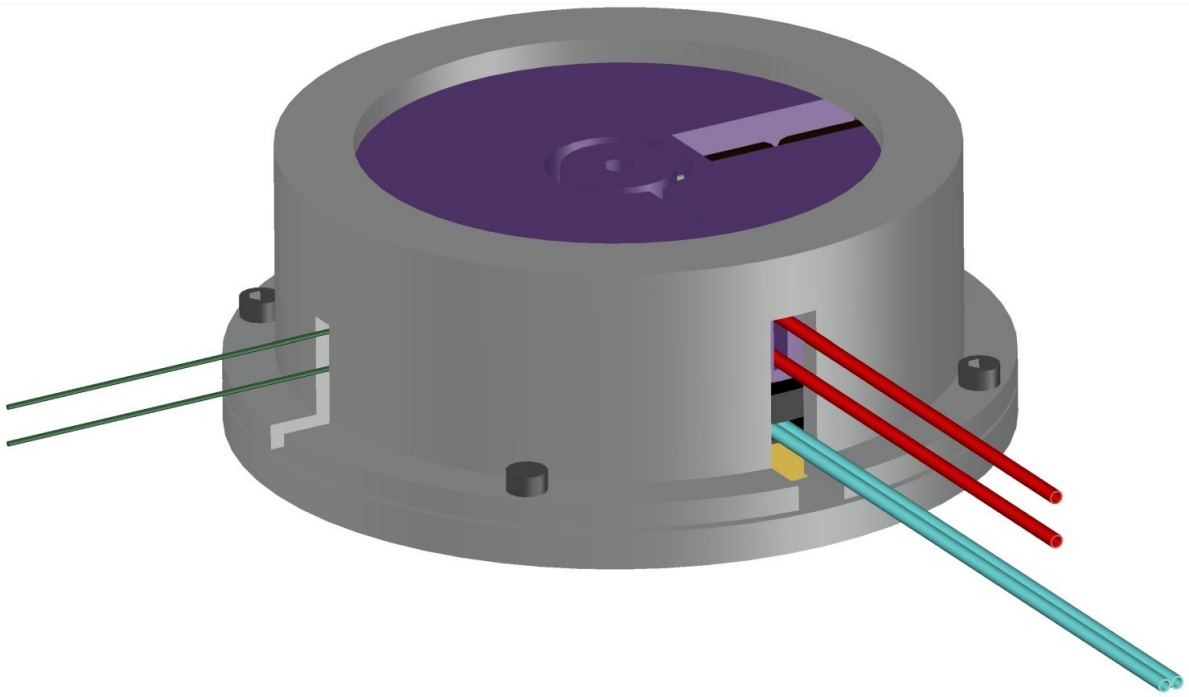

***Figure 3.37.*** *3D view of the PEA cell assembly*

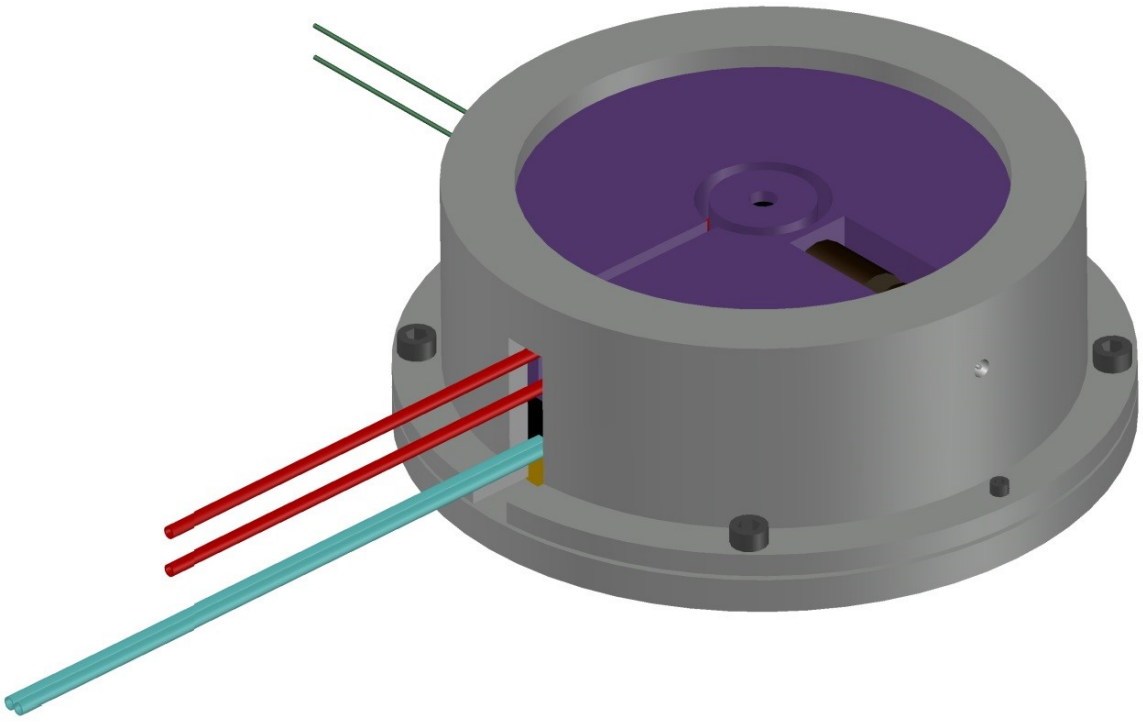

***Figure 3.38.*** *3D view of the PEA cell assembly*

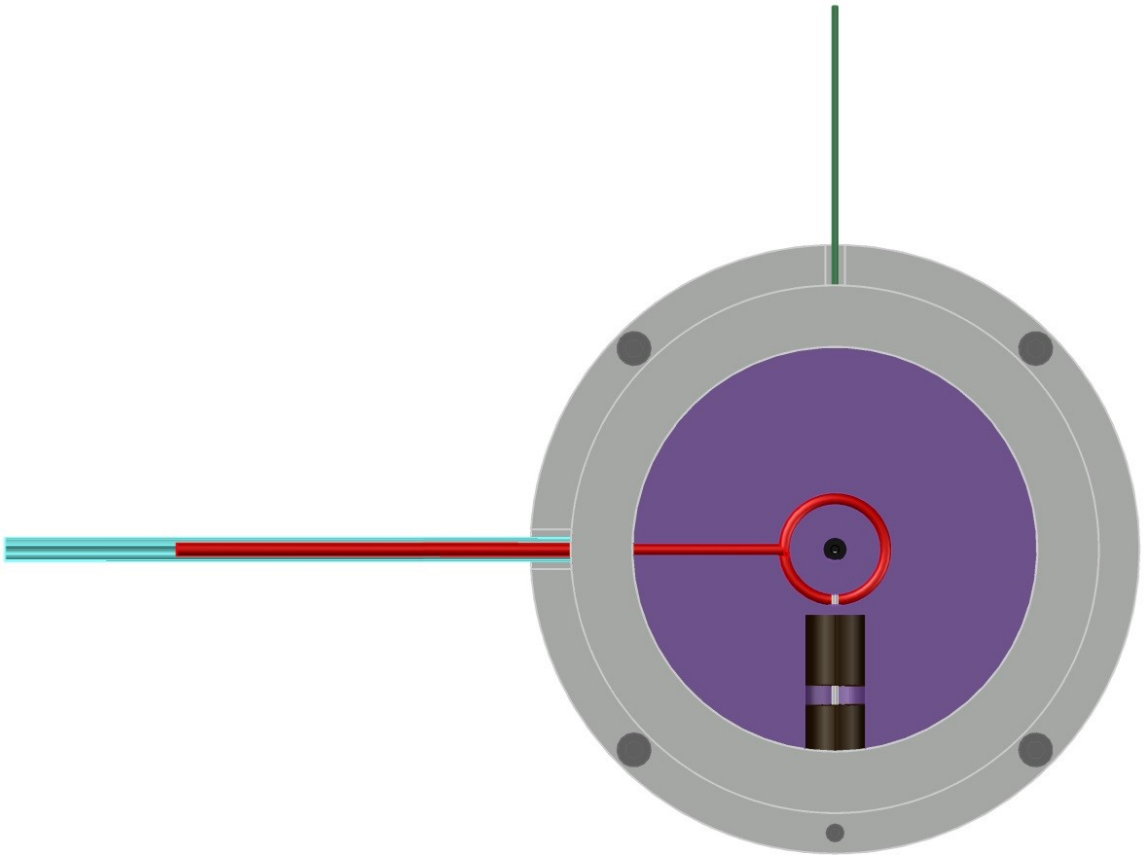

***Figure 3.39.*** *2D view of the PEA cell assembly – top view*

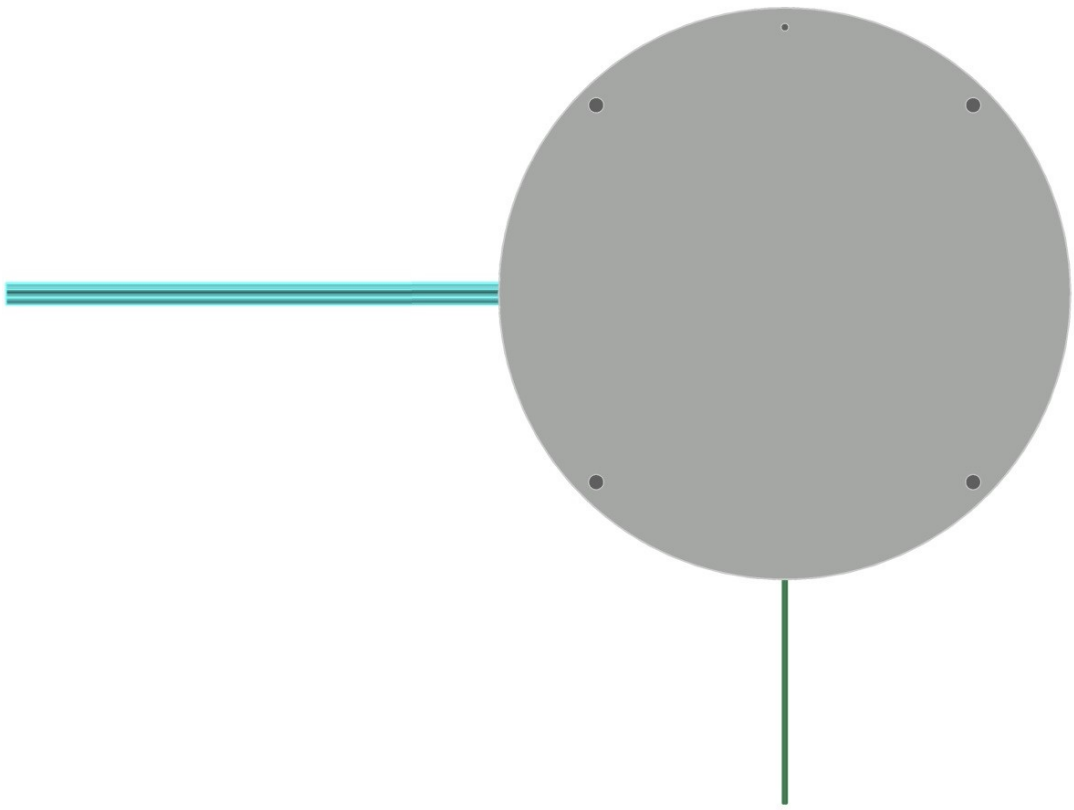

***Figure 3.40.*** *2D view of the PEA cell assembly – bottom view*

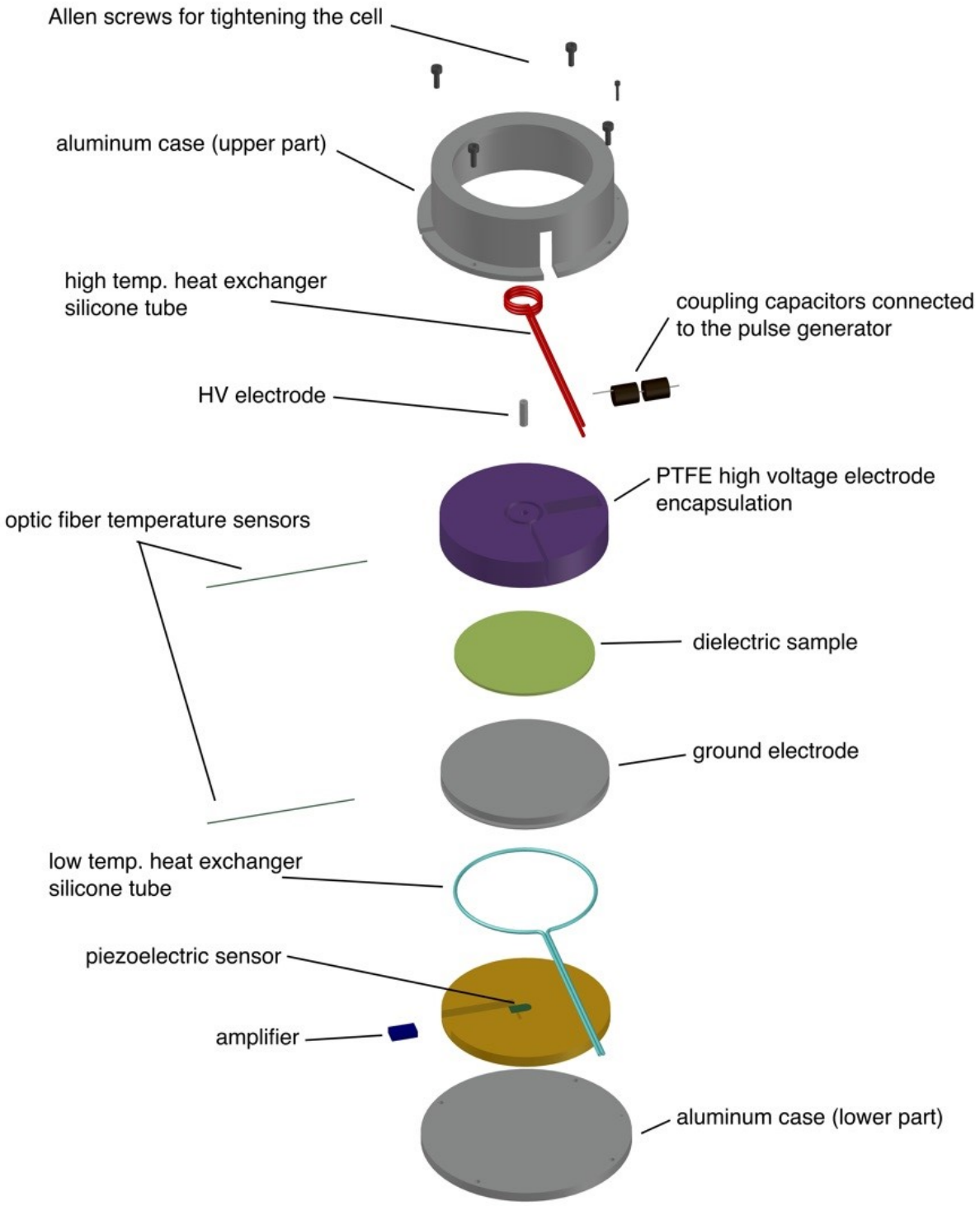


***Figure 3.41.*** *3D view of the PEA cell assembly – exploded view*

## 3.8 Conclusions

In this chapter, the design of a PEA system for space charge measurement on thick specimens is described. From bibliographic research, it can be concluded that, to date, the PEA cells available on the market and the prototypes developed by various researchers are suitable for thin specimens (thickness less than 1 mm) or for cables. As described in the previous chapters, temperature and its variation in space play an important role in conductivity phenomena in dielectrics and in the accumulation of space charge. PEA systems for flat specimens with thicknesses less than 1 mm are not suitable for the application of temperature gradients due to the low thermal resistance of the sample and the need not to subject the piezoelectric membrane to temperatures that can damage it. In the case of PEA systems for cables, it is possible to circulate current through the conductor and thus apply a thermal gradient to the dielectric. However, several peculiarities of the PEA measurement on cables, such as the application of electrodes for the application of the pulsed voltage, often make space charge measurements difficult to replicate and not very reliable.

With these assumptions, it has been considered appropriate to attempt to design a PEA system for flat specimens with a thickness of up to 5 mm with the possibility of applying a temperature difference of up to 20 ° C and a voltage up to 100 kV between the surfaces of the sample. The phenomena of space charge accumulation can determine local electric field peaks during polarity inversion phenomena. For this reason, it has been considered appropriate to use an HV voltage generator with reversible polarity and a pair of voltage generators of opposite polarity for the pulse generator. In this way, it will be possible to carry out experiments involving the sudden reversal of the polarity of the voltage applied to the plane specimen.

This device, once made and tested, could be useful to better understand the conduction phenomena in dielectrics at various temperatures, temperature gradients and electric fields.

First of all, once the project targets have been set, the thicknesses of the piezoelectric and of the ground electrode were identified, taking into account the transmission of the acoustic waves produced by the interaction between the pulsed voltage and the charges present in the sample. Based on these considerations, thicknesses of 52 μm, 20 mm and 17 mm have been chosen for the PVDF piezoelectric membrane, for the aluminum ground

electrode and for the PMMA absorber respectively. Starting from the targets in terms of spatial resolution, it has been chosen to apply pulsed voltage with pulses of width up to 120 ns.

The high voltage electrode has been designed after evaluating, by means of FEM simulations, the electric field in the air gap between this electrode and the ground. Furthermore, thanks to the geometry of a PTFE structure encasing the HV electrode, it is possible to cover the top part of the latter with mineral oil in order to avoid the occurrence of corona discharges during the experiments due to the connection with the output of the HV generator.

Taking into consideration the spatial resolution target, a pulse generator was designed with a frequency of 100 Hz, amplitude up to 6.7 kV and a half-height width of 112 ns. In particular, the designed pulse generator is based on the use of an HV switch controlled by a fast timer.

In order to make the signal produced by the piezoelectric distinguishable from the noise using an oscilloscope, the use of a 40 dB broadband amplifier has been considered.

In order to be able to apply a temperature gradient to the dielectric, two heat exchangers have been designed to be integrated with the PEA cell. The high temperature heat exchanger consists of a coil with 3 turns of silicone rubber tube, integrated with the PTFE structure, in which mineral oil flows moved by a peristaltic pump after being heated in an external tank by an electric resistance. The low temperature heat exchanger has a similar structure to the high one with the difference that the silicone rubber tube coil consists of only one turn and it is integrated with the ground electrode. The inlet temperature for the high temperature exchanger is 80 °C and the oil flow rate is 20 ml/min. On the other hand, a flow rate of 10 ml/min of oil at 20 °C keep the ground electrode at low temperatures. In the Table 3.7, a comparison between the main design targets and achieved results is shown.

After completing the PEA system design for thick specimens, a FEM analysis based on a coupled electrical and thermal principal component model has been conducted in order to evaluate the expected space charge distribution. The results of these simulations show that already for specimens with a thickness of 3 mm it would be possible to observe phenomena of accumulation of space charge in the bulk of the sample with density values comparable to those reached at the contact surfaces with the electrodes.

In the final part of this chapter, a set of drawing of the designed PEA cell is shown with the aim to illustrate the structure and the assembly procedure of this device.

***TABLE 3.7.*** *Main design targets and achieved results*

| **Parameter** | **symbol** | **goals** | | **achieved results** | | **unit** |
|---|---|---|---|---|---|---|
| | | min. | max. | min. | max | |
| **DC voltage** | *HVDC* | 30 | 100 | 30 | 100 | kV |
| **Sample thickness** | $d_{sa}$ | 3 | 5 | 3 | 5 | mm |
| **Sample diameter** | $diam_{sa}$ | 160 | 200 | 160 | 200 | mm |
| **Semicon thickness** | $d_{sem}$ | 0 | 1 | 0 | 1 | mm |
| **Spatial resolution due to the pulse width** | $\eta_{ep}$ | _ | 8 % | 4.5 % | 7.5 % | __ |
| **Spatial resolution due to the sensor thickness** | $\eta_{PVDF}$ | _ | 1.5 % | 0.88 % | 1.47 % | __ |
| **HV electrode diameter** | $diam_{HV}$ | 10 | 12 | 12 | | mm |

# Chapter 4
# Interaction between Space Charge accumulation and Partial Discharge occurring in dielectrics under HVDC stress

This chapter describes the attempt to predict Partial Discharge (PD) activity in experimental setups by means of conductive models for the estimation of the electric field inside a cavity.

Two case studies are reported in this chapter with the aim to use the inception and the repetition rate od PD as an indirect measurement of electric field in dielectrics under HVDC stress.

The first aimed to discreetly reproduce the effect of a cavity inside a dielectric subjected to thermal gradient and HVDC stress. A cell consisting of two electrodes and a flat specimen of thermoplastic insulating material was immersed in heatable mineral oil. This was connected in series with a second cell, similar to the first, inside which an artificial defect was created. The second cell was immersed in mineral oil kept at room temperature. Both cells, connected in series, were subjected to different HVDC voltage levels while a PRY-CAM® antenna sensor detects the possible occurrence of partial discharges and also measures the waveforms. The experimental setup was modeled with a lumped-parameter circuit diagram developed in the time domain in which the resistance values are updated at each time step taking into account the temperature electric field according to the Equation (1.4). The objective of this investigation was both the analysis of the correlation between DC conductivity in dielectrics and the onset of PD as well as the validation of a simplified conductivity model to predict such phenomena.

The second case study had the same objective as the first but, in this case, the experimental setup consisted of a model cable insulated with thermoplastic material, containing an artificial defect between the dielectric and the outer semiconductor, subjected to constant voltage and load current. In this case, simulations of the phenomenon were conducted using a coupled thermal and electrical 3D model in the time domain implemented in a FEM software. As it will be seen from the results of the investigations reported below, it seems that the phenomenon of PD under DC voltages occurs under Partial Discharge Inception Electric Field (PDIEF) higher than that observed under AC stress [81-84]. In reality, as argued in the previous chapters, the conductivity models do not

take into sufficient consideration the phenomena of injection at the interfaces nor the phenomena of entrapment and de-entrapment of charge carriers inside the dielectrics [85-89]. However, the phenomenon of the onset of partial discharges can be modeled using an "Equivalent" PDIEF (EPDIEF) parameter that incorporates the accumulation of charges at the interfaces of the defect. Inevitably, this parameter will depend on the quality of the defect surface, the dielectric material, the pressure and temperature of the gas in the cavity and the aging. However, from the several experiments conducted under different temperature conditions it was concluded that the EPDIEF parameter remains within a range within about 10% of its magnitude.

## 4.1 Partial Discharge activity in an experimental setup consisting of two cells at different temperatures, connected in series and under HVDC voltage stress

It is widely accepted that the occurrence of Partial Discharges within dielectric materials for both AC and DC voltages is one of the factors that contribute most to aging and insulation failure [90-94]. PD recognition in case of AC voltage stress typically occurs by synchronizing the time in which the discharge is detected with the phase of the applied sinusoidal voltage. By superimposing the distribution pattern in phase and amplitude of the PDs with the sinusoid of the applied voltage, it is possible to make qualitative considerations that lead to the recognition of the type of discharge. This qualification is not feasible in the case of measurement of PD under DC stress as there is no sinusoidal voltage applied. Furthermore, as reported by many researchers, under the same conditions, the number of PD detectable under DC stress is significantly lower than that of PD detectable under AC voltage. This involves difficulties in recognizing discharges as their number can be of the same order of magnitude as the noise. As part of this investigation, PD recognition was made on the basis of the similarity of the waveform with discharges recognized as internal by testing under AC voltage. PD measurement is carried out by means of a PRY-CAM® antenna sensor with which it is possible to obtain the waveform of the discharges with an 8-bit resolution.

This investigation aims to evaluate the relationship between space charge accumulation and PD phenomena through the use of a novel experimental setup. In particular, an “Equivalent” PD Inception Electric Field (EPDIEF) was evaluated in order to model the experimental setup by means of a simplified conductivity model. As mentioned above,

space charge measurements demonstrate that space charge accumulation enhanced by other phenomena, namely the trapping and de-trapping of charge carrier as well as their injection at the interfaces between facing layers, are not properly reproduced by macroscopic conductivity models.

The Bipolar Charge Transport (BCT) models describe with higher detail the microscopic phenomena occurring inside a dielectric material subjected to DC stress. However, a large number of parameters is necessary to properly characterize the BCT model to practical cases, therefore, the estimation of the electric field distribution by means of these detailed models remains difficult to perform [95,96].

In this study, the evaluation of the EPDIEF value is used as an indirect measurement of the electric field inside a cavity incorporated in a dielectric subjected to HVDC stress and temperature gradient. With this purpose, an experimental setup has been designed where two identical dielectric cells were connected in series and held at different temperatures. One of the cells contained a void mimicking a defect in the insulation.

The DC voltage was applied and its division between the cells reflected the voltage drops across cable insulation exposed to a thermal gradient. To identify the relationship between the conduction through the dielectric and the actual electric field level inside the cavity, PD activity was investigated at various temperatures of the cells.

In Figure 4.1, a schematic of the novel experimental setup is shown. As it can be seen, a 0.5 mm thick XLPE sample is tightened between two aluminum electrodes and immersed in mineral oil which can be heated through an electrical resistance. In the second cell, two sheet of XLPE with a thickness of 0.3 mm are stacked between the two electrodes and immersed in mineral oil kept at room temperature.

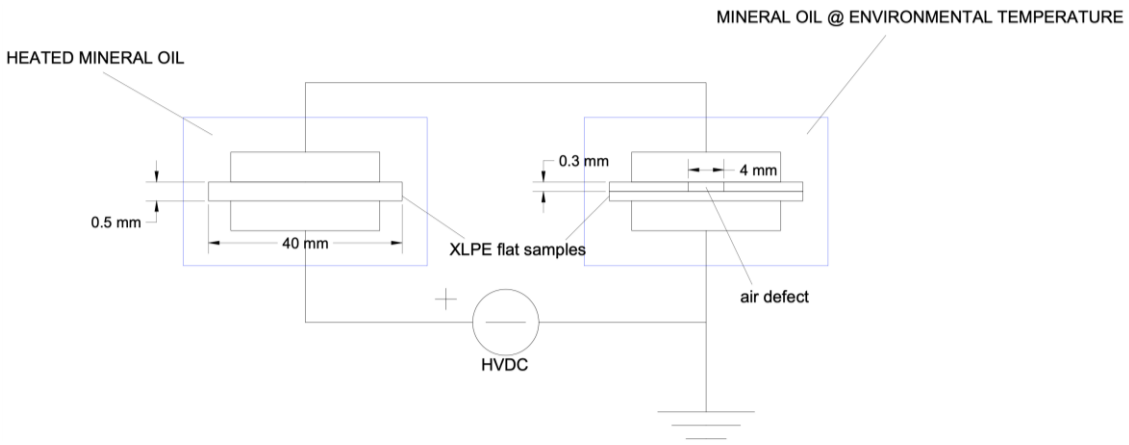


***Figure 4.1.*** *Schematic of the novel experimental setup*

In Figure 4.2, the arrangement of the cell with healthy dielectric specimen is shown. As it can be seen, the cell is immersed in the oil contained in a tank with a heating resistance. The oil is moved from a pump and a temperature sensor is positioned in proximity of the cell. In Figure 4.3, the encasement of the defected sample with the PRY-CAM® antenna sensor facing the ground connection is shown.

In Figure 4.4, the defected sample is shown. the regularity of the cut contours and the absence of roughness are very important factors for obtaining only one main discharge phenomenon. The two samples of the second cell are made to adhere by means of silicone gel in order to avoid the entry of oil into the defect. However, to prevent the gel from compromising the analysis, it is positioned outside the electrode projection.

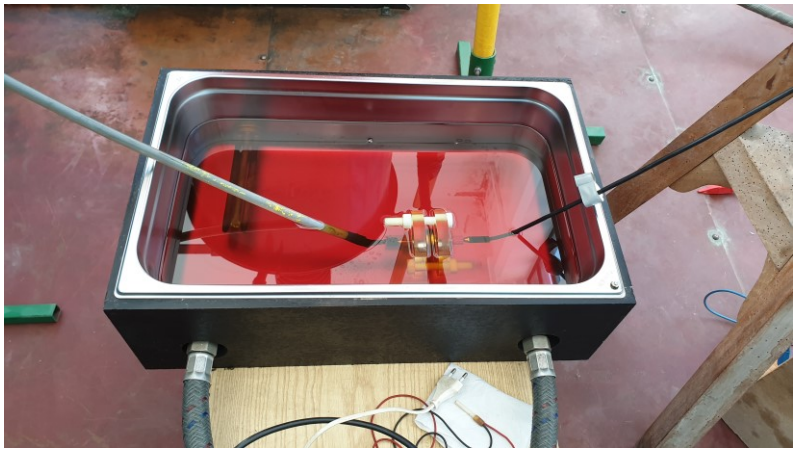

***Figure 4.2.*** *Arrangement of the cell immersed in heatable mineral oil*

***Figure 4.3.*** *Arrangement of the cell immersed in mineral oil kept at room temperature*

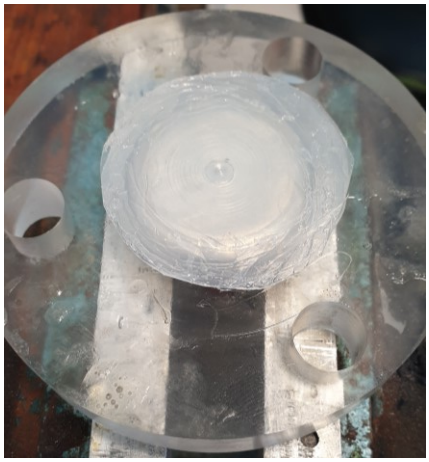

***Figure 4.4.*** *XLPE specimen with defect*

To one of the two specimens of the second cell, a hole with a diameter of 4 mm is made. The cavity faces the electrode connected to the first cell in order to favor internal PD. The output of an HVDC voltage generator is connected to the free terminal of the cell immersed in heatable oil while the free terminal of the cell at room temperature is grounded. The oil in the tank containing the cell with healthy sample was heated through a resistor driven by an automatic system with temperature feedback included. The oil temperature was monitored through a PT100 temperature sensor. During the experiments, the applied voltage was varied as shown in Table 4.1 and each ramp lasted approximately 1 s. Once the exceeded a certain voltage threshold defined as Partial Discharge Inception Voltage (PDIV), the onset of PD in the cavity was expected with a conventional minimum repetition rate equal to 1 $min^{-1}$. The PD activity is detected by a PRY-CAM® positioned in proximity of the second cell ground connection. In accordance with conductivity models for dielectrics, higher electric field magnitude inside the cavity should be reached at higher temperatures of the first cell compared to that of the second cell. Therefore, it can be expected that the PD activity is going to be dependent on the difference in the temperature of the two test cells. To verify this, two experiments have been performed by varying the temperature of the cell with healthy insulation.

***TABLE 4.1.*** *Voltage variation during the experiments*

| Time (s) | Voltage (kV) |
|---|---|
| 0-360 | 10 |
| 360-620 | 15 |
| 620-960 | 20 |
| 960-1060 | 0 |

### 4.1.1 Experiment 1 – two cells at the same temperature

The first experiment was performed keeping both cells at room temperature of 20 °C and by applying the voltage variation trend reported in Table 4.1. No PD were detected when the applied voltage was equal to 10 kV and 15 kV with the exception of few discharges measured during the transition from 0 to 10 kV at the beginning of the experiment. This can be attributed to the high polarization current achieved during the voltage transition. In Figure 4.5, the waveform of a typical PD trace acquired at the voltage level of 20 kV is shown. In order to exclude signals not related to PD activity, a software filter was applied to the measured signals and the similarity of the waveforms characterized by the prevailing frequency of 32 MHz was utilized. The choice of this frequency level was made starting from the results of tests previously carried out with the application of AC voltage. Once completing the denoising process, the time trend of the PD repetition rate was obtained as illustrated in Figure 4.6. As can be seen, peak repetition rates of 15 $s^{-1}$, 6 $s^{-1}$ and 8 $s^{-1}$ were reached during the different voltage ramps of 0-10 kV, 15-20 kV followed by the reduction to zero level. Repetition rate of 0.07 s-1 was measured when the voltage was kept at the stationary value of 20 kV.

The amplitude distribution of the selected PD is shown in Figure 4.7. The result suggests that the measured PD magnitude can be divided into two main groups. The first is characterized by an average amplitude of about 40 mV whilst the second is composed of PD with an amplitude of about 120 mV. All the highest energetic PD have however been observed immediately after voltage change.

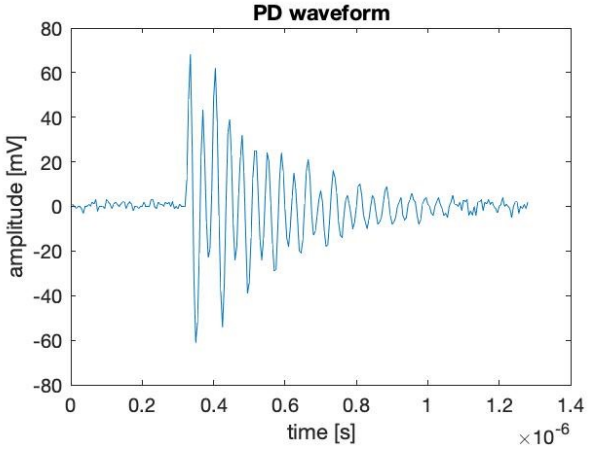


***Figure 4.5.*** *Typical PD waveform corresponding from the internal defect (cavity)– Experiment 1*

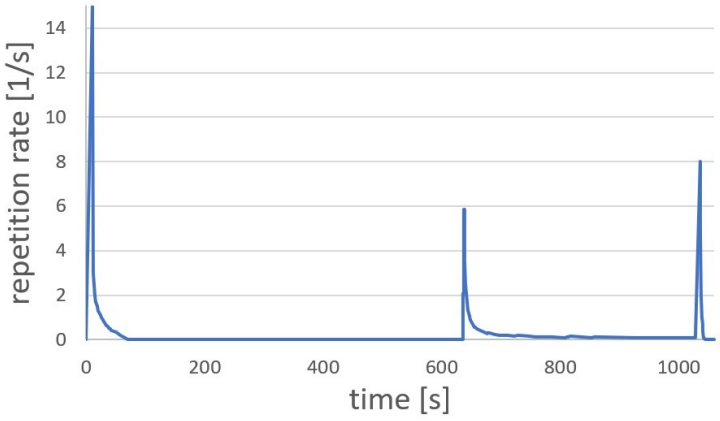


***Figure 4.6.*** *Time trend of PD repetition rate – Experiment 1*

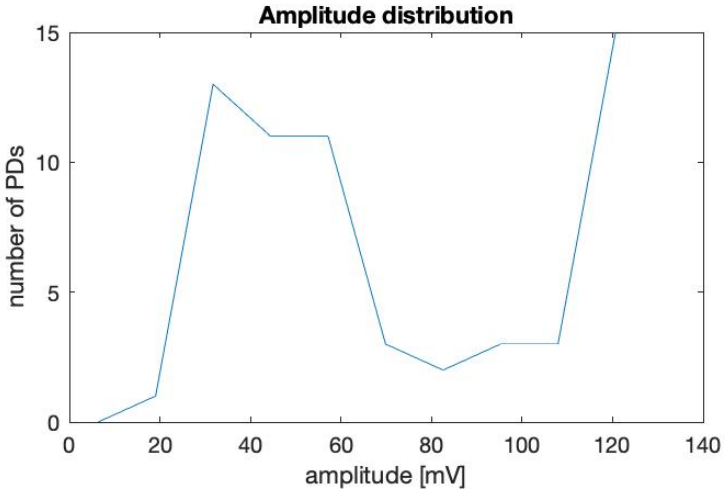


***Figure 4.7.*** *Signal amplitude distribution – Experiment 1*

### 4.1.2 Experiment 2 – fist cell at 80 °C and second cell at 20 °C

The second experiment was carried out by applying the same voltage shape as in the first test, see Table 4.1, but in this case, the first cell was kept at 80 °C and the second one was held at room temperature (20 °C). The waveform of the signal related to the typical PD occurrence acquired during the Experiment 2 is shown in Figure 4.8. The same denoising principles as in the first experiment were applied with the same filtering parameters. The obtained time trend of the PD repetition rate is shown in Figure 4.8. As seen, the first peak was detected at 100 $s^{-1}$ immediately after the application of the initial voltage step of 10 kV. Then, the repetition rate decreased towards an average value of 0.06 $s^{-1}$. Another peak of 16 $s^{-1}$ appeared when the voltage was increased to 15 kV and the new average rate of approximately 0.08 $s^{-1}$ was maintained when the voltage was kept constant. Once the

voltage was further increased up to 20 kV, a succession of peaks in the distribution up to the magnitude of 50 $s^{-1}$ was observed during the first 800 s of the test. Then, an average PD repetition rate between 2 and 4 $s^{-1}$ was measured until a new peak value of 30 $s^{-1}$ was reached when the voltage was reduced to zero. Finally, the PD repetition rate dropped to zero in a few tens of seconds. In Figure 4.9, the distribution of the amplitude of the de-noised PD is shown. As can be observed, the most part of the measured PD are characterized by a signal with the amplitude between 20 mV and 60 mV. As in experiment 1, a significative number of PD characterized by a signal amplitude of about 120 mV was detected immediately after the voltage change.

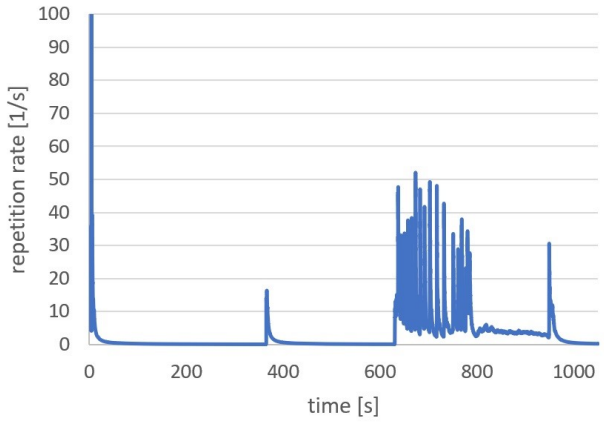


***Figure 4.8.*** *Time trend of PD repetition rate – Experiment 2*

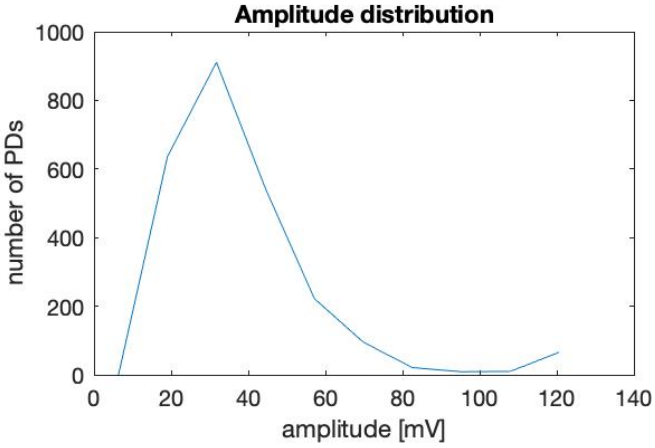


***Figure 4.9.*** *Signal amplitude distribution – Experiment 9*

### 4.1.3 Circuital model of the novel experimental setup

The novel experimental setup described above has been modeled by means of the circuital schematic with lumped parameters shown in Figure 4.10. The voltages and the

currents at the lumped elements were calculated by means of a calculation code implemented in Matlab® in time domain with a time step of 0.1 μs. In the model, the values of the resistors *Ra*, *Rb*, and *Rd* are updated at each time step when estimating the electrical conductivity of XLPE for local values of the field strength *E* and temperature *T* using the Equation (1.4). The value of *Rc* referred to the cavity is calculated using the electrical conductivity of air, which is assumed to be a function of the local electric field modulus *E* as follows:

$$\sigma_a = \begin{cases} 10^{-15}\ S/m, E < E_{inc} \\ 10^{-4}\ S/m, E \geq E_{inc} \end{cases} \tag{4.1}$$

where $E_{inc}$ is the discharge inception field calculated by means of Paschen's law. Once PD are incepted, the conductivity of air is set as

$$\sigma_a = \begin{cases} 10^{-15} S/m, E < E_{est} \\ 10^{-4}\ S/m, E \geq E_{est} \end{cases} \tag{4.2}$$

where $E_{est}$ is the extinction electric field assumed to be equal to 1 kV/mm.

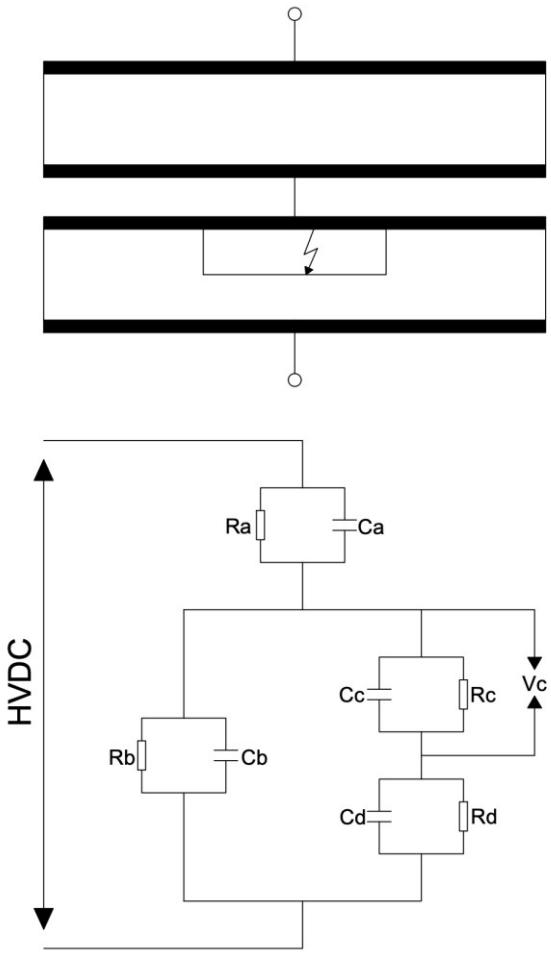


***Figure 4.10.*** *Schematic of the experimental setup*

Both experiments have been simulated by applying the model based on the equivalent circuit in Figure 4.10. The time trend of the PD repetition rate obtained while keeping the two samples at the same temperature is shown in Figure 4.11. As it can be seen, the repetition rate of 27 $s^{-1}$ was calculated when the voltage passes from 0 to 10 kV whilst no PD occurred in the passage from 10 kV to 15 kV. PD repetition rate of 14 $s^{-1}$ was obtained during the ramp between 15 kV and 20 kV, and 21 $s^{-1}$ immediately after the voltage was reduced to zero.

The simulation of the Experiment 2, when the samples were kept at different temperatures, resulted in no PD observed during the stable part of the applied voltage. The obtained time trend of the repetition rate is shown in Figure 4.12. For this case, the rates of 27 $s^{-1}$, 14 $s^{-1}$, 7 $s^{-1}$ and 22 $s^{-1}$ were found during the subsequent voltage ramps. Unlike for the case when the cells were kept at the same temperature, the repetition rates of 1 $s^{-1}$ and 5 $s^{-1}$ were observed for stable voltages 15 kV and 20 kV.

### 4.1.4 Discussion

The number of PD identified after the aforementioned denoising process, is equal to 66 during Experiment 1 and 2221 for Experiment 2. When introducing the temperature difference between the two cells, the number of PD detected during the voltage variations is about 4 times higher than in the case where the samples remain at room temperature. The two experiments were reproduced several times with different values of the ambient temperature leading to similar results.

During the stable phases of the Experiment 1, a PD activity of 0.07 $s^{-1}$ has been detected only at 20 kV. On the contrary, during the Experiment 2, repetition rates of 0.06, 0.08 and 3.0 $s^{-1}$ have been found under the stable phases at 10, 15 and 20 kV, respectively. The number of PD observed at the maximum measured amplitude of 127 mV is then 4 times higher when the two samples are at different temperatures. On the other hand, the modelling showed that in the case of two samples subjected to the same temperature, three peaks of PD repetition rate occurred when the voltage passes from 0 to 10 kV, from 15 kV to 20 kV and from 20 kV to 0. The maximum repetition rate values reached during voltage transitions are in average 2.5 times lower than what is observed experimentally. Hence, the experimental and computational results agree regarding the substantial absence of PD during the stable voltage phase. In the case of two samples subjected to different temperature, the peaks of PD repetition rate resulting from the simulations during the increasing voltage ramps are lower than those observed experimentally. Thus, there is a similarity between experimental and computational results regarding the repetition rates

during the stable voltage phases also in this case. The distributions of PD amplitudes demonstrate a prevalence of high amplitude PD in the case of two samples of the same temperature whilst the most part of PD detected during Experiment 2 are characterized by an averaged PD amplitude of 35 mV. This can be explained with the prevalence, in this case, of PD occurring during the stable phase. In this scenario, the statistical time lag for the appearance of a starting electron is negligible during the stable phases because of the large time constant for the cavity charging. This does not happen during the Experiment 1, where the majority of PD occurs at the voltage ramps.

## 4.2 Partial Discharge activity in an artificially defected model cable under constant HVDC voltage and current load

In this study, the PD phenomenon in an artificial defect within the insulation of a model cable has been experimentally investigated whilst HVDC voltage and load current are applied. A hemispherical shape defect has been made on the outer surface of the thermoplastic dielectric layer of a model cable. An HVDC voltage and a load current are applied at the beginning of an experiment lasting one hour in order to determine a thermal and therefore also an electrical transient inside the insulation.

The main goal of the experiment is to verify the effect on the PD activity of the establishing temperature distribution during a load transient. It is expected that the electric field in proximity of the dielectric's outer surface increases as a consequence of the space charge accumulation due to the establishment of the temperature gradient. In this scenario, the PD measurement can be considered as an indirect evaluation of the electric field in proximity of the artificial defect. The test voltage level has been chosen so as to observe the time when the PD inception threshold is exceeded by the electric field within the cavity whilst the thermal equilibrium is not yet reached.

The case study has been simulated through a coupled thermal and electrical model based on the heat conduction equation, the Gauss law for space charge and the electrical current continuity equation. The model has been applied to a three-dimensional geometry and it is implemented in Comsol Multiphysics® in time domain. As for the study described in the previous section, also in this case, one of the objectives was to validate and calibrate a conductivity model capable of predicting PD phenomena in dielectrics subjected to HVDC voltage.

### 4.2.1 Experimental setup and results

In Figure 4.11, the experimental setup used for the evaluation of the PD activity within an artificial defect made on an HVDC model cable is shown. The model cable is short-circuited forming a loop by means of a junction between its terminals. A current equal to 260 A is induced in the mini cable by a transformer primary as indicated in the Figure 4.11. The thermal power generated in the cable by the Joule effect leads to the establishment of a radial temperature distribution inside the insulating layer.

The current and the external temperature of the cable are measured in real time by means of a Rogowski and a PT 100 respectively. Based on these information a real time thermal rating is performed to obtain the time trend of the conductor temperature and, therefore, of the temperature drop over the insulation thickness.

A direct voltage of 60 kV has been applied, by an HVDC generator, between the conductor and an aluminum tape wrapping the outside of the cable. The PD are detected by means of a PRY-CAM® antenna sensor positioned in proximity of the connection between the outer semiconductive layer of the cable and the ground.

The aforementioned defect has been created on the outer surface of the dielectric in the center of a 6 m long cable insulated with a 5 mm thick thermoplastic layer. The conductor radius was equal to 5 mm and the filling factor equal to 0.91. In Figure 4.12, the structure of the defected area is shown. A pseudo-hemispherical defect with a diameter of about 1 mm has been created through a knife cut. A rectangular portion of the outer semiconductive layer has been removed before smoothing the outer surface of the thermoplastic material and subsequently etching it with the tip of a knife. The defect area has been then restored by affixing a rectangular sheet of semiconductive material of the same size as the removed portion.

In order to mitigate the effects on the onset of partial discharges of the high roughness of the exposed dielectric part, silicone gel has been inserted filling the gap created. Although it is not possible to exclude the PD may be triggered in areas other than the main defect, it is expected that the PD of greater amplitude must originate from knife cut. The distribution of the electric field in the vicinity of the defect can be influenced by the presence of the silicone gel due to possible accumulations of space charge due to the creation of an additional interface.

However, in the radial path through the defect, the gel layer is not encountered. Furthermore, in order to optimize the recognition of the internal PD occurring in the main defect, an AC test has been carried out in order to record the frequency spectrum of the PD detected under this condition. Following the restoration of the semiconductive layer in the area of the defect, an aluminum tape is wrapped around this portion of cable and connected to the ground so as the measurement of PD by means of the antenna sensor can be performed. This further layer which acts as a screen is tightened around the cable by using a further insulating sheath.

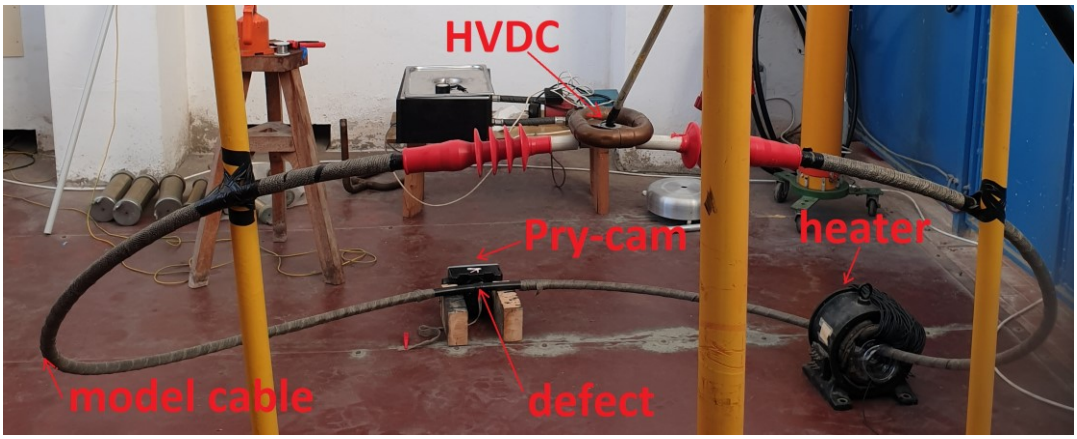


***Figure 4.11.*** *Experimental setup for PD detection under HVDC voltage and current load*

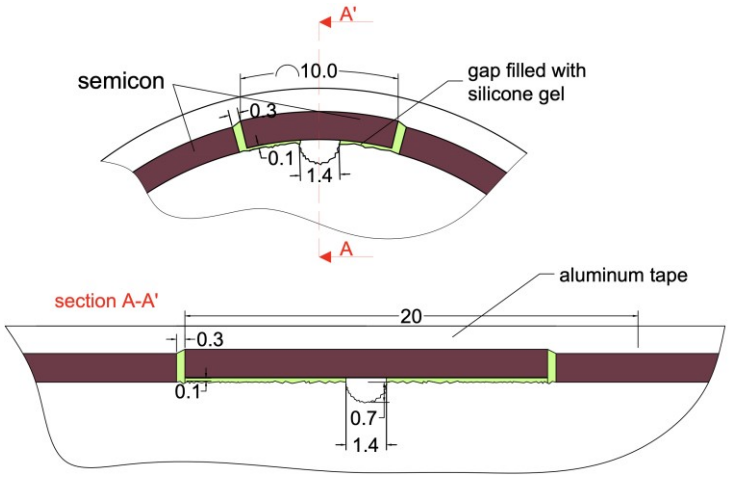


***Figure 4.12.*** *Structure of the defected area*

Before starting the experiment with HVDC voltage application, a PD measurement under AC voltage has performed in order to characterize the type of discharge associated with the artificial defect. This preliminary experiment has been carried out with gradually increasing tension in order to determine the value of the PD Inception Voltage (PDIV) under AC stress. This measurement has been performed with the same positioning of the

components of the experimental setup. A PDIV value equal to 19 kVrms has been found during the tests under AC voltage. In Figure 4.13, the PD pattern and the typical waveform are shown. The main frequency components of the waveform observable at the top right in Figure 4.13 have been found around 32 MHz. Once the typical waveforms of the discharges detected under AC voltage have been characterized by FFT, they have been recorded and used as a comparison for the denoising of the measurements under DC voltage.

The experiment started by simultaneously applying a DC voltage of 60 kV and a current of 260 A through the conductor by means of ramps lasting 10 s. The application of voltage and current were kept stable for 60 minutes and finally the cable was disconnected. PD are measured throughout the duration of the experiment and for 5 minutes following shutdown. As mentioned above, the PD measurement test under HVDC voltage has been performed while the conductor of the model cable is heated by passing an induced current. the initial temperature of the cable, equal to that of the room, was equal to 24 ° C.

In Figure 4.14, the trend of the temperatures inside the conductor and at the cable outer surface is shown. As specified above, the temperature at the outer semiconductive layer is measured in real time by means of a PT100 adjacent to the cable surface and thermally insulated from the outside. The temperature inside the conductor is calculated by means of a thermal model of the experimental setup implemented in a FEM software. As can be seen from the 4.14, a thermal equilibrium is reached about 45 minutes after the beginning of the experiment, when the conductor reaches a temperature of 46 °C with a drop of about 11 °C across the insulation.

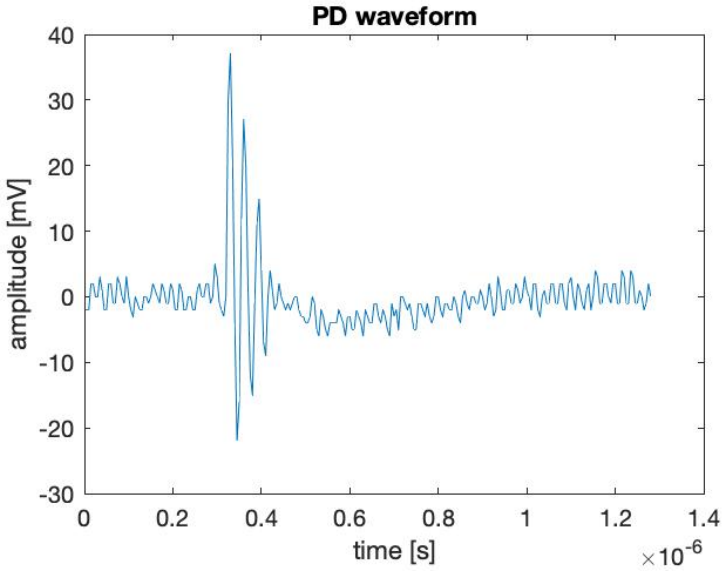


***Figure 4.13.*** *Typical waveform of the PD detected under AC stress – PDIV 19 kVrms*

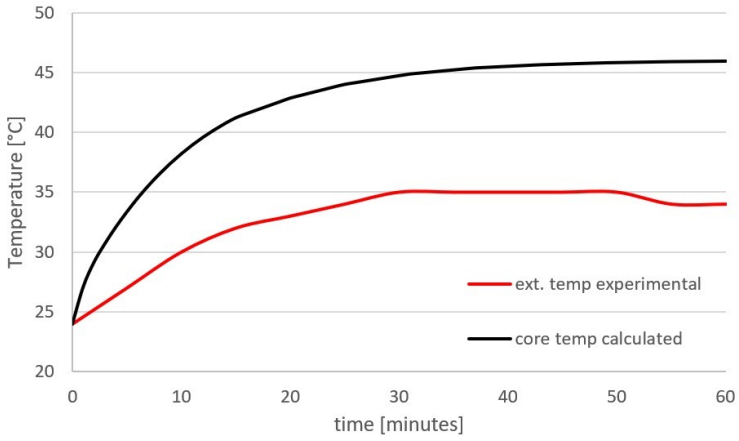


***Figure 4.14.*** *Time trend of the temperatures at the conductor and at the outer cable surface*

In Figure 4.15, a histogram shows the number of PD recorded during the experimental transient. The time has been divided into 5 minute bins. As can be seen, a large number of discharges were recorded immediately after the voltage has been applied and after the HVDC power supply has been turned off. On the other hand, an increasing number of PD over time has been detected after about half an hour from the beginning of the transient. The registered PD have been filtered by means of a comparison with the waveform detected during the test under AC voltage.

The typical PD waveform found during the test under DC stress and load is shown in Figure 4.16. This waveform is quite similar to those detected during the AC test with the main frequency components between 30 MHz and 35 MHz.

In Figure 4.17, the amplitude distribution of the signals relative to the measured PD is shown. Most of the discharges are associated with signals with amplitudes between 20 mV and 60 mV while 24 discharges are more energetic. The latter can be traced back to the phases of increasing and decreasing voltage.

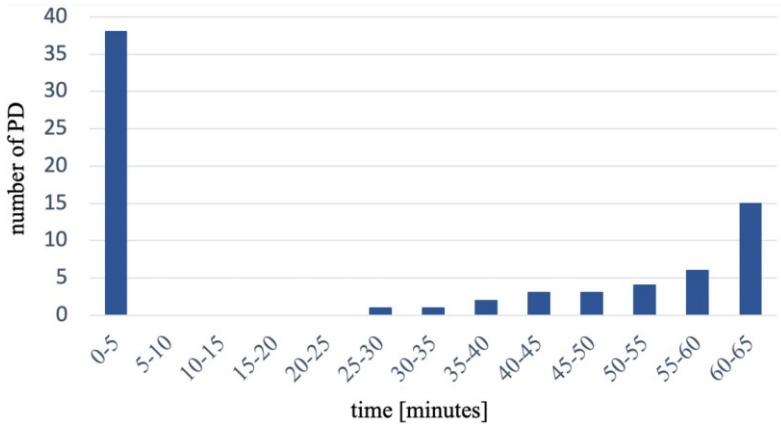


***Figure 4.15.*** *Time trend of the PD repetition rate*

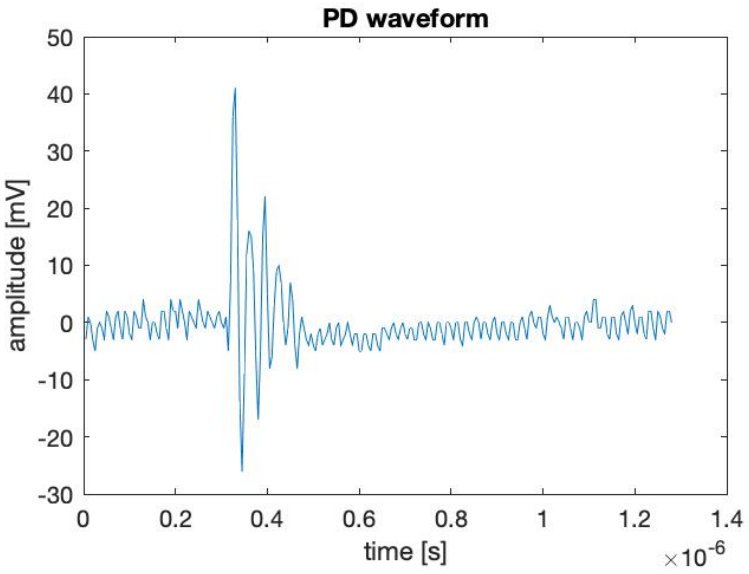


***Figure 4.16.*** *Typical waveform of the PD detected under DC stress – PDIV 60 kV @ temperature drop of 10 °C over the insulation thickness*

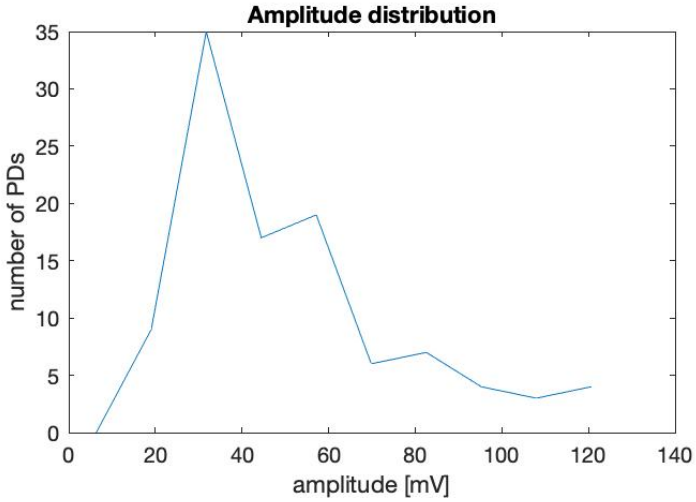


***Figure 4.17.*** *Amplitude distribution of PD detected under DC stress*

The same experiment was conducted in the absence of load current and other conditions being equal. In this case, no discharge was recorded during the time the voltage is kept stable. Only 41 PD were measured during the rising voltage ramp, within the first minute, and 7 PD following the switch off of the HVDC generator.

### 4.2.2 Calculation model and results

The conditions of the experiment were recreated in a coupled thermal and electrical 3D model of an angularly and axially delimited cable sector. For the purposes of these investigation, the occurrence of PD inside the cavity was excluded. In Figure 4.18, a 3D

view of the geometric model of the cable sector is shown whilst, in Figure 4.19, a cross section is depicted in order to describe the structure of the defected area. The geometrical domain of the cable sector is discretized by 84,012 elements. As shown in the Figure 4.19, the cavity has been modeled as an air-filled hemisphere whilst two air gaps are inserted to account for the partial removal and reapplication of the outer semiconductive layer as done in the actual cable. The radius of the hemispherical defect is 0.7 mm whilst the residual air gaps due to the cutting of the outer layer have a thickness of 0.3 mm. The screening tape and the stranded conductor are modeled as homogenous materials having equivalent properties to consider their filling factor. The modeled cable sector has a height of 20 mm and an angular amplitude of 50°.

The boundary conditions were set in accordance with the experiment performed, that is, a voltage of 60 kV and a thermal power generated in the conductor deriving from a load current of 260 A was applied.

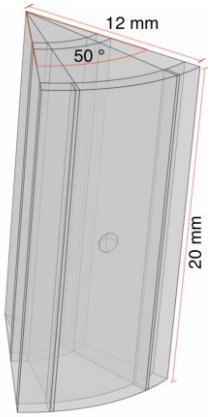


***Figure 4.18.*** *3D geometrical model of the defected mini-cable*

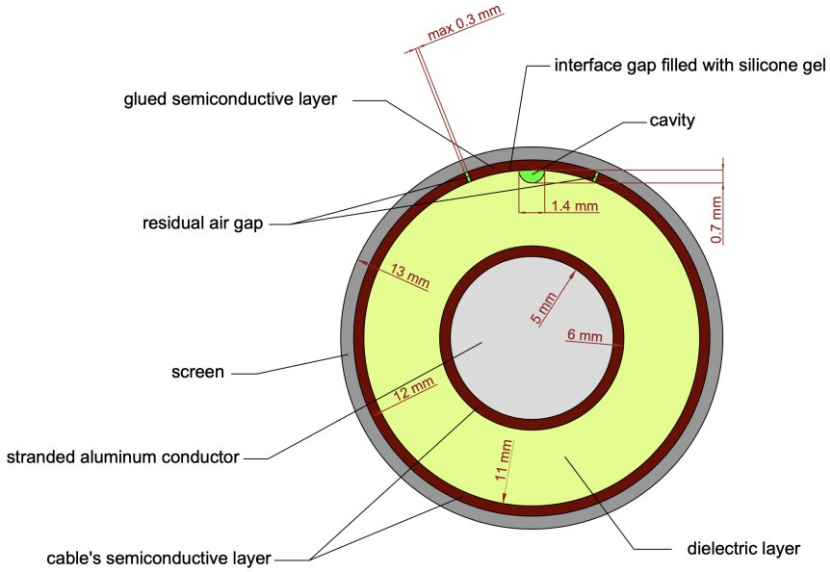


***Figure 4.19.*** *Description of the modeled geometry*

In Figure 4.20, the temperature distribution in the cable sector at the end of the 1 h transient is shown. As it can be observed, the temperature drop of 10.2 °C has been obtained from the simulation and the temperature at the outer cable surfaces resulted equal to 34.3 °C. This value is in good accordance with that obtained experimentally. As it can be observed in Figure 4.21, a maximum electric field of 16.2 kV/mm would be reached within the cavity if the occurrence of PD was excluded. On the other hand, as shown in Figure 4.22, the electric field would reach the maximum value of 20.0 kV/mm in absence of PD.

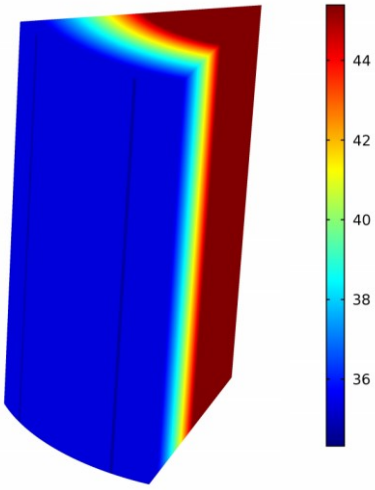


***Figure 4.20.*** *Temperature distribution in the cable sector at the end of the transient*

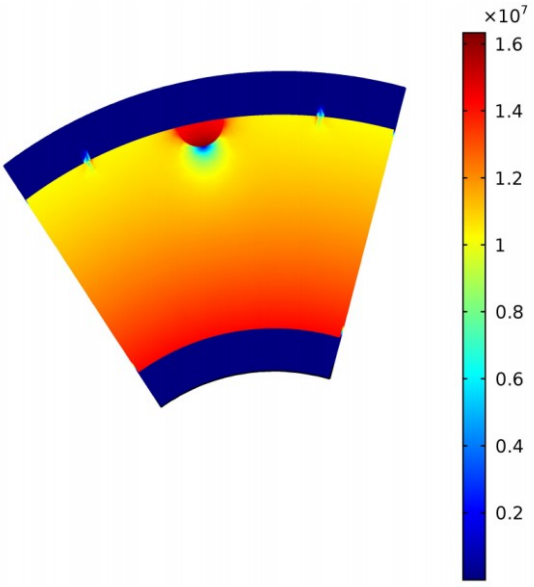


***Figure 4.21.*** *Electric field distribution without current load*

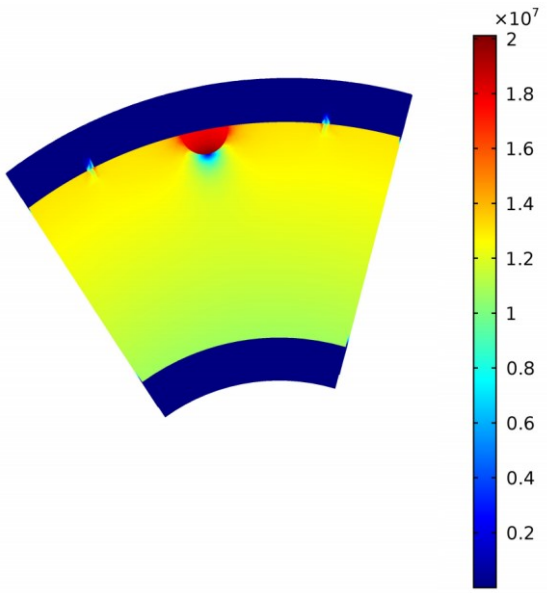


***Figure 4.22.*** *Electric field distribution with current load (end of the transient)*

### 4.2.3 Discussion

The total number of discharges detected under DC stress of 60 kV is much lower than that detected in the same time interval under AC voltage of 19 kVrms. This can be explained by the fact that the electric field intensification factor inside the cavity follows different rules depending on whether the external voltage applied is direct or alternating. During the DC test, the total lack of PD is observed during the first half hour, namely before reaching thermal equilibrium. This behavior demonstrates the existence of a correlation between the temperature distribution and the electric field in a cavity within a solid dielectric subjected to HVDC stress. In this scenario, according to what other researchers have found, the electric field profile results dependent on the distribution of electrical conductivity [93].

As shown in Figure 4.23, once the PD phenomenon has been triggered, the observed repetition rate is increasing over time with a pseudo-exponential trend. An equation obtained by fitting the obtained results is here shown:

$$PDRR = 4.173E - 15 * \exp(3.6078 * t) \quad (4.3)$$

Where *PDRR* is the PD repetition rate expressed in $s^{-1}$ and $t$ is the time expressed in s. The obtained time trend of the *PDRR* is however significant to show the triggering and

intensification of PD phenomena due exclusively to load transients, without variations in the applied voltage.

During the test in AC, PD with greater amplitude than in the case in DC have been detected. This can be explained by a greater weight, under AC stress, of the statistical time lag for the appearance of available electrons [94]. In fact, under AC voltage, the presence of an external dV/dt leads the electric field inside the cavity to exceed the trigger level with a greater time derivative.

The repetition rate levels found in this experiment are linked to a time constant linked to the product between permittivity and electrical conductivity of the materials. Therefore, a substantial increase in PD activity is expected with increasing temperature.

Under DC voltage and load, the PD repetition rate depends on the difference between the limit value of the voltage across the cavity if no PD would occur and the PD inception voltage [97-100]. As shown in Figure 4.24, this difference increases over time after the triggering of the first PD measured during the stable phase.

As shown in Figure 4.24, the electric field under DC and no load is lower than the detected inception value and therefore no PD are expected. Therefore, the experiments confirm this result.

Although the findings of this simulation are dependent on the conductivity parameters of the insulation material obtained from the literature, they still offer a reliable qualitative description of this phenomenon. In addition, the obtained PD inception electric field can be compared with that found by means of other techniques [101,102].

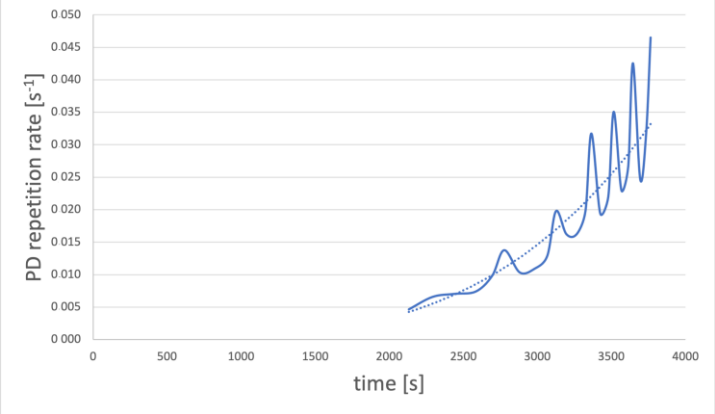


***Figure 4.23.*** *Time trend of the PD Repetition Rate (PDRR)*

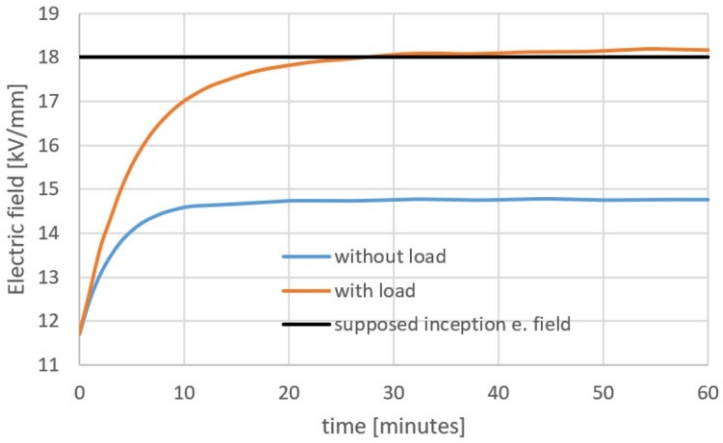


***Figure 4.24.*** *Comparison between the calculated average electric field inside the cavity and the supposed PD inception electric field*

## 4.3 Conclusions

In this Chapter, an analysis of the Partial Discharge (PD) phenomenon occurring in dielectrics under HVDC voltage stress is offered. This analysis is of particular interest for essentially two reasons.

Firstly, the phenomenon of PD in DC has been much less studied by researchers than in the AC case. Due to the small number of measurable PD under DC voltage and the lack of a time reference analogous to the sinusoid synchronized with the AC PD patterns, there are no widespread accepted techniques for recognizing and denoising in the event of DC stress.

The research presented in this chapter offers insights into experimental activities aimed at studying the interaction between PD and conductivity phenomena in dielectrics. The space charge accumulation significantly affect the conduction phenomena in insulating materials.

Secondly, the studies presented in this chapter aim to trying to use the initiation of PD and their repetition rate as an indirect measure of the electric field inside a cavity embedded in a dielectric material. In this way it is possible to compare experimental and simulation results in order to validate the calculation models and therefore obtain a tool useful to understand the space charge accumulation phenomena. This method could be combined with direct measurement methods such as the Pulsed Electro-Acoustic (PEA) method.

The results presented in this chapter show a good accordance between experimental results and those obtained through the use of models based on conductivity in dielectrics under DC voltage. However, the electric ignition fields for the PDs obtained from this

comparison are significantly higher than those obtainable from Paschen law. In all likelihood, this is due to the limit of conductivity models in appropriately considering the phenomena of entrapment and de-entrapment of the charge carriers and those of injection at the interfaces.

# Chapter 5
## Conclusions and future works

The objective of this work was to investigate the space charge phenomena occurring in dielectrics subjected to HVDC stress, study the state-of-the-art of methods and devices for measuring space charge and propose solutions aimed at improving these techniques and measurement tools. First, coupled thermal and electrical models were developed for the study of space charge accumulation phenomena in HVDC cables and accessories. These models are based on the Fourier equation for thermal conduction in solids, on Gauss's law for the electric field, on Ohm's law and on the continuity equation of current. The models used were built both using commercial FEM software and discretizing the aforementioned equations in Matlab®. The latter strategy aims at the automated execution of several simulations by varying the input parameters and minimizing the computational effort by optimizing the calculation code based on the specific case study. As part of this thesis, the results of studies on the effect, on electric field distribution, of axial heat transmission in HVDC cables and accessories were presented. From the analysis carried out, it can be seen that, in the event of discontinuity along the cable axis of the heat exchange conditions with the outside, local peaks of the electric field can be reached. This phenomenon should be considered in the design of cable lines to avoid reaching unexpected electric field peaks, especially as a result of transient phenomena such as Polarity Reversal and Transient Over-Voltages.

In the second chapter, the state of the art on methods for space charge measurement in flat specimens and HVDC cables is presented. In particular, the method called Pulsed Electro-Acoustic (PEA) was described, which is one of the two considered by the recommendations of international technical bodies such as IEEE and Cigrè. In the same chapter, the results of measurements carried out on mini-cable with a commercial PEA cell at the LEPRE high voltage laboratory of the University of Palermo are presented. The measurement campaign presented consists of carrying out space charge measurements on a mini-cable to which a voltage of 90 kV is applied and within which a load current of 264 A flows. The experimental results demonstrate a variation over time of the space charge

profile as an effect of the establishment of a temperature gradient over the insulation thickness.

In Chapter 3, the project of a novel PEA cell developed by the author is presented. This design has been developed starting from the experience of the LEPRE staff, the knowledge acquired by the author through the use of a commercial PEA cell and the need to deepen the knowledge of the space charge phenomenon. The designed PEA system has been optimized for flat specimens up to 5 mm thick capable of applying a temperature difference between the sample surfaces. The design of the PEA apparatus includes the choice and sizing of all the main components necessary for its construction. In Chapter 3, in addition to the calculations necessary for the project and for the choice of components, the detailed drawings are shown.

In Chapter 4, studies are presented aimed at investigating the relationship between space charge accumulation, conductivity and partial discharges phenomena in dielectrics. With this aim, two case studies have been investigated in which partial discharges are induced in artificial defects incorporated in dielectrics subjected to HVDC voltage.

In the first case, two cells, each consisting of two electrodes with a thermoplastic dielectric layer in between, are connected in series and subjected to HVDC voltage. One of the two cells contains an artificial defect between electrode and dielectric. Starting with this innovative setup, two experiments were conducted. The first experiment consists in measuring partial discharges by subjecting the couple of cells to different voltage levels whilst both are kept at room temperature. In this case, discharges are detected only immediately after the voltage rising ramp and once the highest value of the applied stable voltage reaches 20 kV. In the second experiment, the healthy cell is heated up to reach 80 °C whilst the sample containing the defect is held at room temperature. In this case, higher PD repetition rates are measured and the effect of the voltage division due to the increased temperature of the healthy cell is evident. The experimental results were compared with those obtained by a circuital model based on the conductivity in dielectrics. The comparison showed a good accordance between the model and the experimental findings.

In the second case study described in the Chapter 4, an artificial defect was made between the dielectric and the outer surface of a model cable subjected to HVDC voltage and load current. The experiment aimed to demonstrate the inception of PD when the establishment of a temperature gradient leads to exceed the inception electric field within

the cavity, whilst the applied voltage is kept constant. The experiment lasted 1 h and showed the onset of PD after approximately 30 minutes from the beginning of the test. Furthermore, once the PD inception threshold was exceeded, the repetition rate seemed to increase with an exponential law. The experiment performed on the mini-cable was reproduced through simulations carried out with the use of a commercial FEM software where a coupled thermal and electrical model is implemented. The simulation results appear qualitatively coherent with the experimental ones. However, an optimization of the model including coefficients for considering the trapping and de-trapping of charge carriers appears necessary to improve its reliability.

From the research activity described in this thesis, two main lines of future developments arise. First of all, the designed PEA system and its optimization will be carried out it in order to obtain interesting information about the distribution of space charge and electric field in dielectrics subjected to HVDC voltage and thermal gradient. Secondly, the simultaneous development of experimental setups and models for the calculation of the electric field in dielectrics subjected to HVDC stress will be carried out in order to better understand the phenomena leading to premature aging of the insulation in cables and accessories.

# Acknowledgement

Many people I would like to thank for having been helpful or in any case close to me since the beginning of this journey that began in a particular period of my life. Firstly, I would like to thank prof. Romano for welcoming me and for transferring me so much of his experience and scientific knowledge. I thank Antonino Imburgia of the LEPRE Laboratory for the immense amount of advice he has given me during these three years. I thank prof. Ala for his role as a scientific reference point. I would also like to thank Professors Yuriy Serdyuk and Thomas Hammarström of Chalmers University of Technology for their support and collaboration in investigations on partial discharges under DC voltage. I also thank the staff of Prysmian Group for giving me the opportunity for a professional growth, in particular Roberto Candela, Fabrizio Buccheri, Vincenzo Li Vigni, Marco Albertini and Stefano Franchi Bononi. I also thank the coordinator of the PhD prof. Maurizio Cellura for his constant willingness.

I especially thank my wife Erika for being close to me even in the most difficult moments, for her love and for taking care of me. I thank Erika's parents for helping us at the start of this challenge and on so many other occasions when we needed them. Thanks Elio and Anna. I would also like to thank my brother-in-law Giuseppe and my sister-in-law Marta for giving me a piece of their happiness. Last but not the least, I would like to acknowledge with gratitude my family for their support in every moment of my life. Thanks to my father Fernando, my mother Maria, my brother and my sister-in-law Mariangela, my sister and my brother-in-law Alessio. Thanks also to my grandparents Tanino, Rosetta, Peppino and Antonietta for the important human values that they passed on to me. And finally, thanks to my very nice nephews Angelica and Fernando for being able to make me smile at any time.

# References


[1] M. Mammeri and B. Dhuicq, "Challenges of extruded cable for HVAC and HVDC power transmission," 2013 IEEE Grenoble Conference, 2013, pp. 1-8.

[2] G. Mazzanti, M. Marzinotto, "Improved Design of HVDC Extruded Cable Systems," in Extruded Cables for High-Voltage Direct-Current Transmission: Advances in Research and Development, 1, Wiley-IEEE Press, 2013.

[3] U. Axelsson, A. Holm, C. Liljegren, M. Aberg, K. Eriksson and O. Tollerz, "The Gotland HVDC Light project-experiences from trial and commercial operation," 16th International Conference and Exhibition on Electricity Distribution, 2001. Part 1: Contributions. CIRED. (IEE Conf. Publ No. 482), 2001, pp. 5 pp. vol.1.

[4] G. C. Montanari, "The Potential Impact of Flexible DC Transmission and Distribution on Insulated Cables: Accelerated Aging and Premature Failure," 2019 IEEE PES Asia-Pacific Power and Energy Engineering Conference (APPEEC), 2019, pp. 1-4.

[5] F. -B. Meng et al., "Effect of Thermal Ageing on Physico-Chemical and Electrical Properties of EHVDC XLPE Cable Insulation," in IEEE Transactions on Dielectrics and Electrical Insulation, vol. 28, no. 3, pp. 1012-1019, June 2021.

[6] A. K. Upadhyay and C. C. Reddy, "Comparative study of famous conductivity models for low density polyethylene," 2017 IEEE International Conference on Industrial and Information Systems (ICIIS), 2017, pp. 1-4.

[7] N. Haque, S. Dalai, B. Chatterjee and S. Chakravorti, "Investigation of charge trapping behavior of LDPE using de-trapping characteristics," 2016 IEEE 7th Power India International Conference (PIICON), 2016, pp. 1-5.

[8] G. Li, S. Li, D. Min, N. Zhao and Y. Zhu, "Influence of trap depths on space charge formation and accumulation characteristics in low density polyethylene," 2013 IEEE International Conference on Solid Dielectrics (ICSD), 2013, pp. 698-701.

[9] G. Rizzo, P. Romano, A. Imburgia, F. Viola, and G. Ala, “The Effect of the Axial Heat Transfer on Space Charge Accumulation Phenomena in HVDC Cables,” Energies, vol. 13, no. 18, p. 4827, Sep. 2020.

[10] G. Rizzo et al., "Space charge accumulation in undersea HVDC cables as function of heat exchange conditions at the boundaries – water-air interface," 2020 IEEE 20th Mediterranean Electrotechnical Conference (MELECON), 2020, pp. 447-452.

[11] P. Romano et al., "Investigation on partial discharges in HVDC cables after polarity reversal events," 2020 IEEE Conference on Electrical Insulation and Dielectric Phenomena (CEIDP), 2020, pp. 292-295.

[12] G. Rizzo et al., "Polarity reversal in HVDC joints - the effect of the axial thermal conduction," 2020 IEEE Conference on Electrical Insulation and Dielectric Phenomena (CEIDP), 2020, pp. 115-118.

[13] G. Rizzo et al., "The effect of Transient Over Voltages on the Partial Discharges activity in HVDC joints," 2021 AEIT HVDC International Conference (AEIT HVDC), 2021, pp. 1-6.

[14] G. Rizzo et al., "Effect of Heat Exchange Transient Conditions With Moving Water-Air Interface on Space Charge Accumulation in Undersea HVdc Cables," in IEEE Transactions on Industry Applications, vol. 57, no. 5, pp. 4528-4536, Sept.-Oct. 2021.

[15] P. Morshuis, A. Cavallini, D. Fabiani, G. C. Montanari and C. Azcarraga, "Stress conditions in HVDC equipment and routes to in service failure," in IEEE Transactions on Dielectrics and Electrical Insulation, vol. 22, no. 1, pp. 81-91, Feb. 2015.

[16] E. Doedens, E. M. Jarvid, R. Guffond, and Y. V. Serdyuk, “Space Charge Accumulation at Material Interfaces in HVDC Cable Insulation Part I—Experimental Study and Charge Injection Hypothesis,” Energies, vol. 13, no. 8, p. 2005, Apr. 2020.

[17] J. Y. Steven, T. T. N. Vu, G. Teyssedre and N. I. Sinisuka, "Conductivity measurements and space charge inference in polymeric-insulated HVDC model cables," 2014 ICHVE International Conference on High Voltage Engineering and Application, 2014, pp. 1-4.

[18] Nugroho Adi et al, “DC Model Cable under Polarity Inversion and Thermal Gradient: Build-Up of Design-Related Space Charge”; Technologies 2017, 5, 46.

[19] G. Chen, M. Hao, Z. Xu, A. Vaughan, J. Cao and H. Wang, "Review of high voltage direct current cables," in CSEE Journal of Power and Energy Systems, vol. 1, no. 2, pp. 9-21, June 2015.

[20] Z. An, J. Cang, X. Chen and Y. Liu, "Low field thermally assisted charge injection at electrode/polyethylene interfaces observed by space charge measurements," 2013 IEEE International Conference on Solid Dielectrics (ICSD), 2013, pp. 480-483.

[21] D. van der Born, I. A. Tsekmes, P. H. F. Morshuis, J. J. Smit, T. J. Person and S. J. Sutton, "Evaluation of apparent trap-controlled mobility and trap depth in polymeric HVDC mini-cables," 2013 IEEE International Conference on Solid Dielectrics (ICSD), 2013, pp. 242-245.

[22] M. Marzinotto, A. Battaglia and G. Mazzanti, "Space charges and life models for lifetime inference of HVDC cables under voltage polarity reversal," 2019 AEIT HVDC International Conference (AEIT HVDC), 2019, pp. 1-5.

[23] M. A. Fard, A. J. Reid, D. M. Hepburn and M. E. Farrag, "Partial discharge behavior under HVDC superimposed with transients," 2016 51st International Universities Power Engineering Conference (UPEC), 2016, pp. 1-5.

[24] "IEEE Recommended Practice for Space Charge Measurements on High-Voltage Direct-Current Extruded Cables for Rated Voltages up to 550 kV," in IEEE Std 1732-2017 , vol., no., pp.1-36, 26 June 2017.

[25] IEC standard 60287-2-1 (2015), “Electric Cables – Calculation of the current rating – Part 2: Thermal resistance – Section 1: Calculation of thermal resistance”.

[26] H. Choi and Y. H. Zhang, "Monthly variation of sea-air temperature differences in the korean coast", J. Oceanogr., vol. 61, pp. 359-367, 2005.

[27] E. Doedens, E. M. Jarvid, R. Guffond, and Y. V. Serdyuk, “Space Charge Accumulation at Material Interfaces in HVDC Cable Insulation Part II—Simulations of Charge Transport,” Energies, vol. 13, no. 7, p. 1750, Apr. 2020.

[28] Y. Hao, J. Han, G. Guo, H. Li and J. Deng, "Influence of Conductivity on Tangential Electric Field of Composite Interface of HVDC Cable Joint," 2020 4th International Conference on HVDC (HVDC), 2020, pp. 1121-1124.

[29] Y. Qin, N. Shang, M. Chi and X. Wang, "Impacts of temperature on the distribution of electric-field in HVDC cable joint," 2015 IEEE 11th International Conference on the Properties and Applications of Dielectric Materials (ICPADM), 2015, pp. 224-227.

[30] Y. -G. An, C. -H. Kim, T. -W. Nam and J. -H. Lee, "A Study on the Behavior of Interfacial Space Charge at Polymer Dielectric Double-Layer Simulating the HVDC Cable Joints," 2020 International Symposium on Electrical Insulating Materials (ISEIM), 2020, pp. 158-161.

[31] "IEEE Recommended Practice for Partial Discharge Measurements under AC Voltage with VHF/UHF Sensors during Routine Tests on Factory and Pre-Molded Joints of HVDC Extruded Cable Systems up to 800 kV," in IEEE Std 2862-2020 , vol., no., pp.1-31, 8 March 2021.

[32] G. Rizzo, P. Romano, A. Imburgia, and G. Ala, “Review of the PEA Method for Space Charge Measurements on HVDC Cables and Mini-Cables,” Energies, vol. 12, no. 18, p. 3512, Sep. 2019.

[33] A. Imburgia, P. Romano, G. Chen, G. Rizzo, E. Riva Sanseverino, F. Viola, and G. Ala, “The Industrial Applicability of PEA Space Charge Measurements, for Performance Optimization of HVDC Power Cables,” Energies, vol. 12, no. 21, p. 4186, Nov. 2019.

[34] A. Imburgia, P. Romano, G. Rizzo, F. Viola, G. Ala, and G. Chen, “Reliability of PEA Measurement in Presence of an Air Void Defect,” Energies, vol. 13, no. 21, p. 5652, Oct. 2020.

[35] A. Toureille and J. P. Reboul, “The thermal-step-technique applied to the study of charge decay in polyethylene thermoelectrets,” in Proceedings of 6th International Symposium on Electrets (ISE 6) (IEEE, 1988), pp. 23–27.

[36] A. Toureille, P. Notingher, N. Vella, S. Malrieu, J. Castellon, and S. Agnel, “The thermal step technique: An advanced method for studying the properties and testing the quality of polymers,” Polym. Int. 46(2), 81–92 (1998).

[37] P. Notingher, S. Agnel, and A. Toureille, “Recent advances in calculating space charge distribution by processing the signals obtained using the thermal step method,” in Annual Report, Conference on Electrical Insulation and Dielectric Phenomena (IEEE, 1998), Vol. 1, pp.154–157.

[38] G. M. Sessler, “Charge distribution and transport in polymers,” IEEE Trans. Dielectr. Electr. Insul. 4(5), 614–628 (1997).

[39] C. Stancu et al., “Electric field computation in water treed polyethylene with space charge accumulation,” in Conference Record of the 2006 IEEE International Symposium on Electrical Insulation (IEEE, Toronto, Ontario, 2006), pp. 186–189.

[40] P. Notingher, S. Agnel, and A. Toureille, “Thermal step method for space charge measurements under applied dc field,” IEEE Trans. Dielectr. Electr. Insul. 8(6), pp. 985–994, 2001.

[41] S. Agnel, P. Notingher, and A. Toureille, “Space charge measurements under applied DC field by the thermal step method,” in Annual Report Conference on Electrical Insulation and Dielectric Phenomena (IEEE, 2000), Vol. 1, pp. 166–170.

[42] A. Cherifi, M. A. Dakka, and A. Toureille, “The validation of the thermal step method,” IEEE Trans. Electr. Insul. 27(6), 1152–1158 (1992).

[43] J. Laurentie, H. Yahyaoui, P. Notingher, J. Castellon, and S. Agnel, “Contactless electric field and space charge measurement across solid dielectrics: A fully non-intrusive thermal technique,” in IEEE Industry Applications Society Annual Meeting (IEEE, 2014), pp. 1–4.

[44] A. Hascoat et al., “Study and analysis of conduction mechanisms and space charge accumulation phenomena under high applied DC electric field in XLPE for HVDC cable application,” in 2014 IEEE Conference on Electrical Insulation and Dielectric Phenomena (CEIDP) (IEEE, Des Moines, IA, 2014), pp. 530–533.

[45] J. Castellon, P. Notingher, S. Agnel, A. Toureille, J. Matallana, H. Janah, P. Mirebeau, and D. Sy, “Industrial installation for voltage-on space measurements in HVDC cables,” in Industry Applications Conference, Fourtieth IAS Annual Meeting, Conference Record of the 2005 (IEEE, 2005), Vol. 2, pp. 1112–1118.

[46] P. Notingher, A. Toureille, S. Agnel, and J. Castellon, “Determination of electric field and space charge in the insulation of power cables with the thermal step method and a newmathematical processing,” IEEE Trans. Ind. Appl. 45(1), 67–74 (2009).

[47] G. Platbrood, S. Agnel, A. Toureille, and P. Bulens, “Comparison of new cables and aged cables out of the grid by the Thermal Step Method,” in Annual Report Conference on Electrical Insulation and Dielectric Phenomena (IEEE, 2002), pp. 396–399.

[48] J. Castellon et al., “A new diagnosis of the XLPE insulation with water treeing by space charge measurements with the thermal step method and water nuclear magnetic resonance imaging,” in 2005 Annual Report Conference on Electrical Insulation and Dielectric Phenomena, CEIDP’05 (IEEE, 2005), pp. 536–539.

[49] A. Darkawi, P. Notingher, T. Martire, J. Huselstein, and F. Forest, “Portable installation for space charge measurements on full-size high voltage cable loops based on a multicell power converter,” in Annual Report Conference on Electrical Insulation and Dielectric Phenomena (CEIDP) (IEEE, 2012), pp. 499–502.

[50] G. Mazzanti, G. Chen, J. C. Fothergill, N. Hozumi, J. Li, M. Marzinotto, F. Mauseth, P. Morshuis, C. Reed, A. Tzimas, and W. Kai, “A protocol for space charge measurements in full-size HVDC extruded cables,” IEEE Trans. Dielectr. Electr. Insul. 22(1), 21–34 (2015).

[51] H. Hussaini, A. A. Ahmad and A. A. Susan, "Review of space-charge measurement using Pulsed Electro-Acoustic Method: Advantages and Limitations", J. Eng. Research Applications, vol. 5, pp. 90-95, 2015.

[52] T. Takada, M. Takatsuka, T. Futami and M. Sugimori, "Measurement of spatial distributions of mobility and conductivity in electron-beam-irradiated PMMA," Annual Conference on Electrical Insulation and Dielectric Phenomena, 1990, pp. 126-131.

[53] G. Mazzanti et al., "A protocol for space charge measurements in full-size HVDC extruded cables," in IEEE Transactions on Dielectrics and Electrical Insulation, vol. 22, no. 1, pp. 21-34, Feb. 2015.

[54] IEC/TS 62758, Calibration of Space Charge Measuring Equipment Based on the Pulsed Electroacoustic (PEA) Measurement Principle, 2012.

[55] X. Wang et al., "Comparison and analysis of three pulse injection methods in the pulsed electroacoustic technique used for long cables," in IEEE Electrical Insulation Magazine, vol. 34, no. 4, pp. 17-31, July-August 2018.

[56] R. Bodega, P. H. F. Morshuis and J. J. Smit, "Space charge signal interpretation in a multi-layer dielectric tested by means of the PEA method," Proceedings of the 2004 IEEE International Conference on Solid Dielectrics, 2004. ICSD 2004., 2004, pp. 240-243 Vol.1.

[57] R. Bodega, P. H. F. Morshuis and J. J. Smit, "Space charge measurements on multi-dielectrics by means of the pulsed electroacoustic method," in IEEE Transactions on Dielectrics and Electrical Insulation, vol. 13, no. 2, pp. 272-281, April 2006.

[58] M. De Araujo Andrade et al., "Interpretation of PEA Output Signal in a Multilayer Specimen," 2018 IEEE Conference on Electrical Insulation and Dielectric Phenomena (CEIDP), 2018, pp. 101-104.

[59] K. Fukunaga, H. Miyata, M. Sugimori, T. Takada, “Measurement of Charge Distribution in the Insulation of Cables using Pulsed Electroacoustic Method” Ieej Trans. Fundam. Mater. 1990, 110, 647–648.

[60] N. Hozumi, T. Okamoto and T. Imajo, "Space charge distribution measurement in a long size XLPE cable using the pulsed electroacoustic method," Conference Record of the 1992 IEEE International Symposium on Electrical Insulation, 1992, pp. 294-297.

[61] M. Yasuda, M. Ito, T. Takada, “Measurement of charge distribution in coaxial cable using the Pulsed Electroacoustic Method”, Jpn. J. Appl. Phys. 1991, 30, 71.

[62] R.Liu, T. Takada, N. Takasu, “Pulsed electro-acoustic method for measurement of space charge distribution in power cables under both DC and AC electric field”, Jpn. J. Appl. Phys. 1993, 26, 986.

[63] M. Fu, G. Chen, A.E. Davies, Y. Tanaka, T. Takada, “A Modified PEA Space Charge Measuring System for Power Cables”, In Proceedings of the 6th International Conference on Properties and Applications of Dielectric Materials, Xi’an, China, 21–26 June 2000.

[64] H. , Zheng, “Application of PEA Technique to Space Charge Measurement in Cylindrical Geometry HV Cable Systems”, Ph.D. Thesis, Department of Engineering, University of Leicester, Leicester, UK, 2015.

[65] I. M. Zimmerling, I. A. Tsekmes, P. H. F. Morshuis, J. J. Smit, T. J. Person and T. Geussens, "Space charge analysis of modified and unmodified XLPE model-cables under different electric fields and temperatures," 2015 IEEE Conference on Electrical Insulation and Dielectric Phenomena (CEIDP), 2015, pp. 134-137.

[66] N. Adi, G. Teyssedre, T. T. N. Vu and N. I. Sinisuka, "DC field distribution in XLPE-insulated DC model cable with polarity inversion and thermal gradient," 2016 IEEE International Conference on High Voltage Engineering and Application (ICHVE), 2016, pp. 1-4.

[67] C. Iyyappan and C. C. Reddy, "Inverse Power Law based Inclusive Life Model for DC Polarity Reversal Stresses," in IEEE Transactions on Dielectrics and Electrical Insulation, vol. 28, no. 2, pp. 586-593, April 2021.

[68] K. Wu, Y. Wang, X. Wang, M. Fu and S. Hou, "Effect of space charge in the aging law of cross-linked polyethylene materials for high voltage DC cables," in IEEE Electrical Insulation Magazine, vol. 33, no. 4, pp. 53-59, July-August 2017.

[69] G. Mazzanti and M. Marzinotto, "Combination of probabilistic electro-thermal life model and discrete enlargement law for power cable accessories," 2016 IEEE International Conference on Dielectrics (ICD), 2016, pp. 780-783.

[70] T. Liu et al., "A new method of estimating the inverse power law ageing parameter of XLPE based on step-stress tests," 2013 Annual Report Conference on Electrical Insulation and Dielectric Phenomena, 2013, pp. 69-72.

[71] A. Imburgia, P. Romano, E. R. Sanseverino, L. D. Rai, S. F. Bononi and I. troia, "Pulsed Electro-Acoustic Method for specimens and cables employed in HVDC systems: some feasibility considerations," 2018 AEIT International Annual Conference, 2018, pp. 1-6.

[72] R. Bodega, P. H. F. Morshuis and J. J. Smit, "Electrostatic force distribution in a multi-layer dielectric tested by means of the PEA method," Proceedings of the 2004 IEEE International Conference on Solid Dielectrics, 2004. ICSD 2004., 2004, pp. 264-267 Vol.1.

[73] M. Hao, A. Fazal, A. S. Vaughan, G. Chen, J. Cao and H. Wang, "The effect of electrode material and semicon bonding on space charge dynamics of XLPE," 2016 IEEE International Conference on Dielectrics (ICD), 2016, pp. 200-203.

[74] Zhiyu Yan, Baozhong Han, H. Zhao, J. Yang and Chunyang Li, "Space charge and conductivity characteristics of CB/XLPE nanocomposites," Proceedings of 2014 International Symposium on Electrical Insulating Materials, 2014, pp. 30-33.

[75] H. Suzuki, A. Nozomu, H. Miyake, Y. Tanaka and T. Maeno, "Space charge accumulation and electric breakdown in XLPE under DC high electric field," 2013 Annual Report Conference on Electrical Insulation and Dielectric Phenomena, 2013, pp. 250-253.

[76] T. Takada, Y. Satoh and Y. Tanaka, "Comparison between PWP method using piezo-electric transducer and PEA method," 9th International Symposium on Electrets (ISE 9) Proceedings, 1996, pp. 355-360.

[77] K. Sonoda et al., "Development of semiconductor sensor as a use for pulsed electro-acoustic method," 2017 International Symposium on Electrical Insulating Materials (ISEIM), 2017, pp. 601-604.

[78] Z. Gibson, J. R. Dennison, L. Pearson, E. Griffiths, A. Pearson and V. Griseri, "Effects of Sample Adhesives Acoustic Properties on Spatial Resolution of Pulsed Electroacoustic Measurements," *2018 IEEE Conference on Electrical Insulation and Dielectric Phenomena (CEIDP)*, 2018, pp. 267-270.

[79] P. E. Bloomfield, Wei-Jung Lo and P. A. Lewin, "Experimental study of the acoustical properties of polymers utilized to construct PVDF ultrasonic transducers and the acousto-electric properties of PVDF and P(VDF/TrFE) films," in IEEE Transactions on Ultrasonics, Ferroelectrics, and Frequency Control, vol. 47, no. 6, pp. 1397-1405, Nov. 2000.

[80] M.D.Raisinghania, 'Fluid Dynamics With Complete Hydrodynamics and Boundary Layer Theory', New Delhi : S. Chand & Company, 2013.

[81] D. D. Kurniawan, A. Cavallini, Suwarno, L. Cirioni and R. Candela, "A Novel Setup To Investigate Partial Discharges In Interfaces Subjected To HVDC Voltages," 2019 2nd International Conference on High Voltage Engineering and Power Systems (ICHVEPS), 2019.

[82] X. Chen, A. Cavallini and G. C. Montanari, "Dependence of partial discharges in HVDC on environment: Implications for condition assessment monitoring," 2009 IEEE 9th International Conference on the Properties and Applications of Dielectric Materials, 2009, pp. 429-432.

[83] S. Blufpand, A. R. Mor, P. Morshuis and G. C. Montanari, "Partial discharge recognition of insulation defects in HVDC GIS and a calibration approach," 2015 IEEE Electrical Insulation Conference (EIC), 2015, pp. 564-567.

[84] D. Wienold, U. Lühring and F. Jenau, "Detection and distinction of partial discharges in air at DC voltage by using a non-conventional approach in the high-frequency range," 2017 IEEE International Conference on Environment and Electrical Engineering and 2017 IEEE Industrial and Commercial Power Systems Europe (EEEIC / I&CPS Europe), 2017, pp. 1-5.

[85] S. Kumara, Y. V. Serdyuk and M. Jeroense, "Calculation of Electric Fields in HVDC Cables: Comparison of Different Models," in IEEE Transactions on Dielectrics and Electrical Insulation, vol. 28, no. 3, pp. 1070-1078, June 2021.

[86] Jiandong Wu, Li Lan, Zhe Li and Yi Yin, "Simulation of space charge behavior in LDPE with a modified of bipolar charge transport model," Proceedings of 2014 International Symposium on Electrical Insulating Materials, 2014, pp. 65-68.

[87] H. C. Liang et al., "Improved Interface Charge Transport Model of HVDC Cable Joint-Considering Carrier Dynamic Equilibrium," 2020 International Symposium on Electrical Insulating Materials (ISEIM), 2020, pp. 151-154.

[88] Z. Lv, S. M. Rowland and K. Wu, "Simulation of fast space charge packets transport in polymers," 2017 IEEE Conference on Electrical Insulation and Dielectric Phenomenon (CEIDP), 2017, pp. 98-101.

[89] Y. Wang, X. Yang, A. Ma and Y. Yin, "Simulation of Space Charge Distribution in the Insulation Layer of XLPE HVDC Cable under Different Temperatures," 2020 International Symposium on Electrical Insulating Materials (ISEIM), 2020, pp. 143-146.

[90] X. Gu, S. He, Y. Xu, Y. Yan, S. Hou and M. Fu, "Partial discharge detection on 320 kV VSC-HVDC XLPE cable with artificial defects under DC voltage," in IEEE Transactions on Dielectrics and Electrical Insulation, vol. 25, no. 3, pp. 939-946, June 2018.

[91] Y. Trotsenko, V. Brzhezitsky and O. Protsenko, "Partial Discharge as Threat to Insulation of High Voltage Direct Current Transmissions," IEEE 6th International Conference on Energy Smart Systems (ESS), 2019, pp. 24-27.

[92] E. A. Morris, W. H. Siew and M. J. Given, "Methods of Characterisation of DC Partial Discharge in Polymeric Cable Insulation," 2018 IEEE Conference on Electrical Insulation and Dielectric Phenomena (CEIDP), 2018, pp. 494-497.

[93] A. Setyowibowo, Suwarno, A. Cavallini and G. C. Montanari, "Partial discharge measurements in XLPE cables with misplaced grading system under different applied voltage frequencies," 2017 International Conference on High Voltage Engineering and Power Systems (ICHVEPS), 2017, pp. 460-465.

[94] H. A. Illias, M. A. Tunio, H. Mokhlis, G. Chen, and A. H. A. Bakar, “Determination of partial discharge time lag in void using physical model approach,” IEEE Trans. Dielectr. Electr. Insul., vol. 22, no. 1, pp. 463–471, Feb. 2015.

[95] S. Zhang and Y. Liu, "Simulation of space charge accumulation in LDPE under temperature gradient with temperature-dependent parameters," 2018 12th International Conference on the Properties and Applications of Dielectric Materials (ICPADM), 2018, pp. 1028-1032.

[96] C. Jörgens and M. Clemens, "Simulation of the electric field in high voltage direct current cables and the influence on the environment," Tenth International Conference on Computational Electromagnetics (CEM 2019), 2019, pp. 1-5.

[97] P. H. F. Morshuis and J. J. Smit, "Partial discharges at DC voltage: their mechanism, detection and analysis," IEEE Transactions on Dielectrics and Electrical Insulation, vol. 12, no. 2, pp. 328-340, April 2005.

[98] T. Takahashi et al, "AC and DC partial discharge measurements on defective cables," IEEE Electrical Insulation Conference (EIC), 2016, pp. 375-378.

[99] H. Saadati et al, "Fundamental Difference of Partial Discharge Phenomena under AC and DC Stresses," IEEE International Conference on High Voltage Engineering and Application (ICHVE), 2018, pp. 1-4.

[100] E. A. Morris and W. H. Siew, "A comparison of AC and DC partial discharge activity in polymeric cable insulation," IEEE 21st International Conference on Pulsed Power (PPC), 2017, pp. 1-4.

[101] P. Romano et al, "A new technique for partial discharges measurement under DC periodic stress," IEEE Conference on Electrical Insulation and Dielectric Phenomenon (CEIDP), 2017, pp. 303-306.

[102] P. Romano et al, "A New Approach to Partial Discharge Detection Under DC Voltage: Application to Different Materials," IEEE Electrical Insulation Magazine, vol. 37, no. 2, pp. 18-32, March-April 2021.

La borsa di dottorato è stata cofinanziata con risorse del
Programma Operativo Nazionale Ricerca e Innovazione 2014-2020 (CCI 2014IT16M2OP005),
Fondo Sociale Europeo, Azione I.1 “Dottorati Innovativi con caratterizzazione Industriale”

UNIONE EUROPEA
Fondo Sociale Europeo